

# Large Interstellar Polarisation Survey

## LIPS I: FORS2 spectropolarimetry in the Southern Hemisphere<sup>★</sup>

Stefano Bagnulo<sup>1</sup>, Nick L.J. Cox<sup>2</sup>, Aleksandar Cikota<sup>3</sup>, Ralf Siebenmorgen<sup>3</sup>, Nikolai V. Voshchinnikov<sup>4</sup>, Ferdinando Patat<sup>3</sup>, Keith T. Smith<sup>5</sup>, Jonathan V. Smoker<sup>6</sup>, Stefan Taubenberger<sup>3,7</sup>, Lex Kaper<sup>2</sup>, Jan Cami<sup>8</sup>, and the LIPS collaboration

<sup>1</sup> Armagh Observatory and Planetarium, College Hill, Armagh BT61 9DG, Northern Ireland, U.K. e-mail: sba@arm.ac.uk

<sup>2</sup> Anton Pannekoek Institute for Astronomy, University of Amsterdam, NL-1090 GE Amsterdam, The Netherlands

<sup>3</sup> European Southern Observatory, Karl-Schwarzschild-Str. 2, D-85748 Garching b. München, Germany

<sup>4</sup> Sobolev Astronomical Institute, St. Petersburg University, Universitetskii prosp. 28, St. Petersburg, 198504 Russia

<sup>5</sup> AAAS Science International, Clarendon House, Clarendon Road, Cambridge CB2 8FH, UK

<sup>6</sup> European Southern Observatory, Alonso de Cordova 3107, Casilla 19001, Vitacura, Santiago 19, Chile

<sup>7</sup> Max-Planck-Institut für Astrophysik, Karl-Schwarzschild-Str. 1, D-85741 Garching b. München, Germany

<sup>8</sup> Department of Physics and Astronomy and Centre for Planetary Science and Exploration (CPSX), The University of Western Ontario, London, ON N6A 3K7, Canada

Received: 2017-06-28 / Accepted: 2017-10-02

### ABSTRACT

Polarimetric studies of light transmitted through interstellar clouds may give constraints on the properties of the interstellar dust grains. Traditionally, broadband linear polarisation (BBLP) measurements have been considered an important diagnostic tool for the study of the interstellar dust, while comparatively less attention has been paid to spectropolarimetric measurements. However, spectropolarimetry may offer stronger constraints than BBLP, for example by revealing narrowband features, and by allowing us to distinguish the contribution of dust from the contribution of interstellar gas. Therefore, we have decided to carry out a Large Interstellar Polarisation Survey (LIPS) using spectropolarimetric facilities in both hemispheres. Here we present the results obtained in the Southern Hemisphere with the FORS2 instrument of the ESO Very Large Telescope. Our spectra cover the wavelength range 380–950 nm at a spectral resolving power of about 880. We have produced a publicly available catalogue of 127 linear polarisation spectra of 101 targets. We also provide the Serkowski-curve parameters, as well as the wavelength gradient of the polarisation position angle for the interstellar polarisation along 76 different lines of sight. In agreement with previous literature, we found that the best-fit parameters of the Serkowski-curve are not independent of each other. However, the relationships that we obtained are not always consistent with what has been found in previous studies.

**Key words.** Polarisation – ISM: dust, extinction

## 1. Introduction

A full characterisation of the interstellar medium (ISM) is of crucial importance to understand the chemical history of the Universe and various fundamental astrophysical processes, such as the formation and evolution of the stars and their planetary systems. Most of the heavy elements are present in the ISM in the form of dust grains. Non-spherical dust grains, aligned along a preferred direction, linearly polarise the stellar background radiation at wavelengths close to the grain size. Therefore, linear polarimetric measurements of stars that are not intrinsically polarised may set constraints on the chemical composition, shape, and size distribution of the interstellar dust, as well as on the mechanisms responsible for dust grain alignment.

Polarimetry of the interstellar medium started with the discovery work by Hiltner (1949), Hall (1949), and Dombrowskii (1949), culminating later into major surveys such as those by Serkowski et al. (1975), who performed broadband linear po-

larimetry (BBLP) in the optical filters *UBVR*, and by Whittet et al. (1992), who extended BBLP measurements to the full optical and near-IR *UBVRIJHK* filter set (the results of many BBLP surveys have been collected in a catalogue by Heiles 2000). BBLP surveys have also been carried out in just one filter (e.g. Leroy 1993; Santos et al. 2011), and have been used to explore the boundaries of the Local Cavity (Leroy 1999; Santos et al. 2011) and its possible interaction with a nearby superbubble seen in the direction of the Galactic Centre (Santos et al. 2011). However, since the fraction of interstellar polarisation depends on wavelength, multi-filter measurements are crucial for the physical interpretation of the observations. The amount of linear polarisation is linked to the column density (in very simple terms: the higher the amount of aligned dust along the line of sight, the higher the polarisation) and to the optical properties of the dust, while the wavelength at which the polarisation reaches its maximum depends on the grain size (or size distribution) (Carrasco et al. 1973). The polarisation position angle, if due to a single interstellar cloud with a homogeneous magnetic field, does not change with wavelength, and is determined by the direction of the interstellar magnetic field in the plane of the sky.

<sup>★</sup> Table 2 and reduced data (intensity and polarisation spectra) are available in electronic form at the CDS via anonymous ftp to cdsarc.u-strasbg.fr (130.79.128.5) or via <http://cdsweb.u-strasbg.fr/cgi-bin/qcat?J/A+A/>

While BBLP surveys – historically more common than spectropolarimetric surveys – give substantial insight into the behaviour of interstellar polarisation, better constraints may be obtained with a more refined sampling of the polarisation as a function of wavelength. Compared to multicolour BBLP measurements, spectropolarimetry may allow us to better test if the well-known Serkowski curve provides good fits to the interstellar polarisation, or if polarisation spectra present narrowband features that deviate from it, maybe systematically. Another advantage of spectropolarimetry versus multicolour BBLP is that the former technique allows us to distinguish the contribution of dust from that of gas. Finally, we note that although much effort has been dedicated to the observations of the ISM, many lines of sight have never been observed in polarimetric mode.

Spectropolarimetry is therefore the obvious choice for modern polarimetric surveys, when this mode is available at the telescope. Some initial low-resolution polarisation spectra were presented first by Wolstencroft & Nandy (1971) and later by Wolstencroft & Smith (1984). Anderson et al. (1996) presented spectropolarimetric data in the UV and optical range for 38 objects at a spectral resolution of  $\sim 20$  nm. In the past 25 years, optical spectropolarimetry of the ISM was obtained with the observations of more than 200 stars at the Pine Bluff Observatory near Madison, Wisconsin, USA, using the HPOL spectropolarimeter. The observed spectral range was 320–775 nm, then extended to 1050 nm, with a spectral resolution of 2.5 nm (resolving power  $R \sim 300$ ), then refined to 1 nm ( $R \sim 775$ ). The database of processed data is publicly available<sup>1</sup>, and details of the project are given in Weitenbeck (1999) and Meade et al. (2012). More in-depth insight into the shape, size distribution, and composition of interstellar grains can come from detailed physical models that treat the interaction of dust with photons. For example, Siebenmorgen et al. (2014) presented state-of-the-art models that simultaneously reproduce the observed linear-polarisation curve and the UV/visual extinction curve. These recent studies show that models are more advanced than most ISM polarisation data and make clear that medium-resolution linear spectropolarimetry with a high signal-to-noise ratio (S/N) brings a new perspective to the issue of the dust size distribution and composition in the Galactic ISM. Hence a spectropolarimetry survey is required to develop a comprehensive picture of the exact details of the cosmic dust – initially limited to Galactic environments – and to exhaustively test the new models in their applicability to a statistically representative sample (rather than concentrating on a handful of targets).

These considerations have prompted us to initiate a new spectropolarimetric survey, the Large Interstellar Polarisation Survey (LIPS) in both hemispheres with the Focal Reducer/low-dispersion Spectrograph (FOR2) instrument of the Very Large Telescope (VLT) of the European Southern Observatory (ESO) and the Intermediate-dispersion Spectrograph and Imaging System (ISIS) instrument of the William Herschel Telescope (WHT). LIPS fills a gap in our knowledge of dust properties in diffuse lines of sight, the gaseous content of which is being studied with the ESO Diffuse Interstellar Band Large Exploration Survey (EDIBLES, Cox et al. 2017). The main goal of EDIBLES is to create a detailed inventory of interstellar gas in diffuse clouds and to derive accurate physical conditions in order to determine molecular properties of the unidentified diffuse interstellar bands (Sarre 2006; Cami & Cox 2014). Together with existing UV spectroscopy, LIPS and EDIBLES constitute an ex-

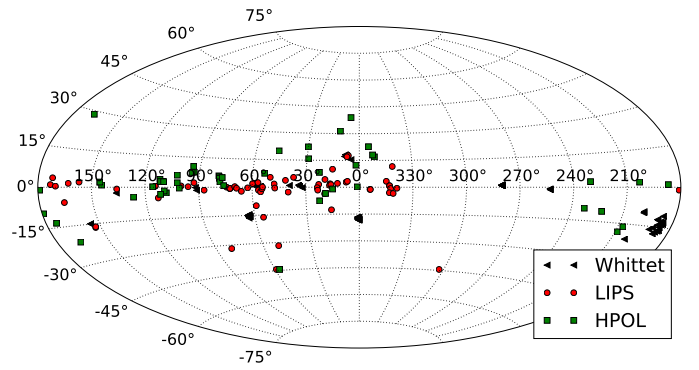


**Fig. 1.** Location of our targets in the Galaxy (red circles) compared to those of other major surveys: HPOL (blue circles) and Whittet et al. (1992) (black triangles).

tensive dataset for interstellar extinction and polarisation, which provides a comprehensive simultaneous view of the properties of the interstellar gas and dust in diffuse interstellar lines of sight.

This paper presents the FOR2 survey in the Southern Hemisphere.

## 2. Observations

### 2.1. Target list

The targets of the FOR2 survey are a set of O- and B-type stars selected from the EDIBLES target list, excluding the brightest stars ( $V \leq 5$  mag) and those accessible with ISIS at the WHT (La Palma), although a few northern targets ( $V \sim 8$  mag) were included for cross-calibration and characterising instrumental effects. The initial set of selected targets covers a wide range of interstellar properties in terms of dust extinction ( $E(B - V) = 0$  to 2 mag,  $R_V = 1.5$  to 6), molecular abundances ( $f(H_2) = 0.0$  to 0.8), radiation fields, gas, and dust temperatures (Cox et al. 2017). To expand the parameter space of dust and environments, additional sightlines in the Magellanic Clouds were added, as well as a few faint ( $V \geq 9$ ) highly reddened Galactic targets that are too faint for the EDIBLES survey. The full target list/observing log is given in Table 1, and their position in Galactic coordinates is shown with red symbols in Fig. 1, which also shows the position of the targets of two other major surveys.

### 2.2. Instrument and instrument settings

FOR2 is a multi-purpose instrument capable of imaging and low-resolution spectroscopy in the optical; it is equipped with polarimetric optics. It is attached at the Cassegrain focus of Unit 1, Antu, of the ESO VLT of the Paranal Observatory. The instrument is described in Appenzeller & Rupprecht (1992) and Appenzeller et al. (1998).

The polarimetric optics are arranged according to the optical design described by Appenzeller (1967). The polarimetric module consists of a retarder waveplate ( $\lambda/2$  for observations of linear polarisation, and  $\lambda/4$  for observations of circular polarisation) followed by a Wollaston prism. The Wollaston prism splits the beam into two components, one linearly polarised along the principal plane of the Wollaston (the parallel beam  $f^{\parallel}$ ), and one linearly polarised perpendicularly to that plane (the perpendicular beam  $f^{\perp}$ ). Following the scheme by Scarrott et al. (1983), a

<sup>1</sup> See <http://www.sal.wisc.edu/HPOL/> and CDS catalogue J/ACa/49/59

6.8' × 22'' Wollaston mask prevents the superposition of the two beams.

### 2.2.1. Grism

Grism 300 V was employed for our observations. With a 0.5'' slit width, it provides a spectral resolving power of about 880. The order-separating filter GG435 may be used to cut off the incoming radiation at  $\lambda \lesssim 435$  nm to avoid second-order contamination from the blue part of the spectrum into the red part (at  $\lambda \gtrsim 650$  nm). However, since our targets are mostly highly reddened, when planning the observations, we assumed that it would probably be safe to observe without order-separating filter, and cover the wavelength range down to  $\sim 360$  nm, which is the blue limit of the spectral range covered by the instrument (for further considerations on the effects of second-order contamination on spectropolarimetric measurements, see Patat et al. 2010). For each star, we therefore decided to obtain an observing series with order-separating filter GG435, and one observing series without it. Observing both with and without order-separating filter allowed us to verify this hypothesis (see Sect. 4), and to have some redundancy in the range 435–650 nm that would serve as a quality check. Our expectation was that the polarised spectra obtained with and without order-separating filter in the wavelength range 435–650 nm would be identical within photon-noise uncertainties, while at  $\lambda \gtrsim 650$  nm, a possible difference between the two would be ascribed to contamination from the second order in the spectra obtained without filter. In fact, since CCD sensitivity drops dramatically at  $\lambda \lesssim 380$  nm, the useful spectral range covered by our observations was finally 380–930 nm with no filter, and 435–930 nm with the filter GG435 inserted.

### 2.2.2. CCD and CCD readout

In service mode, the detector installed in FORS2 is a mosaic composed of two 2k × 4k E2V CCDs (pixel size of 15 × 15  $\mu\text{m}^2$ , pixel scale of 0.125''), optimised for the red. Most of our observations were obtained without rebinning, in order to maximise the  $S/N$  and avoid saturation towards the bright targets, while for certain fainter targets, we used the 2 × 2 rebinning mode.

### 2.3. Observing strategy and data reduction

Our observations were obtained setting the retarder waveplate at four position angles: 0°, 22.5°, 45°, and 67.5°. This implementation of the so-called “beam-swapping technique” allowed us to minimise instrumental effects, as explicitly suggested in the FORS1/2 manual and thoroughly discussed by Bagnulo et al. (2009), for instance.

Stokes  $Q$  and  $U$  parameters are defined as in Shurcliff (1962). In the following, we consider the ratios  $Q/I$  and  $U/I$ , adopting the notation

$$P'_Q = \frac{Q}{I} \quad \text{and} \quad P'_U = \frac{U}{I}. \quad (1)$$

The reduced Stokes parameters  $P'_Q$  and  $P'_U$  were measured by combining the photon counts of the parallel and perpendicular beams ( $f^{\parallel}$  and  $f^{\perp}$ , respectively) observed at retarder waveplate positions  $\alpha = 0^\circ, 22.5^\circ, 45^\circ$ , and  $67.5^\circ$ , as given by the following formula:

$$P'_X = \frac{1}{2} \left\{ \left( \frac{f^{\parallel} - f^{\perp}}{f^{\parallel} + f^{\perp}} \right)_{\alpha=\phi_0} - \left( \frac{f^{\parallel} - f^{\perp}}{f^{\parallel} + f^{\perp}} \right)_{\alpha=\phi_0+45^\circ} \right\}, \quad (2)$$

where  $\phi_0 = 0$  if  $X = Q$  and  $\phi_0 = 22.5^\circ$  if  $X = U$ . The uncertainty due to photon-noise on  $P'_X$  is

$$\sigma_{P'_X}^2 = \left( \left( \frac{f^{\perp}}{f^{\parallel} + f^{\perp}} \right)^2 \sigma_{f^{\parallel}}^2 + \left( \frac{f^{\parallel}}{f^{\parallel} + f^{\perp}} \right)^2 \sigma_{f^{\perp}}^2 \right)_{\alpha=\phi_0} + \left( \left( \frac{f^{\perp}}{f^{\parallel} + f^{\perp}} \right)^2 \sigma_{f^{\parallel}}^2 + \left( \frac{f^{\parallel}}{f^{\parallel} + f^{\perp}} \right)^2 \sigma_{f^{\perp}}^2 \right)_{\alpha=\phi_0+45^\circ}. \quad (3)$$

Assuming that the fluxes in both beams and for all retarder waveplate positions are similar, we obtain

$$\sigma_{P'_X} = \frac{1}{S/N}, \quad (4)$$

where  $S/N$  is the signal-to-noise ratio accumulated in all beams used to calculate  $P'_X$ .

### 2.4. Correction for the chromatism (wavelength dependence) of the retarder waveplate and for instrumental polarisation

The position angle of the retarder waveplate identifies the direction along which the electric field propagates with no phase shift (this is the fast axis of the retarder waveplate). This direction is slightly wavelength dependent, and this deviation introduces a rotation of the measured position angle of the polarisation that may be corrected as explained, for example in Sect. 4.2 of Bagnulo et al. (2009; see also Patat & Taubenberger 2011), that is,

$$\begin{aligned} P_Q &= P'_Q \cos 2\epsilon + P'_U \sin 2\epsilon \\ P_U &= -P'_Q \sin 2\epsilon + P'_U \cos 2\epsilon \end{aligned} \quad (5)$$

where  $\epsilon$  is the deviation angle tabulated in the instrument webpages. The fraction of linear polarisation

$$P = \sqrt{P_Q^2 + P_U^2} \quad (6)$$

is not affected by the problem of the chromatism of the retarder waveplate (i.e.  $P = P'$ ), while the measured position angle  $\theta'$  and the “true” position angle  $\theta$  are simply related by

$$\theta = \theta' - \epsilon. \quad (7)$$

Fossati et al. (2007) and Siebenmorgen et al. (2014) noted that FORS2 spectropolarimetric observations are affected by a small amount of wavelength-dependent instrumental polarisation (mainly in  $Q$ ), which has been further analysed and analytically quantified by Cikota et al. (2017) for grism 300V as

$$\begin{aligned} P_Q^{\text{instr.}} &= 9.66 \times 10^{-8} \lambda + 3.29 \times 10^{-5} \\ P_U^{\text{instr.}} &= 7.28 \times 10^{-8} \lambda - 4.54 \times 10^{-4} \end{aligned} \quad (8)$$

where  $\lambda$  must be expressed in Å. Cikota et al. (2017) derived Eqs. (8) from observations taken with the instrument position angle  $\chi$  set to zero (i.e. with the parallel beam of the Wollaston prism parallel to the north celestial meridian). Various experiments presented by Siebenmorgen et al. (2014) show that FORS2 instrumental polarisation tends to be constant in the instrument reference system; when we wish to express the Stokes parameters in a reference system other than the instrumental one, instrumental polarisation therefore has to be corrected before rotating the Stokes parameters. We assume that Stokes parameters  $P_Q$  and  $P_U$  were measured with the instrument position angle on sky set to a value  $PA$ , counted counterclockwise from the north

celestial meridian (for instance,  $PA$  could correspond to the parallactic angle), and already corrected for the chromatism of the retarder waveplate. To transform the Stokes parameters  $P'_Q, P'_U$  into a new reference system with its reference direction parallel to the north celestial meridian, we have to apply

$$\begin{aligned} P_Q^E &= (P_Q - P_Q^{\text{instr.}}) \cos 2\chi + (P_U - P_U^{\text{instr.}}) \sin 2\chi \\ P_U^E &= -(P_Q - P_Q^{\text{instr.}}) \sin 2\chi + (P_U - P_U^{\text{instr.}}) \cos 2\chi, \end{aligned} \quad (9)$$

where  $P_X$  are given by Eqs. (5),  $P_X^{\text{instr.}}$  are given by Eqs. (8), and  $\chi$  is the angle, counted counterclockwise and looking at the source by which the old (instrument) reference system has to be rotated to coincide with the new (equatorial) reference system (e.g. Landi Degl'Innocenti et al. 2007), that is,  $\chi = -PA$ ,<sup>2</sup> while the fraction of linear polarisation and its position angle are given by

$$\begin{aligned} P &= \sqrt{(P_Q - P_Q^{\text{instr.}})^2 + (P_U - P_U^{\text{instr.}})^2}, \\ \theta^E &= \theta + \chi \end{aligned} \quad (10)$$

where  $\theta$  is given by Eq. (7).

Our final results can be given either using the reduced Stokes parameters  $P_Q$  and  $P_U$  or the fraction of linear polarisation  $P$  and its position angle  $\theta$ . The latter representation is more convenient when the interest is in a map of the polarisation and its direction, for example, as function of the Galactic coordinates, as is our interest here. In our case, it is also convenient to refer the position angle of the polarisation to the direction of the galactic pole. This angle  $\theta^G$  may be obtained for the equatorial position angle  $\theta^E$  as

$$\theta^G = \theta^E + \eta, \quad (11)$$

where

$$\cos \eta = \frac{\cos(\delta) \sin(\delta_G) - \sin(\delta) \cos(\delta_G) \cos(\alpha - \alpha_G)}{\cos(b)}, \quad (12)$$

where  $b$ ,  $\alpha$ , and  $\delta$  are the galactic latitude, right ascension, and declination of the star, respectively, and  $(\alpha_G, \delta_G)$  are the right ascension and declination of the North Galactic Pole.

### 3. Analysis

Our dataset has low photon-noise. Figure 2 shows the histogram of the error bars of the fraction of polarisation  $P$  per nm, obtained after averaging out the spectra obtained with and without order-separating filter. If we were to integrate a broadband filter, these error bars would decrease to the order of a few units in  $10^{-4}$ . As discussed below, these uncertainties are hardly representative of the actual accuracy of our measurements. In this section we describe how we discovered various non-photon-noise errors, and the way we have tried to minimise them.

#### 3.1. Uncertainties due to data reduction

Bagnulo et al. (2012) have discussed the noise due to data reduction, meaning that different but still reasonable choices in the way data are treated lead to (slightly) different results. In

<sup>2</sup> The instrument position angle counted counterclockwise on sky from the north celestial meridian,  $\chi_{\text{instr.}}$ , is given by the FORS2 fits-header keyword ADA.POSANG taken with the opposite sign ( $\chi_{\text{instr.}} = -\text{ADA.POSANG}$ ), hence in Eqs. (9),  $\chi = \text{ADA.POSANG}$  should be used.

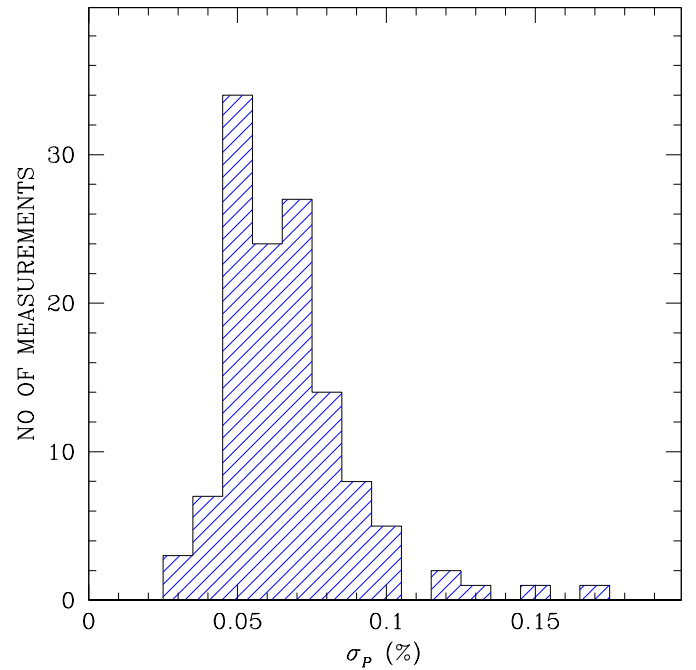


**Fig. 2.** Histogram of the photon-noise error bars of the linear polarisation  $P$  per nm, in the wavelength range where the  $S/N$  is highest (typically around 500 nm).

case of measurements with a very high  $S/N$ , these differences may sometimes be comparable to photon noise, especially in the presence of sharp spectral features (such as emission lines of the telluric  $O_2$  bands). As a first check, we decided to verify whether the differences between the products of independent data reduction were random and well within the photon noise. A dozen observations were reduced independently by two of us (SB and AC), and results were compared. The reduction methods differed mainly in the way background and flux extraction were treated: in one case, no background was subtracted (since the exposure time was very short) and wavelength calibration was carried out on the extracted spectra; in another case, the background was removed and wavelength calibration performed on the 2D spectra. The final products were found perfectly consistent in the continuum; an example is shown in Fig. 3. The two different reductions led to discrepant results around the sharp features discussed in Sect. 3.3, and they are due to a different spectral sampling/rebinning.

#### 3.2. Inconsistencies between consecutive observations

All our stars were observed consecutively with and without order-separating filter. In some cases, the polarisation spectra measured in the wavelength range common to the two instrument setups were found inconsistent among themselves, in that the polarisation spectra obtained with and without filter would appear systematically shifted by a quantity much larger than the photon-noise error bars. The most dramatic example in our database is represented by the observations of HD 149404 obtained on 2015 May 5, shown in Fig. 4, where the red empty circles refer to the polarisation measured with the order-separating filter, the blue solid circles to the polarisation measured without filter, and the solid black line to their average calculated as explained later in this section. In this example, the polarisation

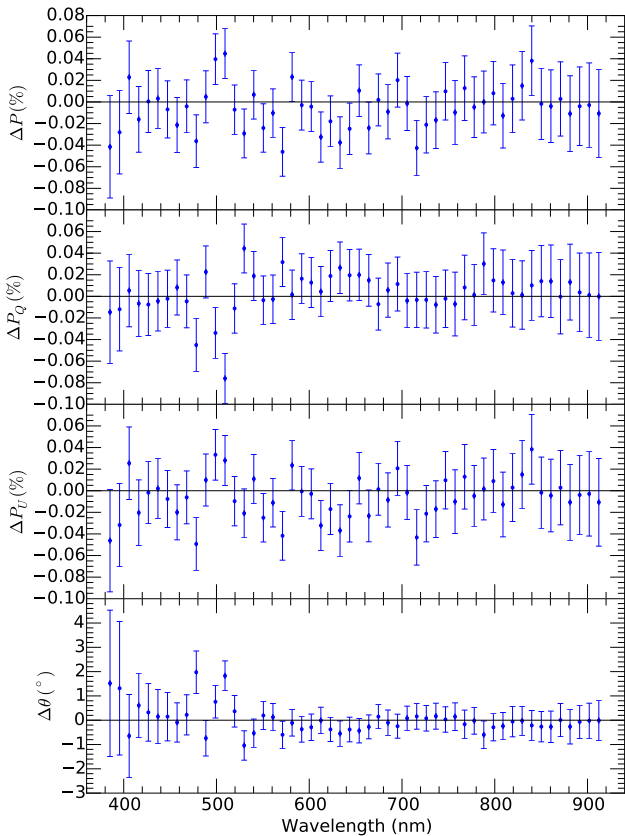


**Fig. 3.** Residuals of independently reduced data, plotted with photon-noise error bars.

measured with the order-separating filter appears systematically higher ( $\Delta P \simeq 0.1\%$ ) than that observed without filter.

HD 149404 is a detached massive O-star binary (O7.5 If + ON9.7 I), with a period of 9.81 d (Massey & Conti 1979). Previous literature data show that HD 149404 exhibits polarimetric variability, but on a much longer timescale than the interval of time between our two observations: Luna (1988) obtained BBLP in the B filter, finding that the fraction of linear polarisation is nearly constant with time, but the position angle changes periodically, so that the polarisation variation in the  $P_Q$ - $P_U$  plane shows a nearly circular pattern. However, it is unlikely that the differences observed in two observing series obtained within a few minutes from each other have an origin intrinsic to the source. We also note that the pairs of observations of the same star obtained on 2016 January 30 are fully consistent among themselves, therefore we conclude that the variability observed on 2015 May 5 has an instrumental origin.

Numerical simulations performed by Cikota et al. (2017, presentation at the ESO Calibration Workshop) suggested that this short-timescale variability could be linked to an inaccurate setting of the retarder waveplate.

The idea of Cikota et al. (2017) may be tested analytically starting from Eqs. (34) and (36) of Bagnulo et al. (2009), assuming that the chromatism of the retarder waveplate and of the Wollaston prism are perfectly corrected, that is, by setting  $\delta\alpha = \delta\beta = 0$  in the expressions of  $\widehat{\mathcal{G}}_X$  of Eqs. (34), assuming a perfect flat-field ( $\delta h = 0$ ) and assuming that the phase shift introduced by the retarder waveplate is exactly  $180^\circ$  ( $\delta\gamma = 0$ ), but associating with each position  $\alpha$  of the retarder waveplate an indetermination  $\delta_\alpha$ . Using Eqs. (34) and (36) of Bagnulo et al.

(2009), setting  $N = 1$ , and considering the retarder waveplate at the angles  $0^\circ + \delta_0$ ,  $22.5^\circ + \delta_{22.5}$ ,  $45^\circ + \delta_{45}$ ,  $67.5^\circ + \delta_{67.5}$ , we find that the measured parameters  $\widehat{P}_Q$ ,  $\widehat{P}_U$  are connected to the “true” parameters  $P_Q$  and  $P_U$  via

$$\begin{aligned} \widehat{P}_Q &= P_Q + 4P_U \frac{1}{2} (\delta_0 + \delta_{45}) \\ \widehat{P}_U &= P_U - 4P_Q \frac{1}{2} (\delta_{22.5} + \delta_{67.5}) . \end{aligned} \quad (13)$$

Equations (13) show that the inaccuracy of the setting of the retarder waveplate is responsible for a cross-talk from  $P_Q$  to  $P_U$  and vice versa. According to the signs of the actual reduced Stokes parameters and of the difference between actual and nominal position of the retarder waveplate, the measurement may be either an over-estimate or an under-estimate of the “true” polarisation. In particular, we can write

$$\begin{aligned} \text{rms}^2(\widehat{P}_Q - P_Q) &= 4P_U^2 (\text{rms}^2(\delta_0) + \text{rms}^2(\delta_{45})) \\ \text{rms}^2(\widehat{P}_U - P_U) &= 4P_Q^2 (\text{rms}^2(\delta_{22.5}) + \text{rms}^2(\delta_{67.5})) , \end{aligned} \quad (14)$$

and assuming a constant rms  $\delta$  for all waveplate positions, we obtain

$$\begin{aligned} \text{rms}(\widehat{P}_Q) &= 2\sqrt{2} |P_U| \text{rms}(\delta) \\ \text{rms}(\widehat{P}_U) &= 2\sqrt{2} |P_Q| \text{rms}(\delta) . \end{aligned} \quad (15)$$

The FORS2 User Manual states that the accuracy of the setting of the retarder waveplate is  $\sim 0.1^\circ$ . This means, for instance, that the expected absolute uncertainty in the  $P_Q$  measurement of a source with  $P_U = 1\%$  is  $0.005\%$ . We note that by using Eqs. (34) and (36) of Bagnulo et al. (2009), we have considered the case in which the reduced Stokes parameters are calculated with the difference method. Similar results would apply by adopting the ratio method, as can be verified by using Eqs. (40) and (41) of Bagnulo et al. (2009). In the following, we test whether these uncertainties may be responsible for the observed discrepancies.

In case of two consecutive measurements (1) and (2), we have

$$\begin{aligned} \text{rms}\left(\frac{\widehat{P}_Q^{(2)} - \widehat{P}_Q^{(1)}}{8P_U}\right) &= \text{rms}(\delta) \\ \text{rms}\left(\frac{\widehat{P}_U^{(2)} - \widehat{P}_U^{(1)}}{8P_Q}\right) &= \text{rms}(\delta) . \end{aligned} \quad (16)$$

From our dataset we calculated the BBLP value in the V filter (see Sect. 3.4.3) and measured the distributions of the quantities

$$\frac{180}{\pi} \frac{\widehat{P}_Q^{(2)} - \widehat{P}_Q^{(1)}}{8P_U} \quad \text{and} \quad \frac{180}{\pi} \frac{\widehat{P}_U^{(2)} - \widehat{P}_U^{(1)}}{8P_Q} ,$$

where the “true” parameters  $P_X$  ( $X = Q, U$ ) were approximated by  $(\widehat{P}_X^{(1)} + \widehat{P}_X^{(2)})/2$ . We report these distributions in form of histograms in Fig. 5. These distributions were found approximately centred about zero (as expected), but could not be represented by Gaussian distributions with  $\sigma = 0.1^\circ$ . We then decided to remove the points for which the denominator was  $\leq 0.5\%$ , finding the Gaussian best fits with  $\sigma = 0.28^\circ$  and  $0.35^\circ$ , respectively. Although these values are still about three times higher than the uncertainty declared in the FORS User Manual, our considerations analytically support the conclusion by Cikota et al. (2017) that an inaccuracy of the setting of the retarder waveplate is responsible for the discrepancies that we found in our dataset.

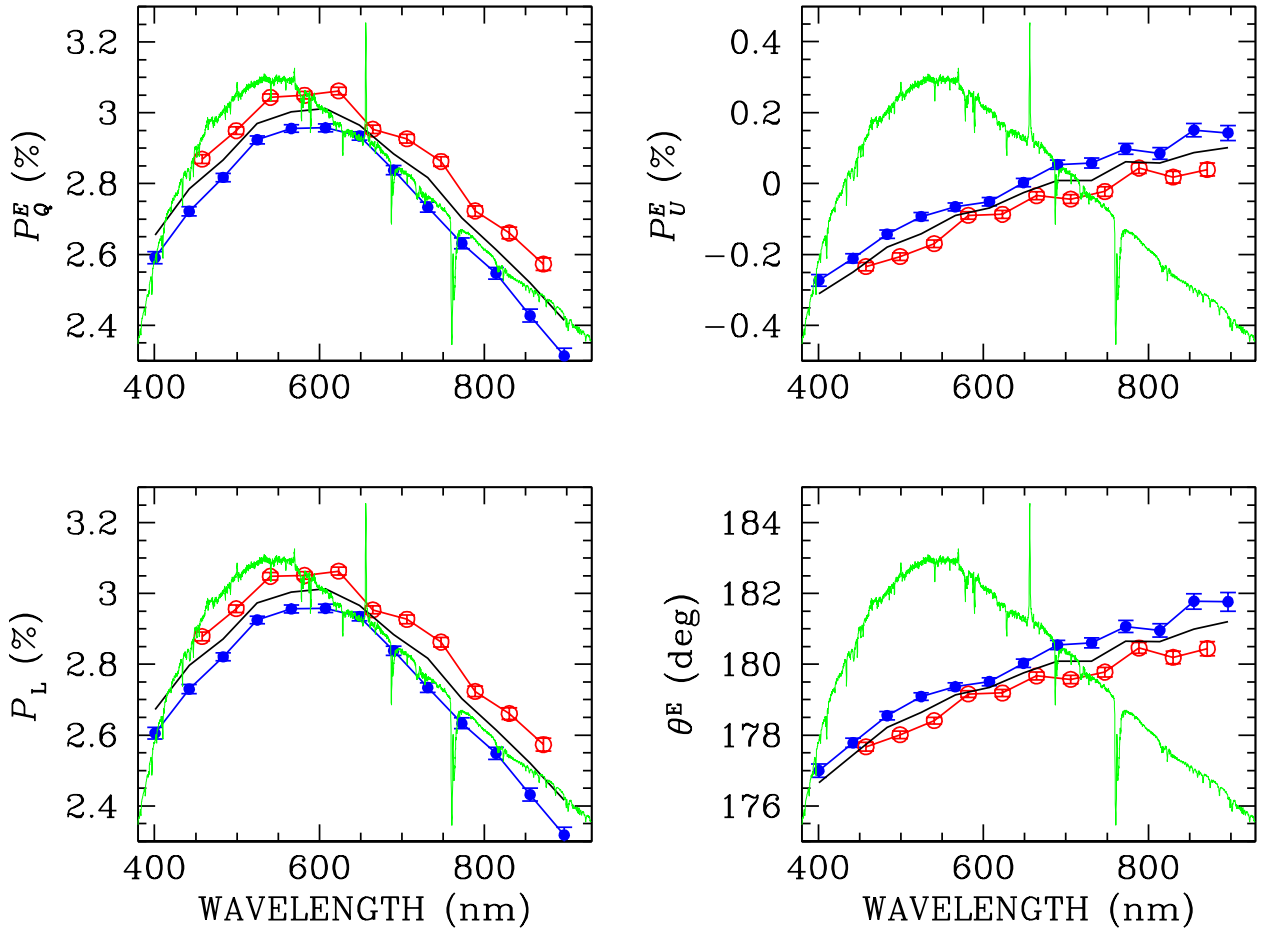


**Fig. 4.** Observations of star HD 149404 obtained on 2015-05-12. The top left panel shows  $P_Q^E$ , the top right panel shows  $P_U^E$ , the bottom left panel shows  $P_L$ , and the bottom right panel shows  $\theta_E^E$ . In each panel, red empty circles refer to the observations obtained with order-separating filter, and blue solid circles refer to the observations obtained without order separating filter, with a 41.4 nm wavelength bin size. The black solid line is their average obtained from Eqs. (17). The green solid line (in arbitrary units and identical in all panels) shows the stellar flux not corrected for instrument+telescope transmission function, and with a 0.7 nm bin size. Error bars due to photon noise are smaller than or comparable to the symbol size, but the shape of the SED may help to visualise how the photon-noise error bars, which are proportional to the inverse of the S/N, change with wavelength.

### 3.3. Spikes in the polarisation spectra

Our polarisation spectra exhibit some departures from a smooth behaviour, some of which are due to cosmic rays. Cosmic rays are generally not well removed during flux extraction because models of the line spread function (LSF) may not be accurate enough compared to the small polarimetric signals that we intend to measure, leaving some spurious spikes randomly distributed in wavelength.

Spikes appear more frequently in proximity of sharp spectral lines (e.g. strong H emission lines), or telluric bands (e.g. O<sub>2</sub>-A band at 760 nm), in the form of a sharp increase or decrease of the polarisation, and/or a sudden change in position angle. In several cases, polarimetric spikes appear in the observations obtained with the order-separating filter, but not in those obtained without filter, or vice versa. Only rarely are they present in both datasets, and their shape and amplitude largely depends on spectral sampling and rebinning. Most of these features are probably spurious and are caused by a tiny offset that is introduced either by imperfect wavelength calibration or by instrument flex-

ures, which creates a difference in the fluxes measured in the spectral bins of different beams when the flux changes rapidly with wavelength. Similar problems were found in FORS circular polarisation measurements and were discussed by Bagnulo et al. (2013). However, there might be situations in which the spikes that we have detected are real. For instance, in stars with emission lines (e.g. Be stars), the observed linear polarisation is probably due to a combination of the contribution from interstellar and disc scattering. Strong emission lines may dilute the radiation polarised in the circumstellar disc, causing a change in polarisation. To determine which of these spikes (if any) are real or if real features are hidden behind spurious spikes requires observations with much higher spectral resolution obtained with a very stable instrument, such as ESPaDOnS at the CHFT or HARPSpol of the La Silla Observatory.

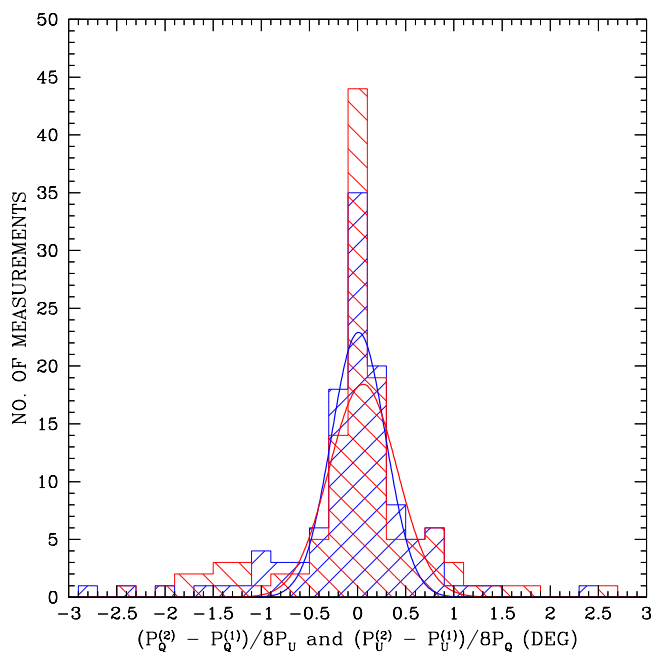


**Fig. 5.** Histograms of two distributions used to estimate the uncertainty due to an imperfect setting of the retarder waveplate (see text) and their best fits with Gaussian distributions. Blue lines correspond to the data obtained without order-separating filter, and red lines to the data obtained with GG435 filter. Best fits were obtained using data with  $|P_Q| \geq 0.5\%$  and  $|P_U| \geq 0.5\%$ , respectively, as explained in the text.

### 3.4. Presenting the results

#### 3.4.1. Averaging the observations

The uncertainties introduced by random misalignments of the retarder waveplate discussed in Sect. 3.2 may be reduced by increasing the number of waveplate positions at which the retarder waveplate is set during the observing sequence, for example, by considering a sequence  $0^\circ, 22.5^\circ, \dots, 157.5^\circ$  instead of  $0^\circ, 22.5^\circ, 45^\circ, \text{ and } 67.5^\circ$ . Unfortunately, our observing strategy was decided before we discovered the accuracy problem of the retarder waveplate setting, therefore our observations were carried out using only four positions of the retarder waveplate. However, the accuracy of our polarisation spectra may still be improved by adopting the average of the measurements obtained with and without order-separating filter. The spectral range 380–435 nm is covered only by the observations without order-separating filter. In this interval range, we therefore adopted the sum of the reduced Stokes parameters measured without filter and the average of the half-difference between the  $P_Q$  and  $P_U$  values measured with and without filter in the common wavelength range ( $\lambda \geq 435$  nm). In other words, we have adopted

$$\begin{aligned} P_X &= \frac{1}{2} (P_X^{(2)} + P_X^{(1)}) & \text{if } \lambda \geq 435 \text{ nm} \\ P_X &= P_X^{(2)} + \frac{1}{2N} \sum_{i=1}^N (P_X^{(1)}(\lambda_i) - P_X^{(2)}(\lambda_i)) & \text{if } \lambda < 435 \text{ nm}, \end{aligned} \quad (17)$$

where the index (1) refers to the observations obtained with order-separating filter, and the index (2) refers to those obtained without filter.

#### 3.4.2. Rebinning

Most of our targets are very bright, and it is in principle possible to reach extremely high  $S/N$  with a very short exposure time. The ADU converter sets an upper limit to the  $S/N$  that may be reached per pixel bin, which in general depends on CCD gain, on the full-well capacity, on the seeing conditions (when seeing is worse, the flux may be spread over more pixels, and this increases the flux that may be measured before saturation is reached, simply by increasing the exposure time), and on the number of frames that are obtained per target. For each frame with  $1''$  seeing conditions and with a converting factor  $1.25 \text{ e}^- \text{ ADU}^{-1}$ , the maximum  $S/N$  that can be reached in the wavelength bin that corresponds to the dispersion bin is  $\sim 800$ . Adding the flux accumulated in two beams and in two frames, this corresponds to an error bar  $\sigma_X \sim 0.06\%$ . Typically, our frames were exposed at 20–30% of the maximum, and each observing series consisted of two frames per Stokes parameter. Therefore, our typical error bar per spectral bin in each Stokes parameter was 0.12–0.15%. Our spectral resolution of 880 is preserved up to a rebinning of two 0.161 nm pixels, but when no narrow spectral features are present in our spectra, it makes sense to consider heavier rebinning. We experimented by combining the signals of 2, 4, 8, 16, 32, 64, 128, and 256 spectral bins, and for our figures we decided to adopt a 20.6 nm bin for a formal uncertainty due to photon noise of 0.01–0.02%.

We should note that rebinning must be performed on the fluxes  $f^{\parallel}$  and  $f^{\perp}$  before combining the flux to obtain the  $P_Q$  and  $P_U$  spectra since

$$\frac{\sum_{i=1}^N (f^{\parallel}(\lambda_i) - f^{\perp}(\lambda_i))}{\sum_{i=1}^N (f^{\parallel}(\lambda_i) + f^{\perp}(\lambda_i))} \neq \sum_{i=1}^N \frac{f^{\parallel}(\lambda_i) - f^{\perp}(\lambda_i)}{f^{\parallel}(\lambda_i) + f^{\perp}(\lambda_i)}.$$

We note also that in case of low polarisation signals, the fraction of linear polarisation pertaining to a larger bin size may appear to be lower than the average of the polarisation signal plotted with a smaller bin size. An example of this situation is given in Fig. 6, which shows a polarisation spectrum with a wavelength bin size of 0.16 nm (corresponding to one CCD pixel) and the polarisation spectrum of the same star rebinned to a 20.6 nm bin size. The reason for this apparent inconsistency is that the  $P$  distribution may be approximated with a Gaussian distribution only for  $P \gg \sigma_P$ , a condition that may not be satisfied by the signal accumulated in a small wavelength bin. For the same reason, the best fit to  $P$  with a Serkowski curve with a least-squares technique must be performed on spectra that have been rebinned so that for each spectral bin  $P \gg \sigma_P$ . In previous literature, for example, Whittet et al. (1992), this problem was mitigated by adopting the correction formula derived by Wardle & Kronberg (1974) and by Clarke & Stewart (1986), namely

$$P^{(c)} = P \left[ 1 - \left( \frac{\sigma_P}{P} \right)^2 \right]^{\frac{1}{2}}, \quad (18)$$

but in our case, after rebinning at 20.6 nm, we found  $\sigma_P/P \ll 1$  was always valid, in particular, that  $\sigma_P/P \leq 10$  in all spectral bins of all our targets, even in the bluest spectral regions where the  $S/N$  is lowest.

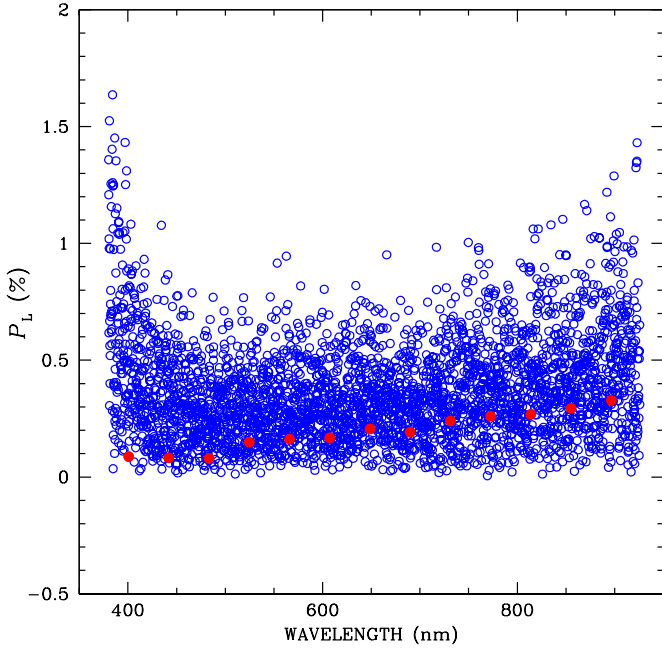


**Fig. 6.** Observations of the low-polarisation star HD 101065. The empty blue circle shows the linear polarisation with the original bin size of 0.16 nm. Red solid circles show the polarisation values obtained after rebinning  $f^{\parallel}$  and  $f^{\perp}$  into  $\sim 20$  nm size bins.

### 3.4.3. Synthetic broadband linear polarisation

For comparison with previous and future BBLP measurements, we calculated for each filter  $F$  of *BVRI*

$$\begin{aligned} P_Q(F) &= \frac{\int_0^{\infty} d\lambda P_Q(\lambda) I_Q(\lambda) T_F(\lambda)}{\int_0^{\infty} d\lambda I_Q(\lambda) T_F(\lambda)} \\ P_U(F) &= \frac{\int_0^{\infty} d\lambda P_U(\lambda) I_U(\lambda) T_F(\lambda)}{\int_0^{\infty} d\lambda I_U(\lambda) T_F(\lambda)} \end{aligned} \quad (19)$$

where  $T_F$  is the transmission function of the  $F$  filter<sup>3</sup>, and

$$\begin{aligned} I_Q &= (f^{\parallel} + f^{\perp})|_{\alpha=0^\circ} + (f^{\parallel} - f^{\perp})|_{\alpha=45^\circ} \\ I_U &= (f^{\parallel} + f^{\perp})|_{\alpha=22.5^\circ} + (f^{\parallel} - f^{\perp})|_{\alpha=67.5^\circ} \end{aligned} \quad (20)$$

### 3.5. Fitting the polarisation spectra with the Serkowski curve

The wavelength dependence of linear polarisation due to interstellar dust is usually well fit by the Serkowski curve introduced by Serkowski (1973)

$$\frac{P(\lambda)}{P_{\max}} = \exp \left[ -K \ln^2 \left( \frac{\lambda_{\max}}{\lambda} \right) \right], \quad (21)$$

where  $\lambda_{\max}$  is the wavelength where the polarisation reaches its maximum  $P_{\max}$ , and  $K$  is a constant that controls the half-width of the curve. The values of  $P_{\max}$  (generally of a few units per cent at most) and  $\lambda_{\max}$  (typically between 400 and 800 nm) depend on the position of the star (distance and galactic coordinates).

Although alternative functional forms have been proposed to describe the interstellar polarisation curve (see for example Wolstencroft & Smith 1984 and Efimov 2009), only the Serkowski-

<sup>3</sup> <http://www.eso.org/sci/facilities/paranal/instruments/fors/inst/Filters/curves.html>

curve parameters are presented here for comparison to the literature. Linear polarisation spectra are publicly available<sup>4</sup> to facilitate future comparisons, dust modelling, and analysis.

We have applied a least-squares technique by minimising the expression

$$\chi^2 = \sum_i^N \frac{(y_i - A - B x_i - C x_i^2)^2}{\sigma_i^2}, \quad (22)$$

where

$$\begin{aligned} x_i &= \ln(\lambda_i) \\ y_i &= \ln(P(\lambda_i)) \\ \sigma_i &= \sigma_P/P(\lambda_i) \\ A &= \ln P_{\max} - K \ln^2 \lambda_{\max} \\ B &= 2K \ln \lambda_{\max} \\ C &= -K, \end{aligned}$$

hence

$$\begin{aligned} K &= -C, \\ \lambda_{\max} &= \exp \left( -\frac{B}{2C} \right), \\ P_{\max} &= \exp \left( A - \frac{B^2}{4C} \right), \end{aligned}$$

and the parameter errors are

$$\begin{aligned} \sigma_K^2 &= \sigma_{CC}^2 \\ \sigma_\lambda^2 &= \frac{1}{4C^2} \exp \left( -\frac{B}{C} \right) (C^2 \sigma_{BB}^2 + B^2 \sigma_{CC}^2 - 2BC \sigma_{BC}) \\ \sigma_P^2 &= \frac{1}{16C^4} \exp \left( 2A - \frac{B^2}{2C} \right) (16C^4 \sigma_{AA}^2 + 4B^2 C^2 \sigma_{BB}^2 + B^4 \sigma_{CC}^2 + \\ &\quad -16BC^3 \sigma_{AB}^2 + 8B^2 C^2 \sigma_{AC}^2 - 4B^3 C \sigma_{BC}^2), \end{aligned}$$

where  $\sigma_{XY}$  ( $X, Y = A, B, C$ ) are the elements of the inverse of the  $\chi^2$  matrix. Since photon noise alone underestimates the actual error bars, the best-fit parameter uncertainties were finally multiplied by  $(\chi^2/\nu)^{1/2}$ , where  $\chi^2$  is given by Eq. (22) and  $\nu$  is the number of degrees of freedom, as discussed by (Bagnulo et al. 2012).

### 3.6. Fitting the polarisation position angle

In many cases, the polarisation position angle was found to be slightly wavelength dependent. In order to quantify the deviations from a constant value, we decided to fit the position angle  $\theta^E(\lambda)$  with a straight line and to consider the slope of this line in addition to the Serkowski parameters.

## 4. Results

Table 2 shows the values obtained by calculating from our polarisation spectra synthetic BBLP values in the *BVRI* filters, as well as the best-fit parameters  $K$ ,  $\lambda_{\max}$ ,  $P_{\max}$ , and  $d\theta^E/d\lambda$ . Photon-noise error bars in the broadband values are virtually negligible ( $\sim 10^{-4}$ ), and the accuracy of our measurements is limited by non-photon noise, as discussed in Sect. 3.2. All our polarisation spectra are shown in the figures of the Appendix in the form of  $P$  and  $\theta^E$  plots. We set the same  $P$ -axis range (1.5%) and  $\theta^E$  range (40°) to facilitate visual comparison. In some cases, the  $P$  range was expanded to 3.0% or 3.5%, and the  $\theta^E$  range to 80° or 120°. To facilitate the comparison between plots with different  $y$ -scales, we adopted identical tick sizes throughout (0.1/0.5%). We note also that the figures are sorted by RA, but with some

<sup>4</sup> See footnote to the title.



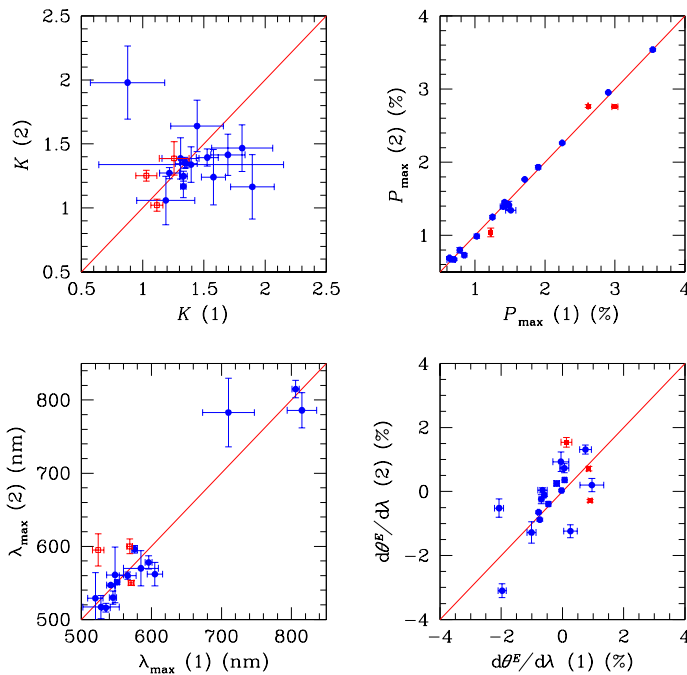


**Fig. 7.** Comparison of the best-fit parameters of the Serkowski curve and the position-angle gradient from pairs of observations of the same stars obtained with FORS2 at different epochs. The red empty squares correspond to three stars that are likely polarimetric variables, namely HD 149404, HD 153919, and HD 116852 (see Sect. 6.4.2).

exceptions, in order to display in the same row the observations of the same star obtained in different epochs. Stellar fluxes (not corrected for atmosphere and instrument+telescope transmission function) are also plotted in arbitrary units both in the  $P$  and in the  $\theta^E$  panels.

Around the telluric  $O_2$  A-band (759–770 nm) in some polarisation spectra, we note a depolarisation of the continuum. In other cases, the polarisation across a sharp spectral emission line increases and changes direction. In these cases, the best-fit parameters of the Serkowski curve were calculated after interpolating the continuum. These spectral regions were not used to calculate the BBLP measurements given in Table 2 or for the best fit with the Serkowski curve.

We did not fit any of the stars with  $P_{\max} \leq 0.70\%$  with the Serkowski curve. We finally note that the following stars have very low (but non-zero) polarisation values: HD 50820 (0.1–0.2%), HD 101065 (0.1–0.2%), HD 105416 (0.2%), HD 115842 (0.4%), HD 134591 (0.3–0.4%), and HD 152424 (0.0–0.4%).

## 5. Quality checks

### 5.1. Consistency of the observations of stars observed at more than one epoch

Some of our targets have been observed at more than one epoch: 25 stars were observed twice and one target was observed three times. The consistency between these observations can be checked in Table 2 and by visual inspection of the figures in the Appendix. A direct comparison of the Serkowski curve parameters and of the position-angle gradient is shown in Fig. 7. Three of the targets are probably polarimetrically variable (see Sect. 6.4.2) and are highlighted with special symbols in the fig-

ure. Except for these three cases, the consistency of the  $\lambda_{\max}$  and  $P_{\max}$  parameters recovered from different datasets is generally very good, while the consistency of the  $K$  parameter and of the gradient of the polarisation angle appears less satisfactory.

### 5.2. Consistency with previous work

Only a few stars in our sample have previously been observed in polarimetric mode. Six stars have been observed with HPOL, and Fig. 8 shows the comparison between our observations and HPOL observations for two of them, HD 147888 and HD 161056. HD 37903 was also observed in spectropolarimetric mode with FORS2 by Siebenmorgen et al. (2014). For another five stars, BBLP measurements were available in the literature. A good but not perfect agreement was found, as demonstrated in Table 3, which shows a comparison between the Serkowski best-fit parameters obtained from this work and those from previous works.

## 6. Discussion

In this section we present an initial qualitative discussion of our results, in particular in comparison with previous works.

### 6.1. Galactic polarisation map

The most immediate way to globally visualise our data is to plot a polarisation map as a function of galactic coordinates. This is done in Fig. 9 for our new FORS2 data (top panel), the data from HPOL (middle panel), and those from Whittet et al. (1992) (bottom panel). Pending accurate Gaia distances for the targets in this survey (Gaia Collaboration et al. 2016), we do not show distance-longitude distribution plots.

### 6.2. Relationships between the best-fit parameters $K$ and $\lambda_{\max}$ of the Serkowski curve

In this section we discuss the relationship between the free-parameters  $K$  and  $\lambda_{\max}$  of Eq. (21) obtained as explained in Sect. 3.5 from our dataset, and we compare our results with those previously obtained in the literature.

In some earlier works, the value of  $K = 1.15$  originally introduced by Serkowski (1973) was assumed as a standard. Eventually, it was found that infrared polarimetric data could not be fitted by adopting this fixed value for  $K$  (Dyck & Jones 1978; Wilking et al. 1980), and  $K$  was considered as a free parameter. Wilking et al. (1980) found a correlation between  $\lambda_{\max}$  and  $K$ : the normalised polarisation curve would be narrowing as  $\lambda_{\max}$  increases. Wilking et al. (1980) suggested to adopt

$$K = 1.7 \lambda_{\max},$$

and later, Whittet et al. (1992) suggested the relationship

$$K = (0.01 \pm 0.05) + (1.66 \pm 0.09) \lambda_{\max}, \quad (23)$$

where in both Eqs.  $\lambda_{\max}$  is expressed in  $\mu\text{m}$ . Figure 10 shows the relationship between best-fit values of  $K$  and  $\lambda_{\max}$  from our survey and those obtained from the dataset by Whittet et al. (1992) and HPOL. It clearly appears that our data (red circles) and those from HPOL (blue circles) are located in the same region of the  $\lambda_{\max} - K$  plane, but none of these two datasets follows the linear trend seen in Whittet et al. (1992) data (black symbols).

The question now is whether this discrepancy is due to different features of the ISM in the regions probed by the different

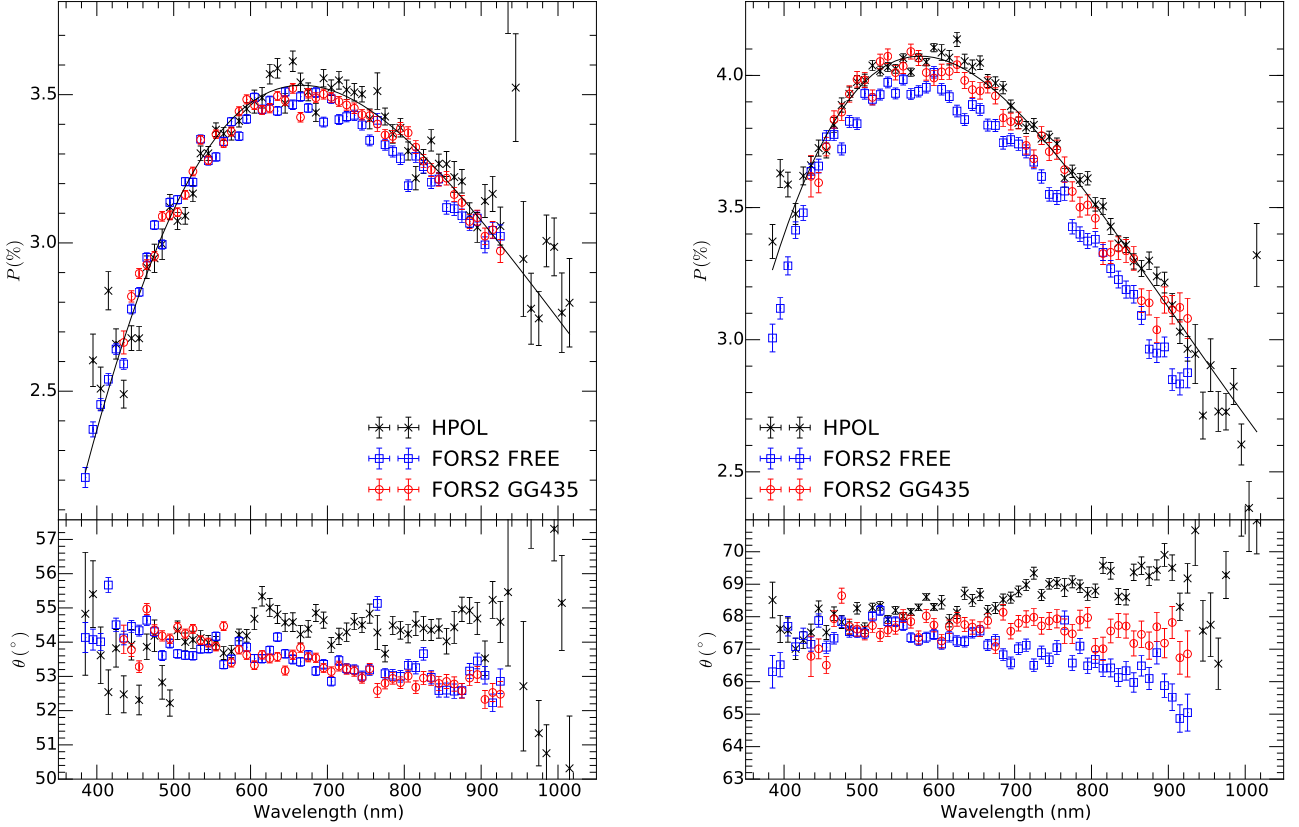


**Fig. 8.** Comparison between FORS2 (blue and red symbols) and HPOL (black symbols) data. Black solid lines are best fits with the Serkowski curve to the HPOL data. *Left panel:* HD 147888. *Right panel:* HD 161056.

surveys, or whether it is an artefact due to either photon noise or systematic error. We should keep in mind that the results of Sects. 5.1 and 5.2 suggest that while the  $P_{\max}$  and  $\lambda_{\max}$  values retrieved from different datasets are generally consistent among themselves, the recovery of the  $K$  parameter, representing the width of the polarisation spectrum, seems less robust. We note that these inconsistencies cannot be due to the issues with the positioning of the retarder waveplate discussed in Sect. 3.2, as they would not affect the ratio  $P(\lambda)/P_{\max}$  of Eq. (21).

To answer to this question, we first studied whether the observed discrepancy may be an artefact caused by the shorter wavelength range of our observations compared to those of Whittet et al. (1992), which extends into the  $U$  filter and into the near-IR. Clarke & Al-Roubaie (1983) indeed suggested that the estimated  $\lambda_{\max} - K$  correlation depends on the wavelength range in which the observations are carried out. For instance, by adopting the  $UBVR$  polarimetric data from Serkowski et al. (1975), Clarke & Al-Roubaie (1983) found that  $K$  and  $\lambda_{\max}$  are anti-correlated. By considering another  $UBVR$  literature dataset, they again obtained a linear relationship with a negative slope, which is opposite to what has been found by Wilking et al. (1980). However, using all available data within the wavelength range from 330 to 950 nm, Clarke & Al-Roubaie (1983) found a positive correlation between  $K$  and  $\lambda_{\max}$ . Inspired by these earlier tests, we performed a similar experiment. We fitted the Whittet et al. (1992) dataset discarding data obtained with the  $U$  and  $JHK$  filters, and considering only those obtained with the  $BVRI$  filters. With this subset, we were still able to recover a loosely linear relationship between  $K$  and  $\lambda_{\max}$  but opposite to that given by Eq. (23) and closer to the relationship found with our survey

(see Fig. 11 and compare it with Fig. 10). This result is in agreement with the previous studies of Clarke & Al-Roubaie (1983), and suggests that the lack of consistency between our results and those from Whittet et al. (1992) may indeed be an artefact that is due to the different wavelength coverage of the datasets.

To further investigate this issue, we performed Monte Carlo simulations in order to test which types of observational constraints are needed to retrieve a linear relationship between  $K$  and  $\lambda_{\max}$ . We generated a number of initial Serkowski-curve parameter values  $\lambda_{\max}$ ,  $P_{\max}$ , and  $K$  randomly selected within these limits:  $470 \text{ nm} \leq \lambda_{\max} \leq 730 \text{ nm}$ , and  $1.4 \leq P_{\max} \leq 5.8$ . The parameter  $K$  was then calculated via Eq. (23). We then generated artificial polarisation spectra with 100 nm wavelength bins in the spectral range 400 to 900 nm using the Serkowski curve, and we scattered all data points according to a Gaussian distribution with  $\sigma = 0.1\%$ . Then we fitted our artificially generated polarisation spectra with a Serkowski curve, adopting  $\lambda_{\max}$ ,  $P_{\max}$  and  $K$  as free parameters, and we used our best-fit parameters to create a new  $\lambda_{\max} - K$  plot. The results are shown in the left panel of Fig. 12, where the black solid line represents the relationship given by Whittet et al. (1992), the black dots correspond to the  $K$  and  $\lambda_{\max}$  parameters scattered around this relationship, the red dots show their values as recovered after our numerical simulation of photon noise, and the red solid line represents the best fit to the recovered  $K$  and  $\lambda_{\max}$  parameters. These results are consistent with our previous finding that measuring BBLP in only four filters does not allow us to recover the linear relationship between  $K$  and  $\lambda_{\max}$ , while when adding three additional data points in the near-IR, we were able to recover it.

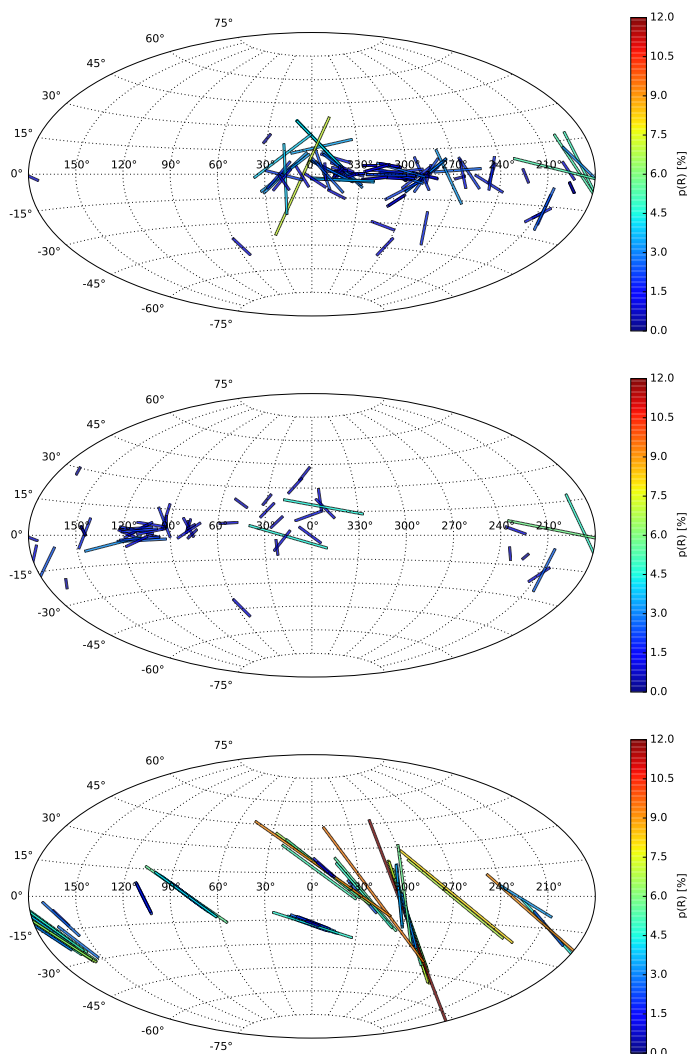


**Fig. 9.** Polarisation map of our Galaxy from our data (top panel), from HPOL data (middle panel), and from Whittet et al. (1992) (bottom panel). The length of the segments is directly proportional to the fraction of linear polarisation.

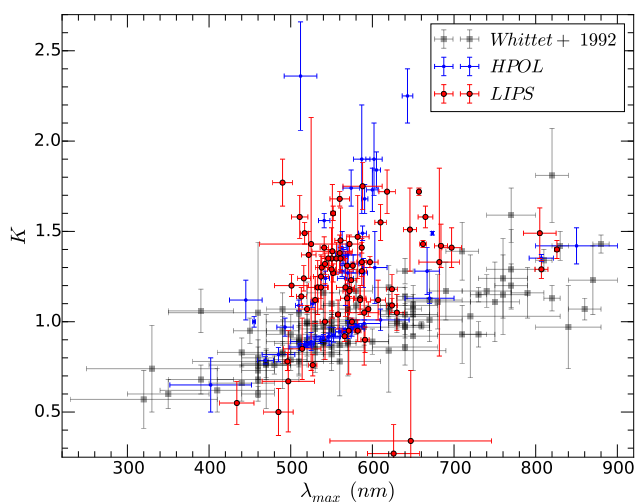


**Fig. 10.**  $K$  vs.  $\lambda_{\max}$  from the best fit obtained with the Serkowski curve using the targets of this survey (red symbols), HPOL data (blue symbols), and data from Whittet et al. (1992) (black symbols).

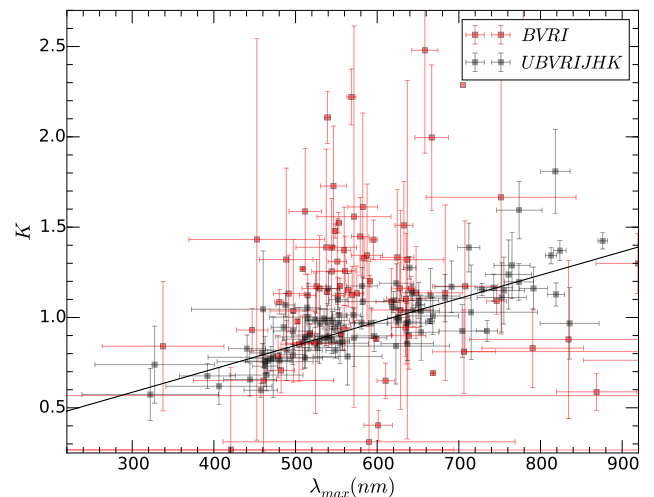


**Fig. 11.** Relationship between  $K$  and  $\lambda_{\max}$  using all *UBVRJHK* filters of Whittet et al. (1992) (black symbols, as in Fig. 10), and using only their *BVRI* photometry (red symbols).

Next we performed a numerical simulation to investigate the LIPS database. We repeated the same experiment as before, but using a 20 nm step size instead of 100 nm, still associating a 0.1 % error bar per spectral bin. For comparison with our real dataset, we note that the typical residual of the best-fit Serkowski curve to the LIPS data is  $\lesssim 0.05\%$ . The result of this test is shown in the right panel of Fig. 12. Although the red straight line in the right panel of Fig. 12 slightly deviates from the original distribution of black dots, the results of our second test suggest that if the polarisation that we have measured with FORS2 followed the linear relationship by Whittet et al. (1992), then we would still have been able to recover a similar (although not identical) linear relationship. Therefore the results of this final experiment seem to contradict the idea that the discrepancies between our results and those found by Whittet et al. (1992) are due to the limited wavelength range of the spectropolarimetric observations compared to the sample by Whittet et al. (1992).

In conclusion, if the results by Whittet et al. (1992) are correct, it means that the shape of our polarisation spectra is affected by errors that are substantially larger than photon noise, probably  $\lesssim 0.1\%$  in the BBLP filters, and we suggest that in order to retrieve meaningful  $K$  values of the Serkowski-curve parameters, it is desirable to obtain a stronger constraint in the blue and red spectral regions than is possible with FORS optical spectropolarimetry. However, the observed discrepancies between our sample and that of Whittet et al. (1992) may also be due to the fact that different surveys probe regions of the ISM with different dust grain features (e.g. Voshchinnikov 2012). The differences between the surveys are also evident in the  $P_{\max}$  histogram of Fig. 13.

### 6.3. Relationships between $\lambda_{\max}$ , $P_{\max}$ and the extinction

The  $\lambda_{\max}$  and  $P_{\max}$  parameters retrieved from the best fit seem accurate enough to allow us a meaningful discussion of their relationships with other features of the ISM, like for instance the visual extinction.

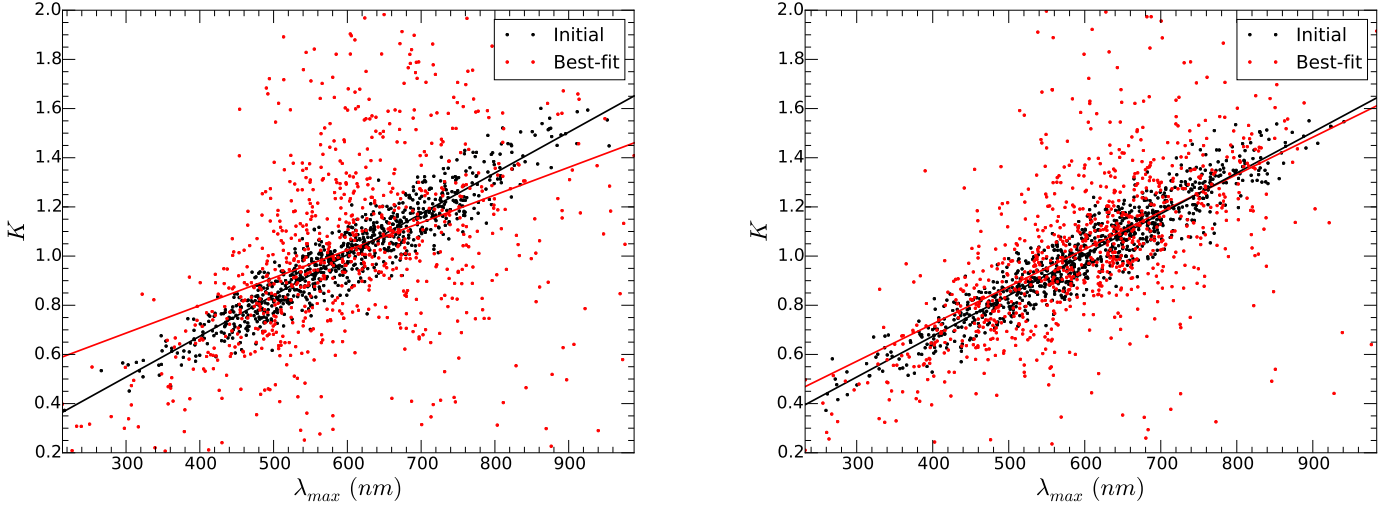


**Fig. 12.** Simulation of the recovery of the free parameters of the Serkowski curve from a numerical dataset simulating noisy data. *Left panel:* using a 100 nm step size. *Right panel:* using a 20 nm step size. The figure is explained in the text.

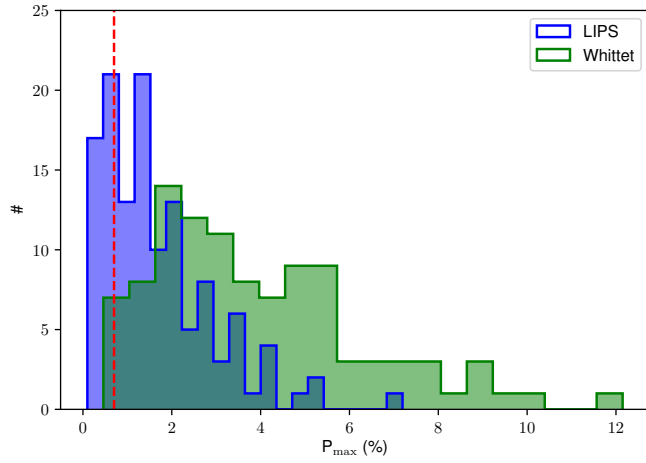


**Fig. 13.** Distribution of  $P_{\max}$  for our sample and for that of Whittet et al. (1992). The red dashed line at 0.70% shows the  $P_{\max}$  limit below which we did not calculate the best-fit parameters of the Serkowski curve.

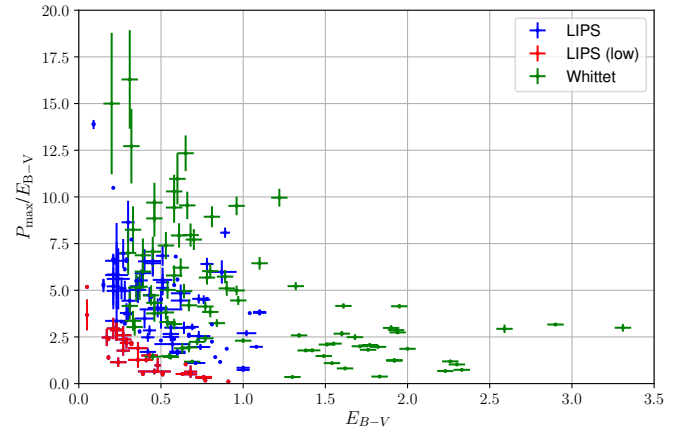


**Fig. 15.** Relationship between maximum polarisation and  $E(B - V)$ . “LIPS (low)” refer to stars for which  $P \leq 0.7\%$ .

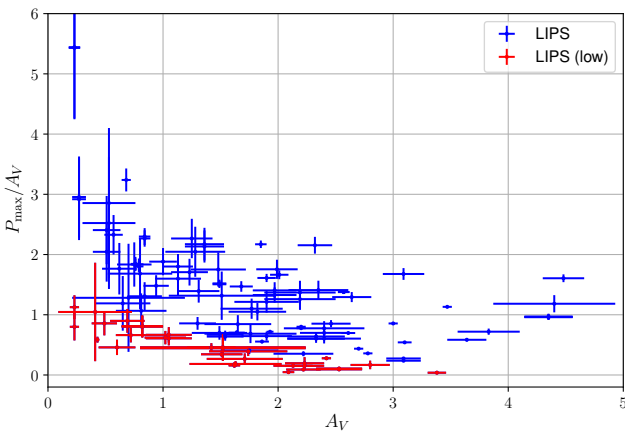


**Fig. 14.** Relationship between polarisation efficiency and visual extinction. The red symbols (“LIPS low”) refer to data with  $P \leq 0.7\%$ .

### 6.3.1. Polarising efficiency $P_{\max}/A_V$ vs. visual extinction $A_V$

Figure 14 shows the parameter  $P_{\max}/A_V$ , the historically defined polarising efficiency (Tamura et al. 1987; Whittet et al. 1994; Greenberg et al. 1995), plotted versus the total visual extinction  $A_V$ . The polarisation efficiency decreases as visual extinction increases, in agreement with what was found by Whittet et al. (1994) (see their Fig. 7), by Gerakines et al. (1995), who proposed the relationship  $p_{\max}/A_V = 1.38 A_V^{-0.56}$  (see their Fig. 1), and Whittet et al. (2001), who proposed the relationship  $p_{\max}/A_V = 2.5 A_V^{-0.71}$  (see their Fig. 10).

### 6.3.2. Polarising efficiency $P_{\max}/E(B - V)$ vs. selective extinction $E(B - V)$

Another quantity representing the polarising efficiency is the ratio  $P_{\max}/E(B - V)$ , where  $E(B - V) = A_B - A_V$  is the selective extinction. Serkowski et al. (1975) found that this parameter is always  $\lesssim 9\% \text{ mag}^{-1}$ . The relationship between  $P_{\max}/E(B - V)$  and  $E(B - V)$  depends on the dust grain size and has been dis-

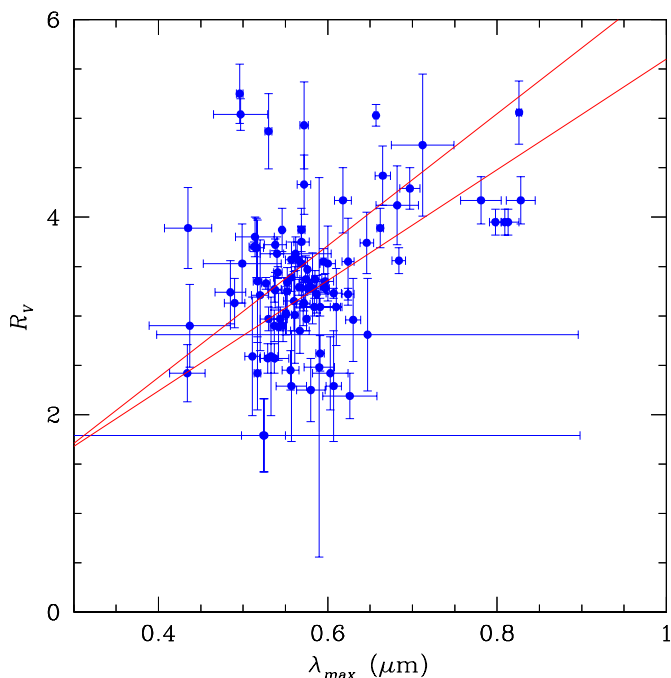


**Fig. 16.** The relationship between  $R_V$  and  $\lambda_{\max}$ . Symbols refer to the data from our survey, and the solid lines are the relationships of Eqs. (24) and (25).

cussed by Voshchinnikov et al. (2016). Figure 15 shows this relationship for our dataset.

### 6.3.3. Total-to-selective extinction ratio $R_V$ vs. $\lambda_{\max}$

Whittet & van Breda (1978) derived the linear relationship

$$R_V = (5.6 \pm 0.3) \lambda_{\max}, \quad (24)$$

where  $R_V = A_V/E(B-V)$  is the ratio between total and selective extinction, and  $\lambda_{\max}$  is expressed in  $\mu\text{m}$ , while Clayton & Mathis (1988) suggested

$$R_V = -0.29 \pm 0.74 + (6.67 \pm 1.17) \lambda_{\max}. \quad (25)$$

The validity of this relationship was not confirmed in later studies (e.g. Whittet et al. 2001), and our data do not follow any of these relationships either (see Fig. 16).

## 6.4. Comments on special cases

### 6.4.1. Position angle varying with wavelength

If polarisation is due to dichroic extinction from interstellar dust, we would expect a fairly smooth function  $P(\lambda)$  that is reasonably well reproduced by the Serkowski curve, with the position angle independent of  $\lambda$ .

Of special interest are stars for which the position angle of the polarisation is not constant with wavelength. These cases may be identified from inspection of the last column of Table 2, which provides the wavelength gradients of the polarisation position angle. This may be due to the presence of more than one dust cloud along the line of sight, with different characteristics, but we should note that the steepest gradients are usually associated with stars with low polarisation (e.g. the blue supergiant HD 154368 and the main-sequence O star HD 93222). Particularly puzzling is the case of the Be stars HD 155851 and

HD 172694, which show a sharp change in slope in both the polarisation and the position angle at wavelengths longer than 820 nm. The observed polarisation is probably given by the superposition of the contribution from the circumstellar disc and the ISM dust, and the change in polarisation, which corresponds to the Paschen edge, almost certainly originates in the disc. The polarimetric properties (including variability) of Be stars have been studied in the past (e.g. Bjorkman 1994), but to our best knowledge, the observed sharp change in polarisation at longer wavelength has not previously been reported.

### 6.4.2. Time variability

Twenty-two stars of our sample were observed twice and one was observed three times. These stars can be checked for variability.

From our observations, it appears that the high-mass X-binary HD 153919 shows variability in the fraction of linear polarisation, consistent with the observations by van Paradijs (1980), Oestreicher & Schulte-Ladbeck (1982), and Dolan & Tapia (1984), who found the star to be periodically variable with an amplitude of  $\sim 0.3\%$ .

The blue supergiant HD 149404 (observed twice by us) shows variability both in  $P$  and  $\theta^E$  (the  $\theta^E$  variability was already detected in a previous work, see the discussion in Sect. 3.2).

Star HD 116852 shows a discrepancy of 0.2% between the polarisation measured in two different observing epochs, which may also be due to intrinsic variability.

## 7. Conclusions

Using the FORS2 instrument of the ESO VLT, we have obtained moderate-resolution ( $R \sim 880$ ) polarisation spectra with high  $S/N$  for 101 diffuse interstellar lines of sight, and made them publicly available – at different rebinning steps – at CDS. We used the polarisation spectra to estimate broadband linear polarisation values in the  $BVRI$  filters and for an analysis with the Serkowski curve. In particular, we fitted the polarisation spectra of all stars with  $P_{\max} \geq 0.7\%$  (76 targets) with the Serkowski curve, and, in addition, we fitted the wavelength-dependent position angle with a first-order polynomial, estimating for each star the newly introduced parameter  $d\theta/d\lambda$  (measured in  $^\circ/100\text{ nm}$ ). As expected, we often found this parameter to be consistent with zero, but with exceptions, especially for stars with low polarisation. Remarkable exceptions are represented by the Be stars HD 155851 and HD 172694, which exhibit a sharp change in slope in the polarisation and its position angle at wavelengths  $\geq 820\text{ nm}$ , in proximity of the Paschen edge.

Uncertainties due to photon noise are very small (typically  $\leq 0.1\%$  per nm, reduced to a few units in  $10^{-4}$  when integrating in a broadband filter). However, while processing the data, we discovered some small discrepancies larger than photon noise between datasets obtained within a very short interval of time. We have ascribed these discrepancies to an imperfectly accurate setting of the retarder waveplate. This issue was mitigated by combining data obtained with and without order-separating filter. Spectra are also affected by cosmic rays, and, corresponding to sharp features in intensity (such as emission lines or the  $\text{O}_2\text{-A}$  band), exhibit polarisation spikes that we believe to be spurious (at least most of them). In spite of these caveats, our Large Interstellar Polarisation Survey (LIPS) of the Southern Hemisphere significantly extends the current dataset of moderate-resolution spectropolarimetry of the diffuse ISM, particularly for sightlines

with relatively low interstellar reddening. Owing to systematic errors, we estimate that the accuracy of our BBLP measurements is of the order of 0.1 %.

In previous works, it was found that the parameters of the Serkowski curve are not independent of each other; for example, Whittet et al. (1992) found a linear relationship between the wavelength  $\lambda_{\max}$  at which the polarisation reaches maximum and the width  $K$  of the polarisation spectrum. Our results deviate significantly from the trends found by Whittet et al. (1992). We have investigated this issue by means of numerical simulations, without reaching a clear conclusion. On the one hand, the  $K$  parameter of the Serkowski curve (which is related to the width of the polarisation spectrum) may not be sufficiently well constrained by our observations. However, the observed deviations may also be attributed to real physical differences – either in dust grains or interstellar conditions – between the different regions probed with LIPS and the sample by Whittet et al. (1992).

We have also performed a preliminary investigation of the relationship between polarisation and interstellar extinction, improving a previously found relationship between polarisation efficiency and visual (or selective) extinction. In agreement with previous works, we were unable to confirm the existence of a linear relationship between the ratio of total-to-selective extinction and the wavelength at which the polarisation reached maximum.

Moderate-resolution spectropolarimetry adds new information that can help us to better understand the properties of dust and/or ISM conditions. Our Southern Hemisphere FORS2 data will be combined with the Northern Hemisphere ISIS data, which will be described in a separate publication. This combined LIPS dataset will then enable a number of detailed studies of polarisation properties and modelling of dust grains.

*Acknowledgements.* This work is based on observations collected at the European Organisation for Astronomical Research in the Southern Hemisphere under ESO programmes 095.C-0855 and 096.C-0159, PI=N.L.J. Cox. Some of the data presented in this paper were obtained from the Mikulski Archive for Space Telescopes (MAST). STScI is operated by the Association of Universities for Research in Astronomy, Inc., under NASA contract NAS5-26555. Support for MAST for non-HST data is provided by the NASA Office of Space Science via grant NNX09AF08G and by other grants and contracts. NVV acknowledges the support from RFBR grant 16-02-00194 and RFBR-DST grant 16-52-45005.

## References

Anderson, C. M., Weitenbeck, A. J., Code, A. D., et al. 1996, *AJ*, 112, 2726  
 Appenzeller, I. 1967, *PASP*, 79, 136  
 Appenzeller, I., Fricke, K., Fürtig, W., et al. 1998, *The Messenger*, 94, 1  
 Appenzeller, I. & Rupprecht, G. 1992, *The Messenger*, 67, 18  
 Bagnulo, S., Fossati, L., Kochukhov, O., & Landstreet, J. D. 2013, *A&A*, 559, A103  
 Bagnulo, S., Landolfi, M., Landstreet, J. D., et al. 2009, *PASP*, 121, 993  
 Bagnulo, S., Landstreet, J. D., Fossati, L., & Kochukhov, O. 2012, *A&A*, 538, A129  
 Bjorkman, K. S. 1994, *Ap&SS*, 221, 335  
 Cami, J. & Cox, N. L. J., eds. 2014, *IAU Symposium*, Vol. 297, *The Diffuse Interstellar Bands*  
 Carrasco, L., Strom, S. E., & Strom, K. M. 1973, *ApJ*, 182, 95  
 Cartledge, S. I. B., Clayton, G. C., Gordon, K. D., et al. 2005, *ApJ*, 630, 355  
 Cikota, A., Patat, F., Cikota, S., & Faran, T. 2017, *MNRAS*, 464, 4146  
 Clarke, D. & Al-Roubaie, A. 1983, *MNRAS*, 202, 173  
 Clarke, D. & Stewart, B. G. 1986, *Vistas in Astronomy*, 29, 27  
 Clayton, G. C. & Mathis, J. S. 1988, *ApJ*, 327, 911  
 Cox, N., Cami, J., Farhang, A., et al. 2017, *ArXiv e-prints* [1708.01429]  
 Cox, N. L. J., Cordiner, M. A., Cami, J., et al. 2006, *A&A*, 447, 991  
 Dolan, J. F. & Tapia, S. 1984, *A&A*, 139, 249  
 Dombrowskii, V. 1949, On the polarization of radiation of early-type stars, *Dokl Akad Nauk Armenia*, 10, 199  
 Dyck, H. M. & Jones, T. J. 1978, *AJ*, 83, 594  
 Efimov, Y. S. 2009, *Bulletin Crimean Astrophysical Observatory*, 105, 82

Fossati, L., Bagnulo, S., Mason, E., & Landi Degl'Innocenti, E. 2007, in *Astronomical Society of the Pacific Conference Series*, Vol. 364, *The Future of Photometric, Spectrophotometric and Polarimetric Standardization*, ed. C. Sterken, 503  
 Gaia Collaboration, Prusti, T., de Bruijne, J. H. J., et al. 2016, *A&A*, 595, A1  
 Gerakines, P. A., Whittet, D. C. B., & Lazarian, A. 1995, *ApJ*, 455, L171  
 Gordon, K. D., Clayton, G. C., Misselt, K. A., Landolt, A. U., & Wolff, M. J. 2003, *ApJ*, 594, 279  
 Greenberg, J. M., Li, A., Mendoza-Gomez, C. X., et al. 1995, *ApJ*, 455, L177  
 Hall, J. S. 1949, *Science*, 109, 166  
 Heiles, C. 2000, *AJ*, 119, 923  
 Hiltner, W. A. 1949, *Science*, 109, 165  
 Landi Degl'Innocenti, E., Bagnulo, S., & Fossati, L. 2007, in *Astronomical Society of the Pacific Conference Series*, Vol. 364, *The Future of Photometric, Spectrophotometric and Polarimetric Standardization*, ed. C. Sterken, 495  
 Larson, K. A. 1999, PhD thesis, Rensselaer Polytechnic Institute  
 Leroy, J. L. 1993, *A&A*, 274, 203  
 Leroy, J. L. 1999, *A&A*, 346, 955  
 Luna, H. G. 1988, *A&AS*, 74, 427  
 Martin, P. G., Adamson, A. J., Whittet, D. C. B., et al. 1992, *ApJ*, 392, 691  
 Massey, P. & Conti, P. S. 1979, in *IAU Symposium*, Vol. 83, *Mass Loss and Evolution of O-Type Stars*, ed. P. S. Conti & C. W. H. De Loore, 271–273  
 Meade, M. R., Whitney, B. A., Babler, B. L., et al. 2012, in *American Institute of Physics Conference Series*, Vol. 1429, *American Institute of Physics Conference Series*, ed. J. L. Hoffman, J. Bjorkman, & B. Whitney, 226–229  
 Oestreicher, R. & Schulte-Ladbeck, R. 1982, *A&A*, 114, 328  
 Patat, F., Maund, J. R., Benetti, S., et al. 2010, *A&A*, 510, A108  
 Patat, F. & Taubenberger, S. 2011, *A&A*, 529, A57  
 Patriarchi, P., Morbidelli, L., & Perinotto, M. 2003, *A&A*, 410, 905  
 Santos, F. P., Corradi, W., & Reis, W. 2011, *ApJ*, 728, 104  
 Sarre, P. J. 2006, *Journal of Molecular Spectroscopy*, 238, 1  
 Scarrott, S. M., Warren-Smith, R. F., Pallister, W. S., Axon, D. J., & Bingham, R. G. 1983, *MNRAS*, 204, 1163  
 Serkowski, K. 1973, in *IAU Symposium*, Vol. 52, *Interstellar Dust and Related Topics*, ed. J. M. Greenberg & H. C. van de Hulst, 145  
 Serkowski, K., Mathewson, D. S., & Ford, V. L. 1975, *ApJ*, 196, 261  
 Shurcliff, W. A. 1962, *Polarized light*  
 Siebenmorgen, R., Voshchinnikov, N. V., & Bagnulo, S. 2014, *A&A*, 561, A82  
 Tamura, M., Nagata, T., Sato, S., & Tanaka, M. 1987, *MNRAS*, 224, 413  
 Valencic, L. A., Clayton, G. C., & Gordon, K. D. 2004, *ApJ*, 616, 912  
 van Paradijs, J. 1980, *A&A*, 87, 210  
 Voshchinnikov, N. V. 2012, *J. Quant. Spec. Radiat. Transf.*, 113, 2334  
 Voshchinnikov, N. V., Il'in, V. B., & Das, H. K. 2016, *MNRAS*, 462, 2343  
 Wardle, J. F. C. & Kronberg, P. P. 1974, *ApJ*, 194, 249  
 Wegner, W. 2003, *Astronomische Nachrichten*, 324, 219  
 Weitenbeck, A. J. 1999, *Acta Astron.*, 49, 59  
 Whittet, D. C. B., Gerakines, P. A., Carkner, A. L., et al. 1994, *MNRAS*, 268, 1  
 Whittet, D. C. B., Martin, P. G., Hough, J. H., et al. 1992, *ApJ*, 386, 562  
 Whittet, D. C. B., Pendleton, Y. J., Gibb, E. L., et al. 2001, *ApJ*, 550, 793  
 Whittet, D. C. B. & van Breda, I. G. 1978, *A&A*, 66, 57  
 Wilking, B. A., Lebofsky, M. J., Kemp, J. C., Martin, P. G., & Rieke, G. H. 1980, *ApJ*, 235, 905  
 Wilking, B. A., Lebofsky, M. J., & Rieke, G. H. 1982, *AJ*, 87, 695  
 Wolstencroft, R. D. & Nandy, K. 1971, *Ap&SS*, 12, 158  
 Wolstencroft, R. D. & Smith, R. J. 1984, *MNRAS*, 208, 461



Table 1. continued.

Star	RA	DEC	V	Spectral type	E(B-V)	R <sub>V</sub>	A <sub>V</sub>	REF	DATE	UT	Exp (sec)
HD 133518	15:06:56.0	-52:01:47.2	6.39	B2 Vp	0.15	1.79 ± 0.37	0.27 ± 0.06	W	2016-02-22	04:46	8
									2015-05-11	09:06	4
									2016-02-12	07:10	8
HD 134591	15:11:51.0	-34:45:47.4	8.37	B5III	0.24 ± 0.05	2.51 ± 0.40	0.60 ± 0.16	V	2015-05-12	02:47	40
									2016-02-22	05:18	32
HD 135591	15:18:49.1	-60:29:46.8	5.46	O8IV((f))	0.22	3.57 ± 0.18	0.79 ± 0.04	W	2015-05-12	04:46	3
									2016-01-29	08:42	6
HD 147683	16:24:43.7	-34:53:37.5	7.05	B3: Vn	0.28			X	2016-02-12	08:08	8
HD 147888	16:25:24.3	-23:27:36.8	6.74	B3 V:	0.51 ± 0.04	3.89 ± 0.20	1.99 ± 0.18	V	2016-01-30	08:40	24
HD 147889	16:25:24.3	-24:27:56.6	7.90	B2 V	1.10 ± 0.04	3.95 ± 0.13	4.35 ± 0.21	V	2015-05-13	09:53	32
									2015-05-24	03:21	32
									2016-01-28	08:58	24
HD 148379	16:29:42.3	-46:14:35.6	5.37	B2Iab	0.73 ± 0.07	3.28 ± 0.36	2.40 ± 0.35	V	2015-05-11	09:26	2
HD 148688	16:31:41.8	-41:49:01.7	5.39	B1Iaeqp	0.58	3.33 ± 0.06	1.93 ± 0.03	W	2015-05-11	09:42	2
HD 148937	16:33:52.4	-48:06:40.5	6.71	O6f?p	0.67	3.28 ± 0.06	2.20 ± 0.04	W	2015-05-12	05:20	8
									2016-02-12	07:52	16
HD 149404	16:36:22.6	-42:51:31.9	5.47	O8.5Iab(f)p	0.62 ± 0.06	3.53 ± 0.38	2.19 ± 0.31	V	2015-05-12	05:38	3
									2016-01-30	08:57	6
HD 150136	16:41:20.4	-48:45:46.7	5.65	O3.5-4 III(f*)+O	0.50	3.27 ± 0.13	1.64 ± 0.07	W	2015-05-20	05:00	3
HD 151804	16:51:33.7	-41:13:49.9	5.22	O8Iaf	0.30 ± 0.03	4.33 ± 0.30	1.30 ± 0.16	V	2015-05-24	03:39	3
HD 151805	16:51:35.7	-41:46:35.5	9.01	B1Ib	0.43 ± 0.05	3.29 ± 0.30	1.42 ± 0.21	V	2016-02-22	08:24	48
HD 152235	16:53:58.9	-41:59:39.6	6.38	B0.5Ia	0.71 ± 0.06	3.13 ± 0.25	2.22 ± 0.26	V	2015-05-24	03:58	4
HD 152248	16:54:10.1	-41:49:30.1	6.05	O7Iabf+O7Ib(f)	0.41 ± 0.04	3.68 ± 0.26	1.51 ± 0.18	V	2015-05-24	04:15	4
HD 152249	16:54:11.6	-41:50:57.2	6.45	OC9Iab	0.46 ± 0.10	3.54 ± 0.45	1.63 ± 0.40	V	2015-05-24	04:31	8
HD 152408	16:54:58.5	-41:09:03.1	5.77	O8Iape	0.42 ± 0.05	4.17 ± 0.33	1.75 ± 0.25	V	2015-05-24	04:47	3
HD 152424	16:55:03.3	-42:05:27.0	6.27	OC9.2Ia	0.68 ± 0.04	3.28 ± 0.15	2.23 ± 0.17	V	2015-05-24	05:04	4
									2016-02-12	07:34	12
HD 153919	17:03:56.8	-37:50:38.9	6.51	O6Iafcp	0.51 ± 0.04	3.87 ± 0.22	1.97 ± 0.19	V	2015-04-12	08:58	8
									2016-02-22	07:26	16
HD 154043	17:05:18.9	-47:04:08.5	7.10	B2Iab	0.78	3.30 ± 0.06	2.57 ± 0.05	W	2015-04-12	08:39	12
									2016-02-02	09:08	8
HD 154368	17:06:28.4	-35:27:03.8	6.13	O9.2Iab	0.76 ± 0.05	3.33 ± 0.15	2.53 ± 0.20	V	2015-04-12	09:19	4
									2016-02-22	08:44	8
HD 155806	17:15:19.2	-33:32:54.3	5.53	O7.5V((f))z(e)	0.28	2.48 ± 1.92	0.70 ± 0.49	P	2015-05-24	05:36	3
HD 155851	17:15:33.8	-32:41:23.1	8.13	B0Vne	0.32	5.25 ± 0.30	1.68 ± 0.10	W	2015-05-24	05:19	32
HD 156201	17:17:45.5	-35:13:27.0	8.01	B0.5 Ia	0.86	3.23 ± 0.05	2.78 ± 0.04	W	2015-05-25	02:06	32
HD 157038	17:22:39.2	-37:48:16.7	6.44	B3Iap	0.81	3.70 ± 0.05	3.00 ± 0.04	W	2015-05-25	02:32	8
HD 157978	17:26:19.0	07:35:44.3	6.04	G0/K0 II:+A1	0.65	3.72 ± 0.06	2.42 ± 0.04	W	2016-03-14	09:27	8
HD 161056	17:43:47.0	-07:04:46.6	6.32	B1.5 V	0.59	3.13 ± 0.08	1.85 ± 0.05	W	2016-02-17	08:57	12
HD 163181	17:56:16.1	-32:28:30.0	6.61	O9.5Ia/ab	0.74 ± 0.06	3.24 ± 0.32	2.40 ± 0.32	V	2015-05-25	02:57	8
HD 164073	18:02:00.6	-48:48:37.7	8.03	B3III/IV	0.21 ± 0.04	2.96 ± 0.42	0.62 ± 0.15	V	2015-05-25	03:19	32
HD 164740	18:03:38.3	-24:22:35.0	9.10	O7: V + sec	0.89 ± 0.03	5.03 ± 0.11	4.48 ± 0.18	V	2015-04-07	07:29	160
HD 315023	18:04:20.6	-24:13:54.9	10.03	OB	0.40 ± 0.06	4.12 ± 0.40	1.65 ± 0.29	V	2015-04-07	08:11	160
HD 165319	18:05:58.8	-14:11:53.0	8.04	O9.7Ib C	0.83	3.25 ± 0.05	2.70 ± 0.04	W	2015-10-16	01:15	24
HD 167838	18:17:37.7	-15:25:50.6	6.73	B5 Ia	0.63 ± 0.04	3.39 ± 0.14	2.13 ± 0.17	V	2016-03-13	09:06	16
BD-13 4920	18:18:26.2	-13:50:05.2	10.06	B1V	0.73 ± 0.04	3.22 ± 0.19	2.35 ± 0.26	V	2015-04-07	08:30	160
HD 168076	18:18:36.4	-13:48:02.0	8.25	O4III(f)	0.76 ± 0.04	3.47 ± 0.12	2.64 ± 0.17	V	2015-05-30	09:49	32
HD 169454	18:25:15.2	-13:58:42.3	6.71	B1Ia	1.08 ± 0.04	3.37 ± 0.09	3.64 ± 0.17	V	2016-03-13	09:22	16
HD 170740	18:31:25.7	-10:47:45.0	5.72	B2 V	0.50 ± 0.13	3.01 ± 0.49	1.51 ± 0.46	V	2016-03-15	09:06	12
HD 170938	18:32:37.8	-15:42:05.9	7.99	B1 Ia	1.04	3.34 ± 0.04	3.47 ± 0.04	W	2015-11-08	00:08	16
HD 171957	18:38:04.5	-14:00:17.2	6.47	B9 IV	0.27			X	2015-11-08	00:41	12
HD 172694	18:42:16.6	-15:51:20.8	8.12	B1: Vne	0.37	5.04 ± 0.16	1.86 ± 0.06	W	2015-06-02	04:27	160
HD 203532	21:33:54.6	-82:40:59.1	6.38	B3 IV	0.28 ± 0.03	3.37 ± 0.24	0.94 ± 0.11	V	2015-06-02	06:22	8
HD 210121	22:08:11.9	-03:31:52.8	7.68	B7II	0.31 ± 0.05	2.42 ± 0.29	0.75 ± 0.15	V	2015-10-02	03:02	24

Key to references: V=Valencic et al. (2004); W=Wegner (2003); C=Cartledge et al. (2005); C06=Cox et al. (2006); P=Patriarchi et al. (2003); G=Gordon et al. (2003); X=No R(V) data.





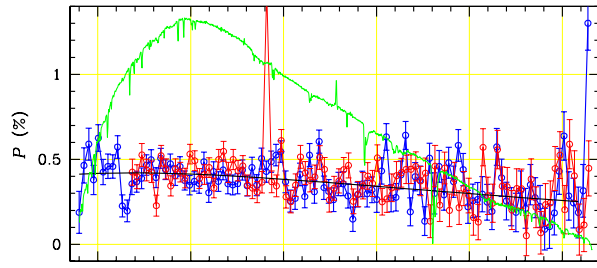


13. HD 155851 on 2015-05-24: at  $\lambda \geq 820$  nm the polarisation decreases, and the gradient of its position angle changes its sign.
14. HD 172694 on 2015-06-02 shows a sudden increase of polarisation at  $\lambda \geq 820$  nm. In the same wavelength region, the gradient of the polarisation position angle changes its sign, however the intensity spectrum does not show anything remarkable in that interval.

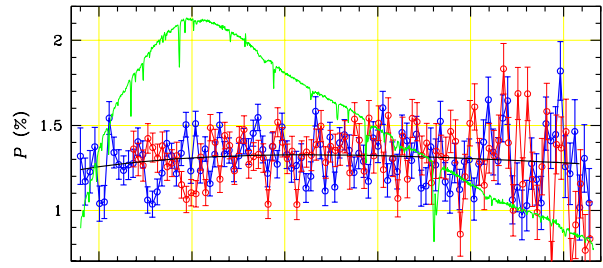
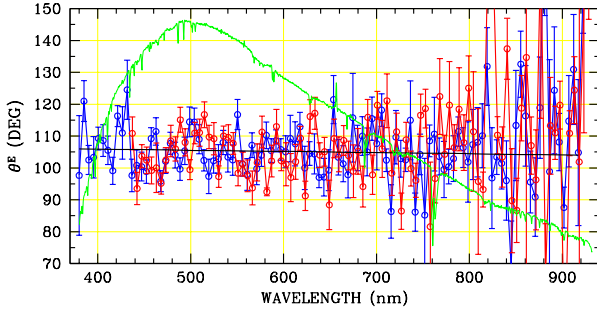
**Table 3.** Previously published Serkowski parameters for sightlines in common with LIPS.

STAR	Reference	Instrument	Best-fit parameters		
			$K$	$\lambda_{\max}$ (nm)	$P_{\max}$ (%)
HD 37903	(This work)	HPOL	$0.73 \pm 0.11$	$657 \pm 10$	$1.95 \pm 0.01$
	Efimov (2009)		1.35	680	2.00
	This work	FORS2	$1.51 \pm 0.23$	$646 \pm 8$	$1.82 \pm 0.01$
HD 38087	(This work)	HPOL	$1.25 \pm 0.21$	$585 \pm 12$	$2.79 \pm 0.02$
	This work	FORS2	$1.18 \pm 0.04$	$572 \pm 5$	$2.59 \pm 0.01$
HD 43384	Wilking et al. (1980)	FORS2	$0.97 \pm 0.04$	$560 \pm 10$	$3.00 \pm 0.04$
	This work	FORS2	$0.92 \pm 0.03$	$566 \pm 2$	$3.06 \pm 0.01$
Walker 67	Wilking et al. (1980)		$1.39 \pm 0.09$	$810 \pm 2$	$5.31 \pm 0.06$
	This work	FORS2	$1.40 \pm 0.05$	$826 \pm 3$	$5.20 \pm 0.04$
HD 108639	Heiles (2000)		$0.87 \pm 0.13$	$520 \pm 10$	$1.91 \pm 0.02$
	This work	FORS2	$1.29 \pm 0.23$	$550 \pm 5$	$1.92 \pm 0.04$
HD 147888	Wilking et al. (1982)		$1.29 \pm 0.05$	$720 \pm 10$	$3.75 \pm 0.07$
	Martin et al. (1992)		$1.28 \pm 0.04$	$700 \pm 10$	$3.63 \pm 0.04$
	(This work)	HPOL	$1.51 \pm 0.04$	$672 \pm 20$	$3.53 \pm 0.01$
	This work	FORS2	$1.43 \pm 0.02$	$662 \pm 4$	$3.49 \pm 0.01$
HD 147889	Wilking et al. (1980)		$1.32 \pm 0.05$	$800 \pm 10$	$4.09 \pm 0.07$
	Martin et al. (1992)		$1.25 \pm 0.03$	$780 \pm 10$	$4.02 \pm 0.04$
	This work	FORS2 (2015-05-13)	$1.32 \pm 0.02$	$809 \pm 4$	$4.22 \pm 0.01$
	This work	FORS2 (2015-05-25)	$1.37 \pm 0.04$	$798 \pm 7$	$4.18 \pm 0.01$
	This work	FORS2 (2016-01-28)	$1.18 \pm 0.09$	$815 \pm 13$	$4.18 \pm 0.01$
HD 161056	Wilking et al. (1980)		$0.96 \pm 0.09$	$560 \pm 2$	$3.8 \pm 0.1$
	(This work)	HPOL	$1.3 \pm 0.02$	$578 \pm 1$	$4.08 \pm 0.01$
	This work	FORS2	$1.43 \pm 0.05$	$572 \pm 2$	$4.02 \pm 0.04$
HD 164740	Wilking et al. (1982)		$1.24 \pm 0.12$	$670 \pm 20$	$7.75 \pm 0.15$
	Martin et al. (1992)		$1.24 \pm 0.07$	$670 \pm 10$	$7.45 \pm 0.14$
	This work	FORS2	$1.72 \pm 0.02$	$657 \pm 2$	$7.20 \pm 0.02$
HD 210121	Larson (1999)		$0.66 \pm 0.09$	$380 \pm 30$	$1.32 \pm 0.04$
	(This work)	HPOL	$0.65 \pm 0.15$	$402 \pm 50$	$1.37 \pm 0.06$
	This work	FORS2	$0.55 \pm 0.12$	$434 \pm 21$	$1.38 \pm 0.02$
HD 251204	(This work)	HPOL	$1.25 \pm 0.11$	$584 \pm 7$	$4.95 \pm 0.03$
	This work	FORS2	$1.00 \pm 0.02$	$575 \pm 2$	$5.00 \pm 0.01$

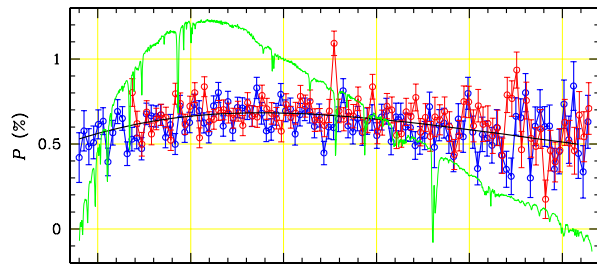
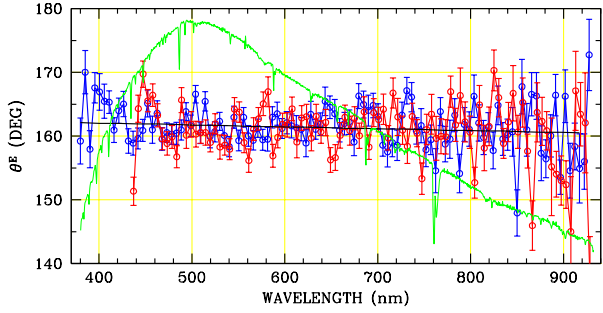
**Notes.** Wilking et al. (1980) and Martin et al. (1992) report updated Serkowski parameters from compilations of broad-band polarimetric data. The best-fit parameters from HPOL were obtained in this work using data made available at the Mikulski Archive for Space Telescopes (MAST).



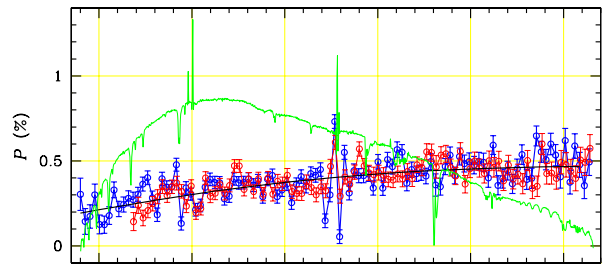
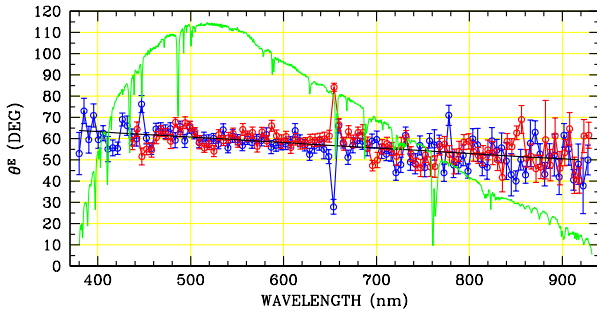
AzV18 2015-10-14



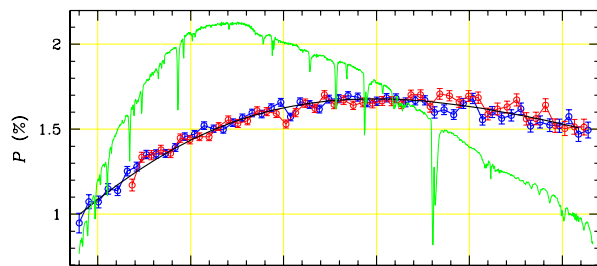
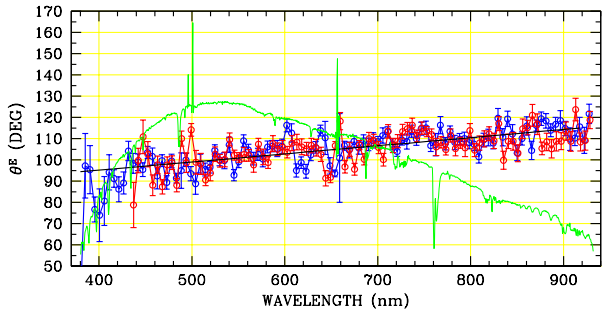
AzV456 2015-10-14



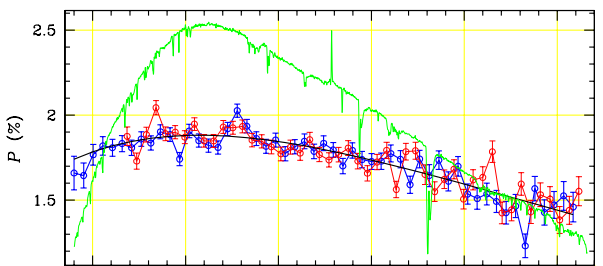
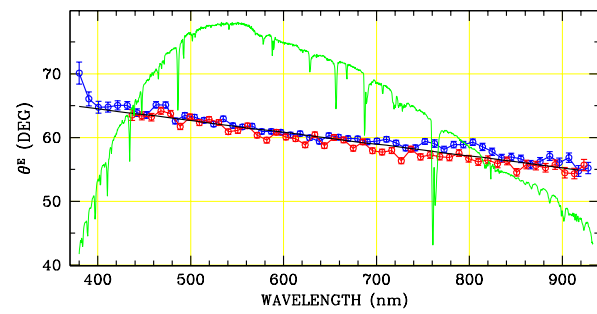
HD36982 2015-10-17



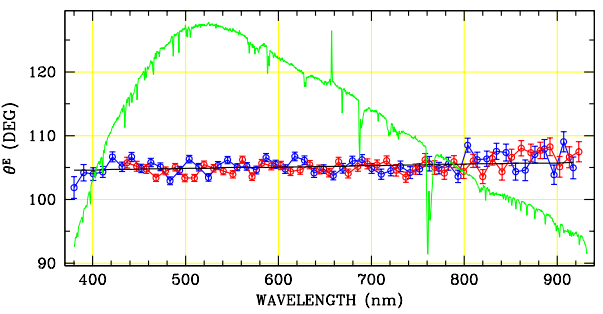
HD37021 2015-10-17

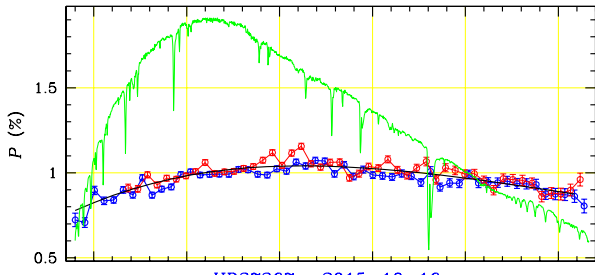


HD37061 2015-10-14

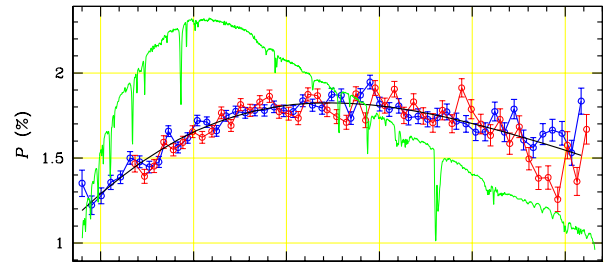
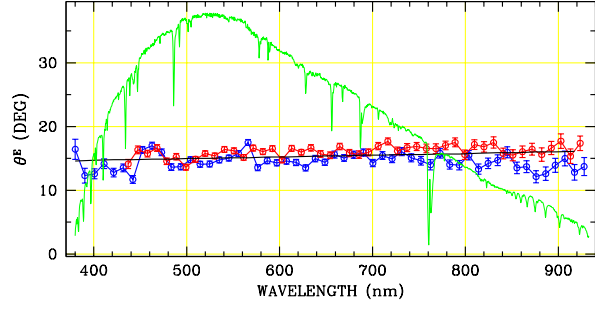


HD38029 2015-10-14

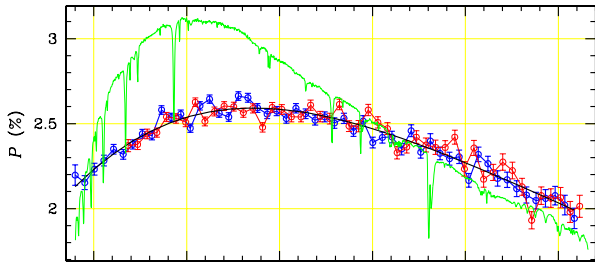
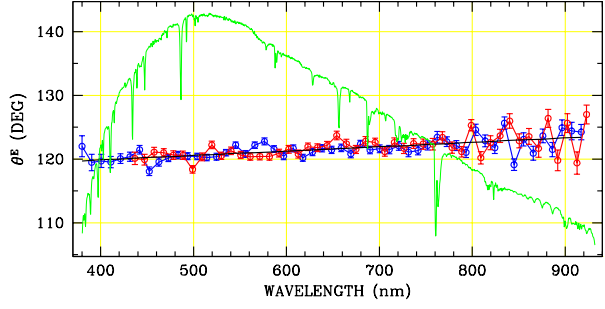




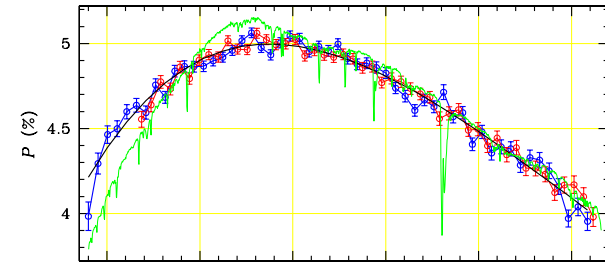
HD37367 2015-10-16



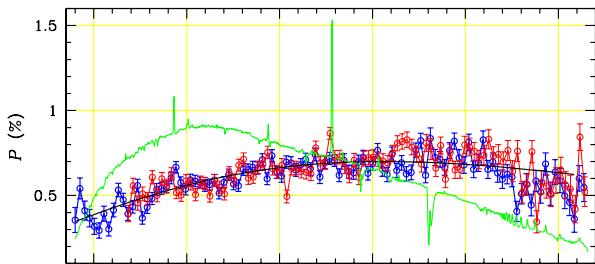
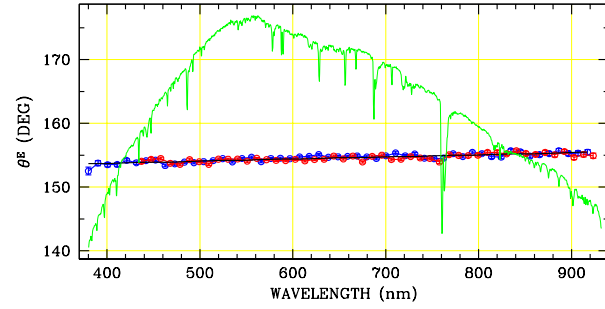
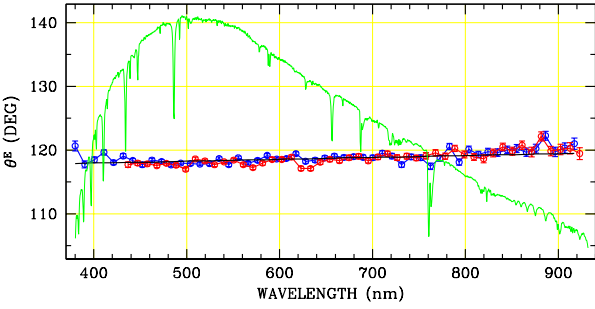
HD37903 2015-10-17



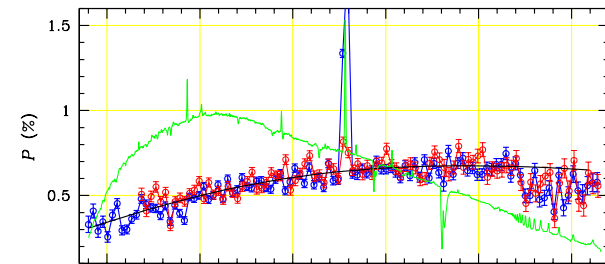
HD38087 2015-10-17



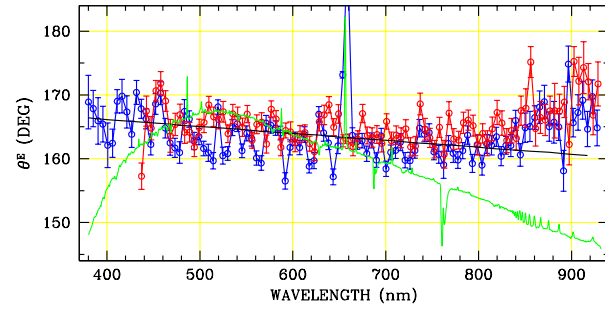
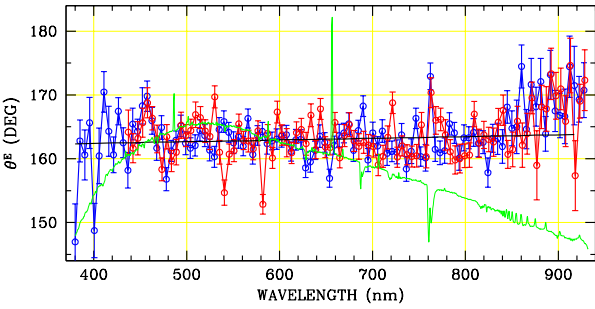
HD251204 2015-10-14

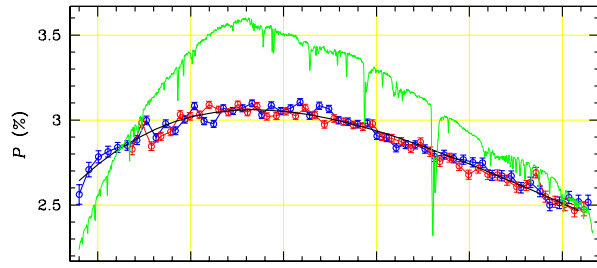


HD39680 2015-10-14

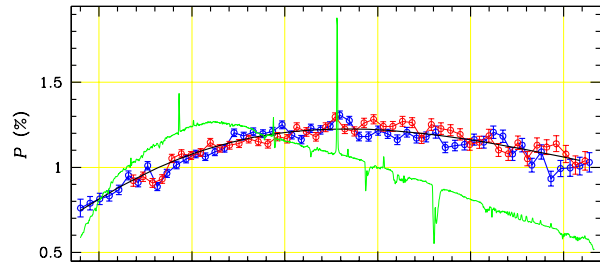
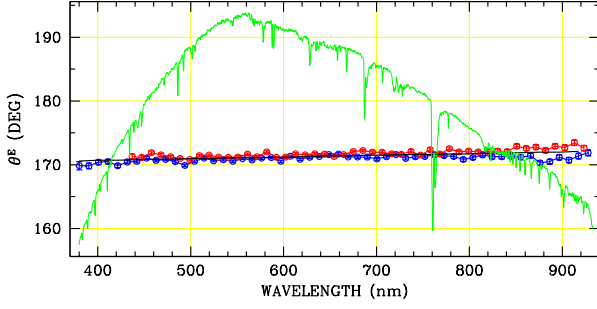


HD39680 2015-12-01

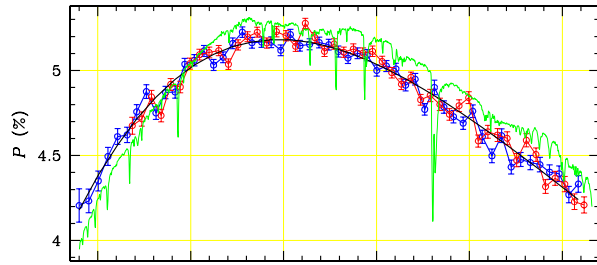
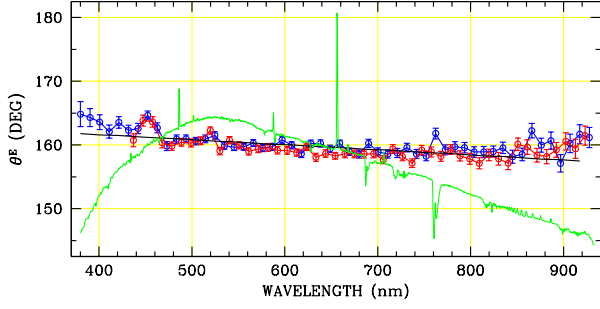




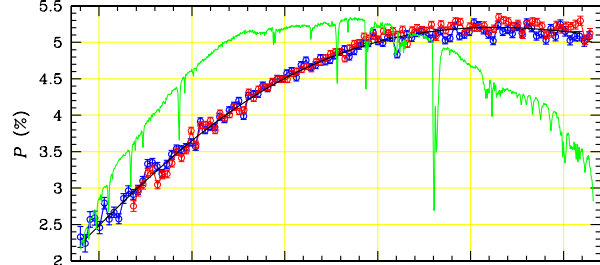
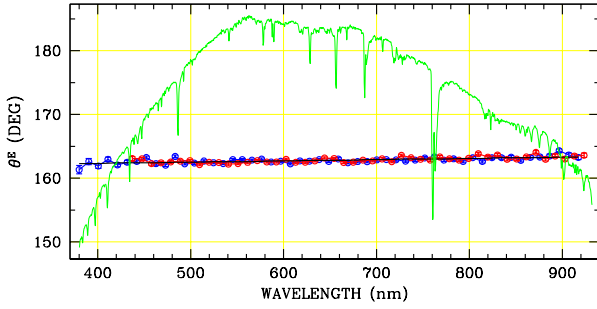
HD43384 2015-04-07



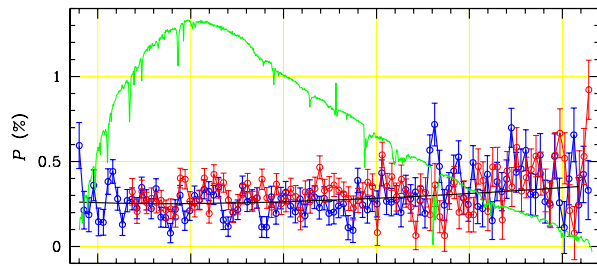
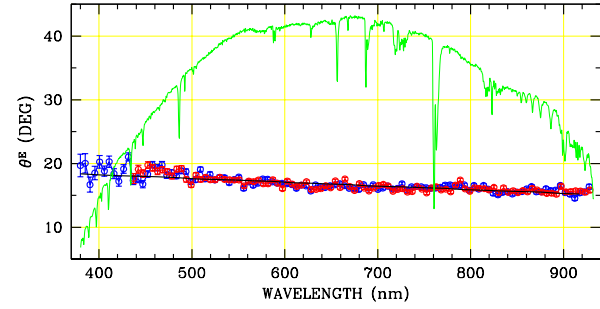
HD45314 2015-10-17



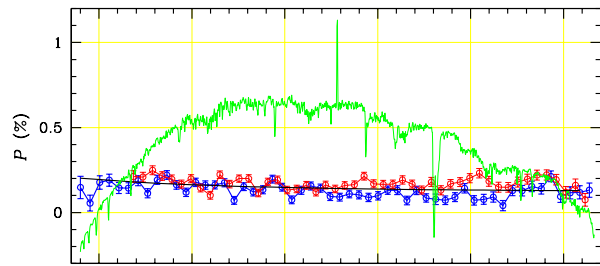
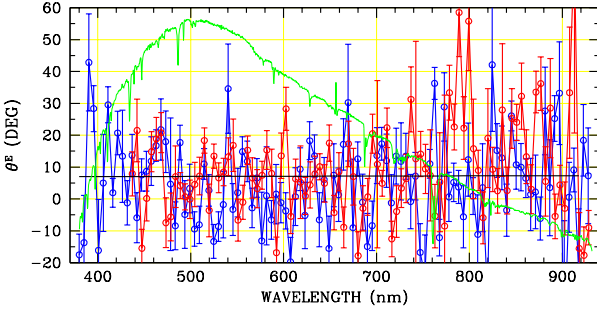
HD252325 2015-10-14



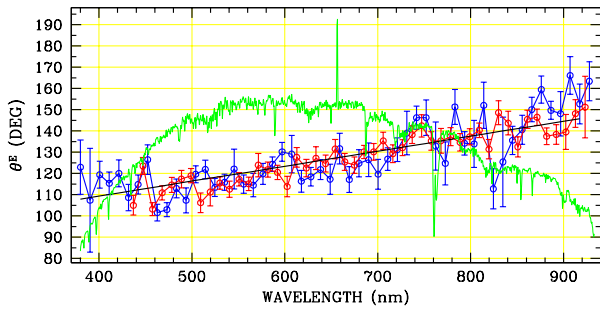
Walker67 2015-10-17

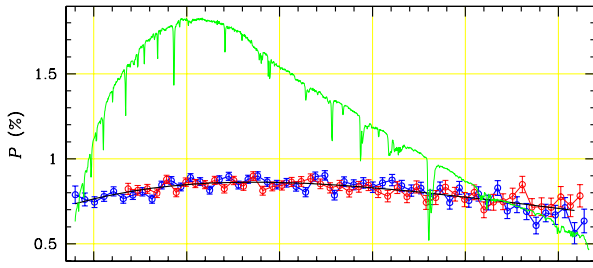


HD49787 2015-10-17

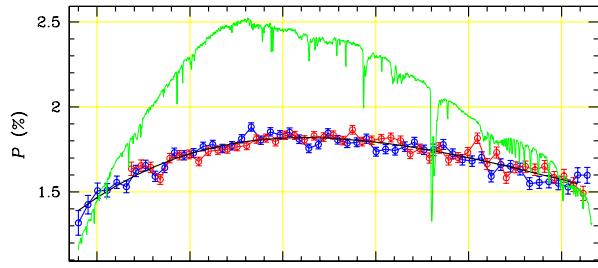
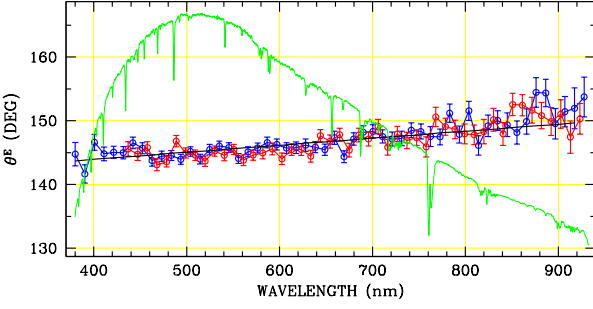


HD50820 2015-10-17

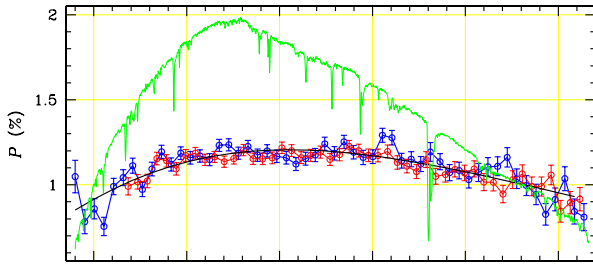
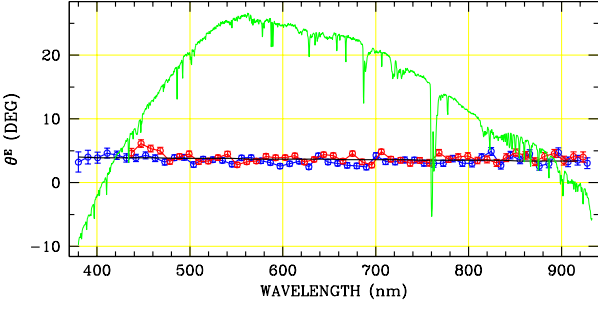




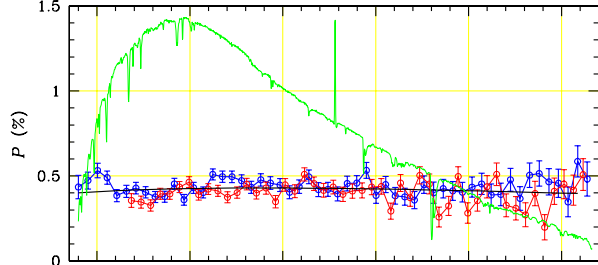
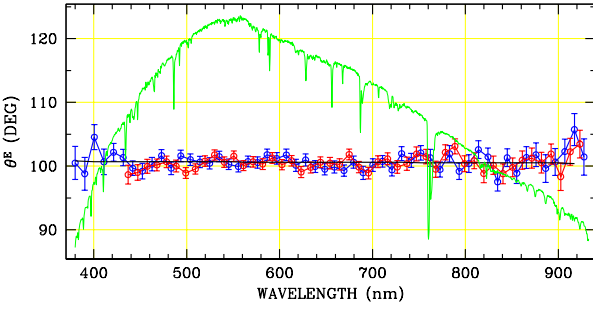
HD54662 2015-10-17



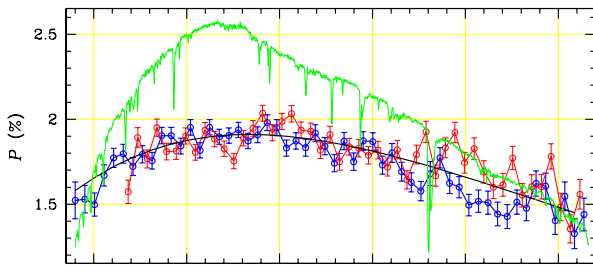
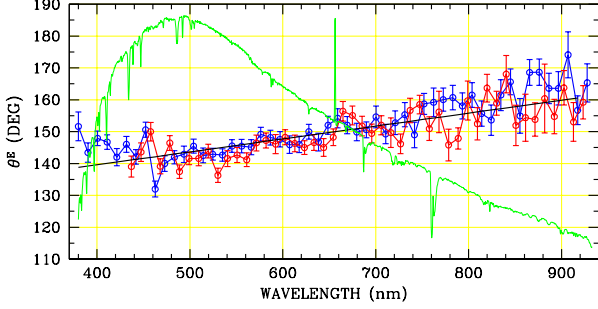
HD61827 2015-05-22



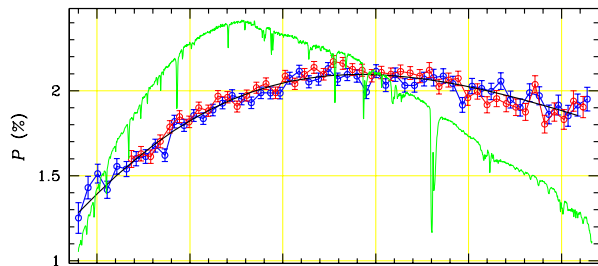
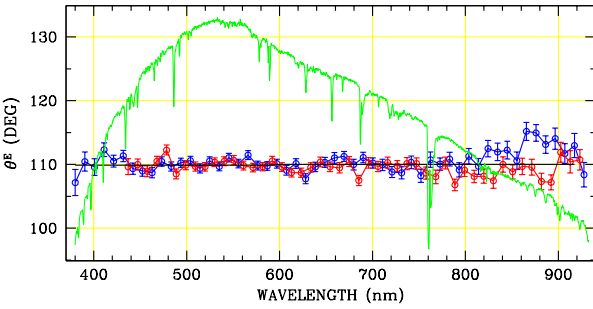
CD-28 5205 2015-05-12



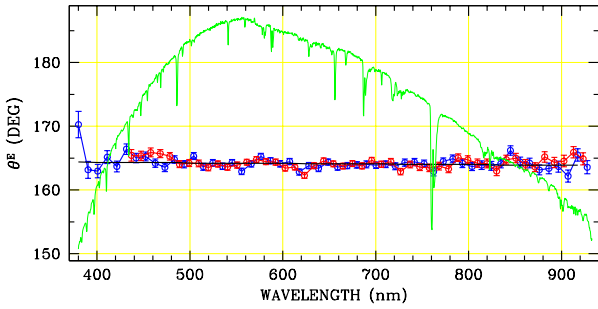
HD66194 2015-05-22



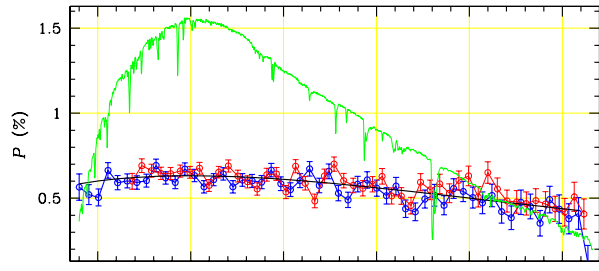
LS908 2015-05-12



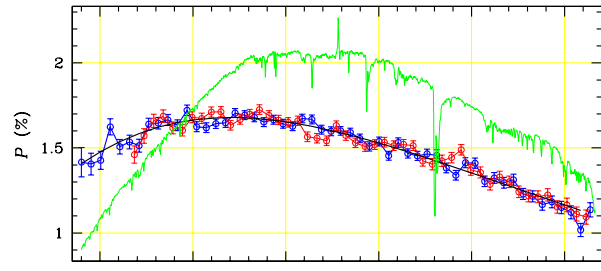
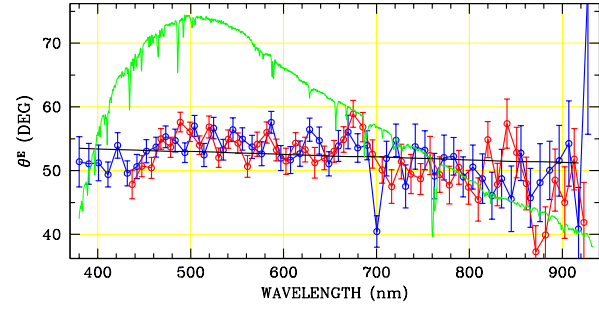
HD73882 2015-05-22



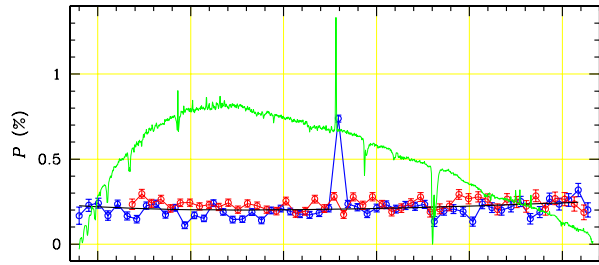
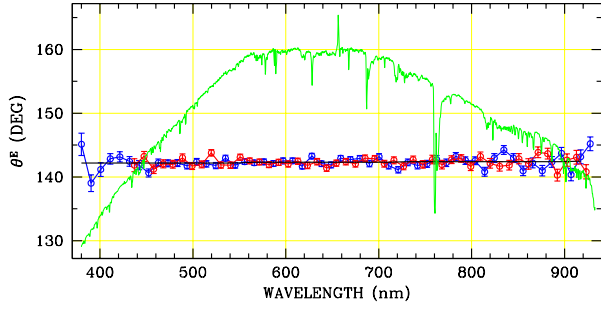




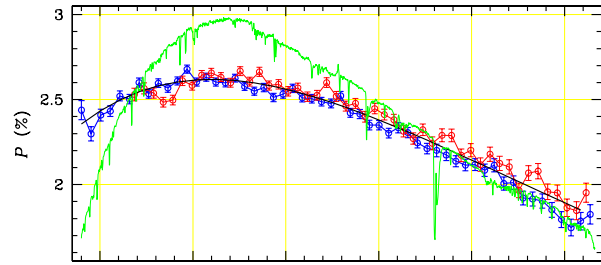
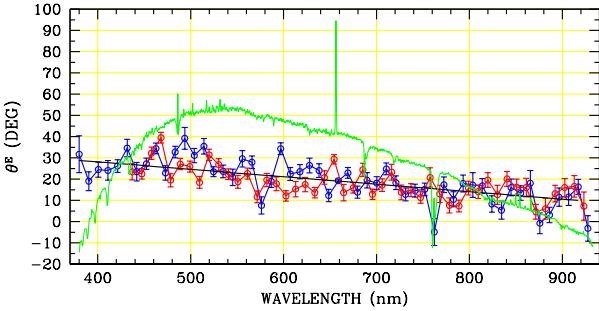
HD75309 2015-05-23



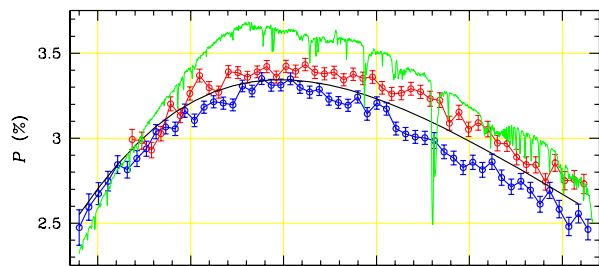
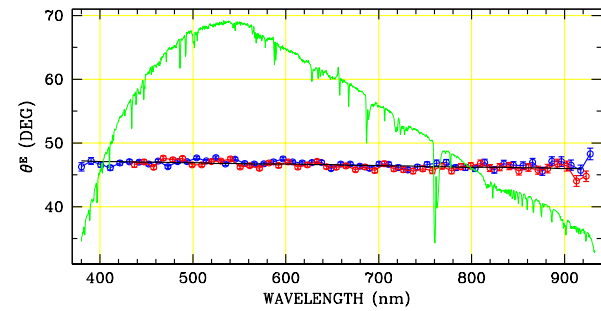
HD75860 2015-05-22



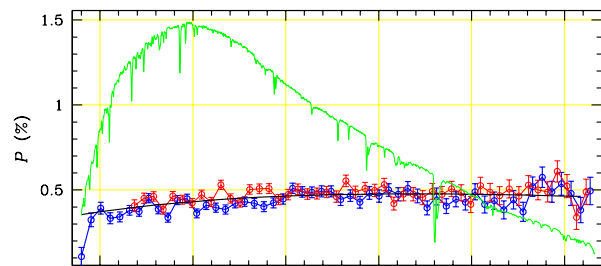
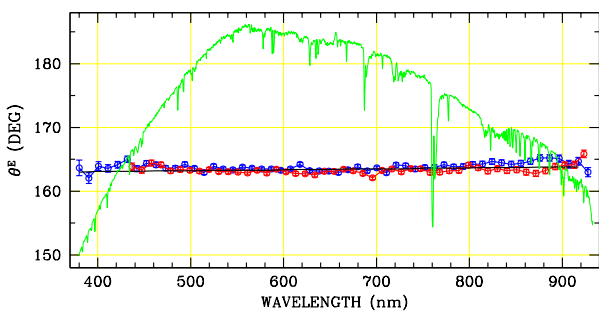
HD76868 2015-05-29



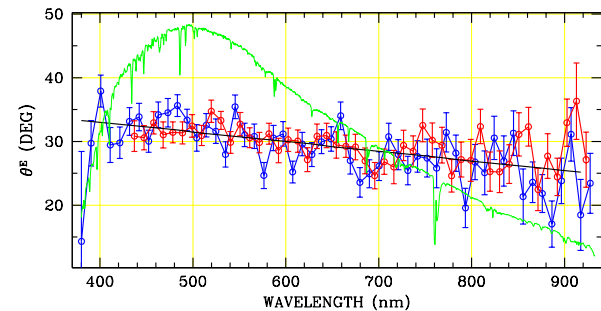
HD79186 2015-05-23

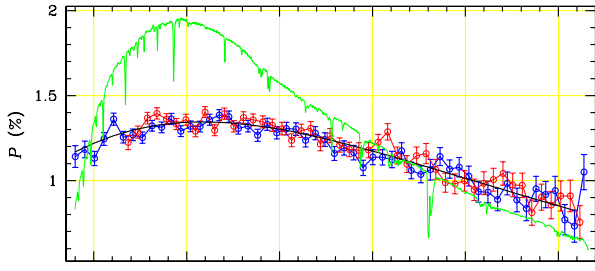


HD80558 2015-05-23

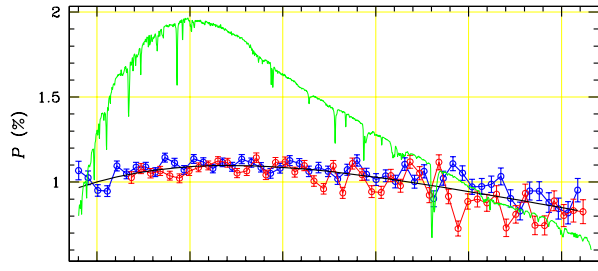


HD89137 2015-05-23

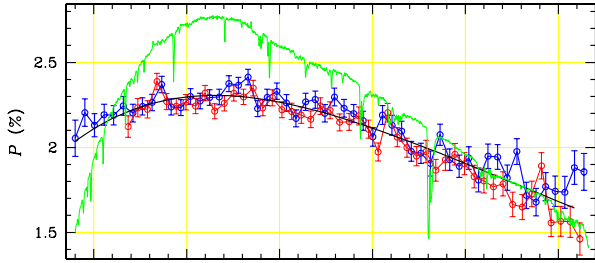
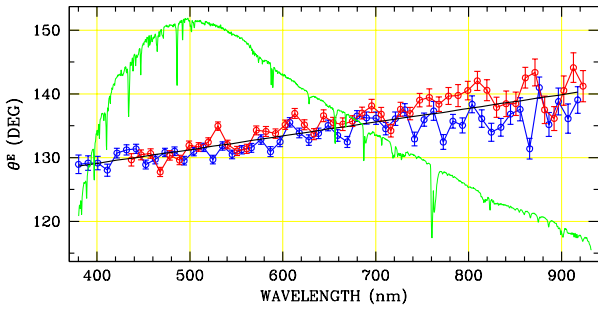
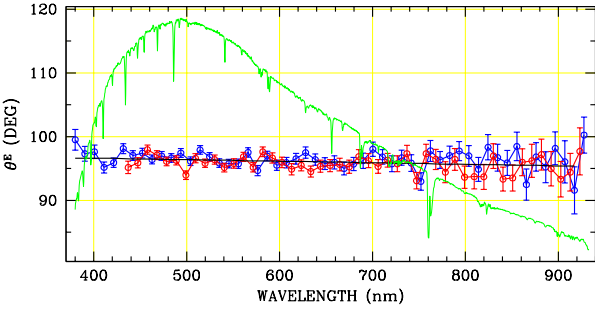




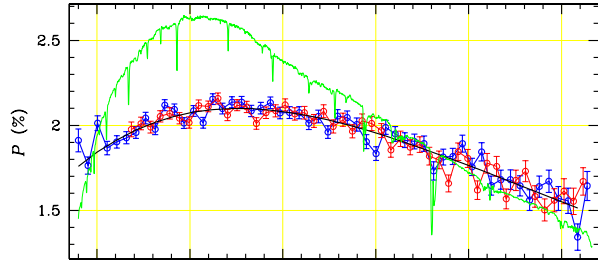
HD91824 2015-05-24



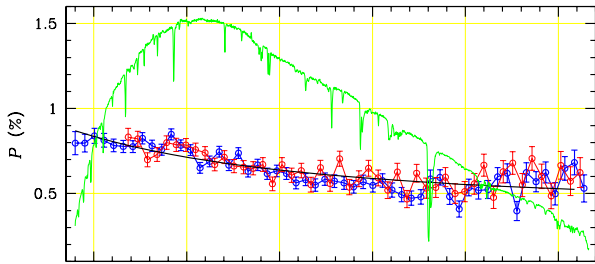
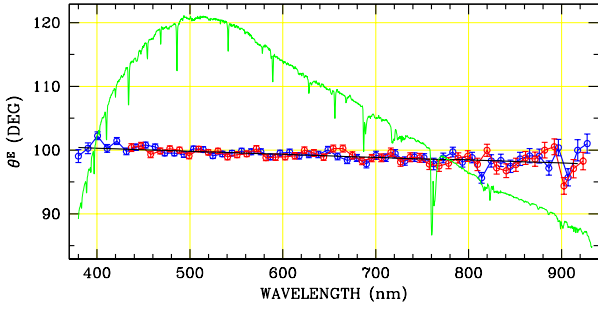
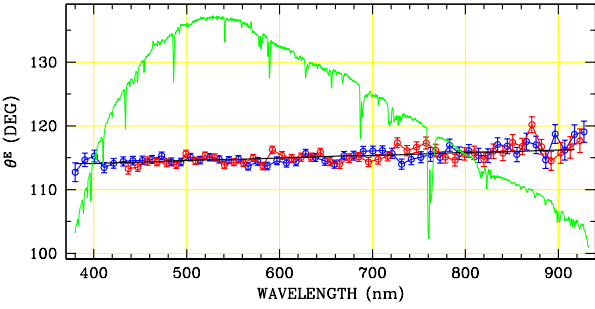
HD91983 2016-01-30



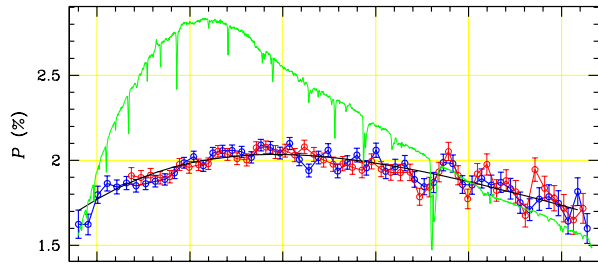
HD93160 2015-05-24



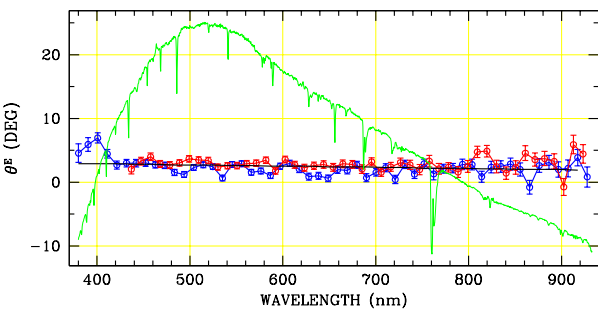
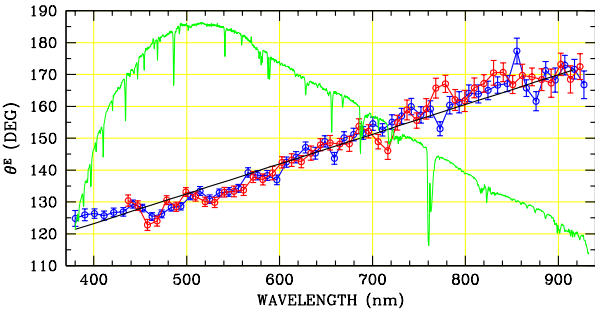
HD93205 2015-05-24

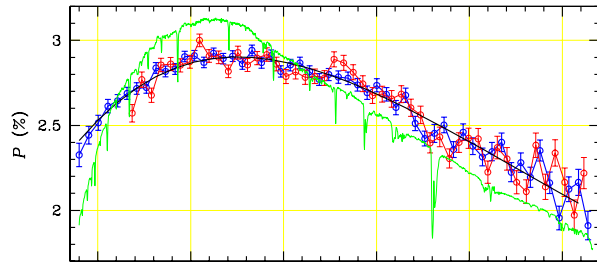


HD93222 2015-05-24

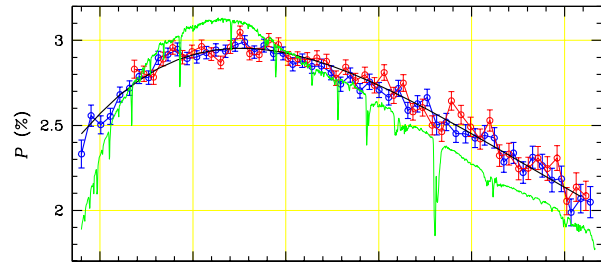


HD96715 2015-05-20

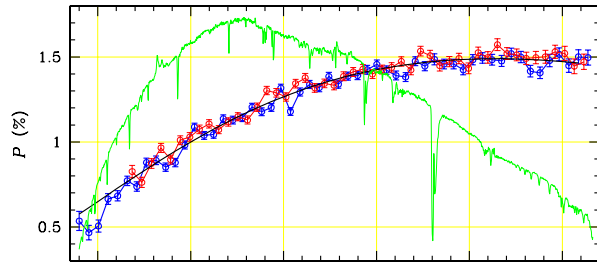
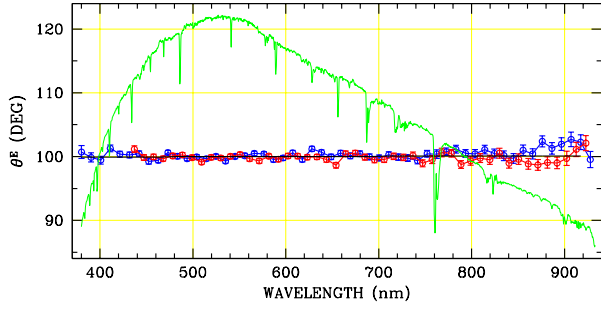
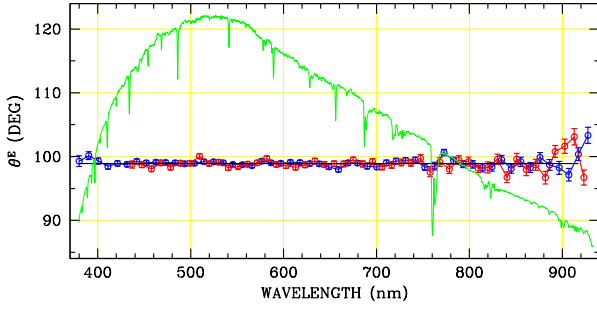




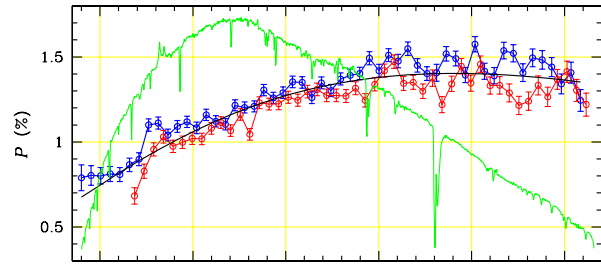
HD303308 2015-05-24



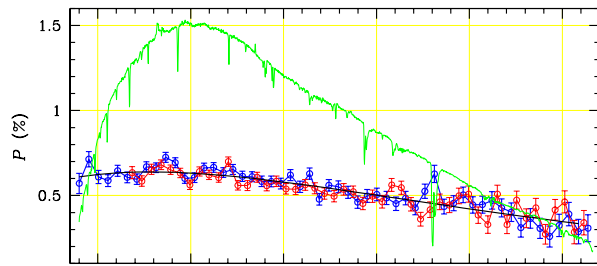
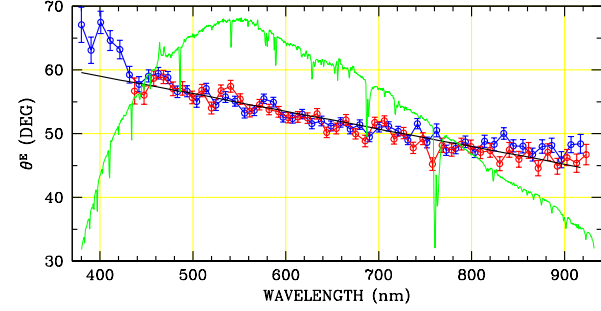
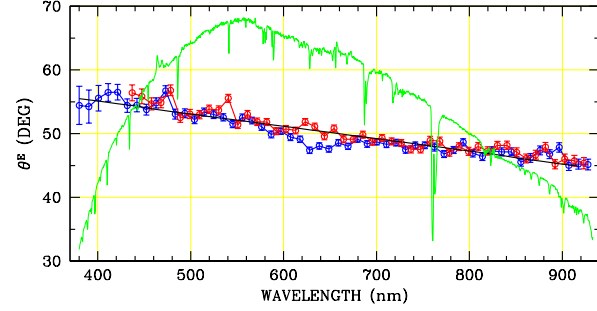
HD303308 2016-01-30



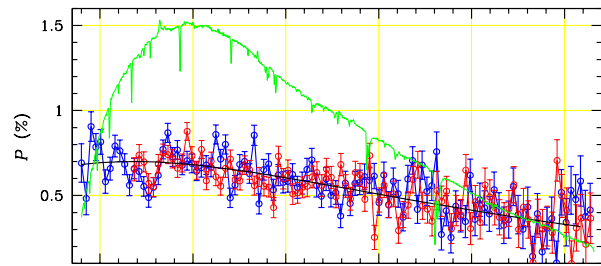
HD93632 2015-05-12



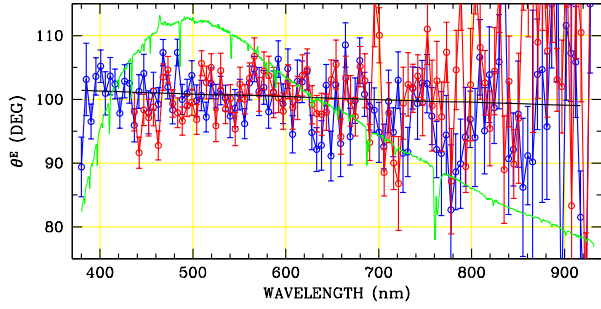
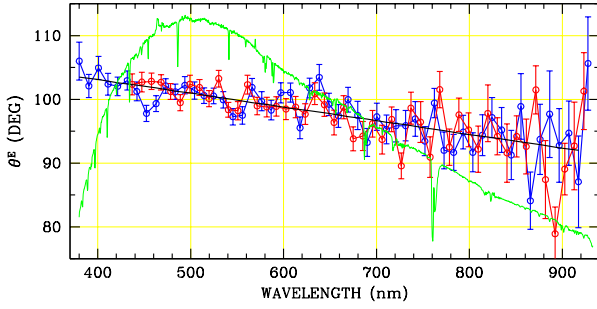
HD93632 2015-12-29

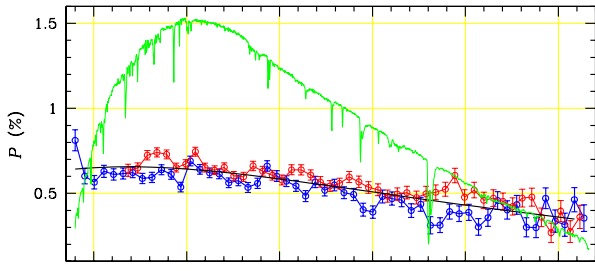


HD93843 2015-05-12

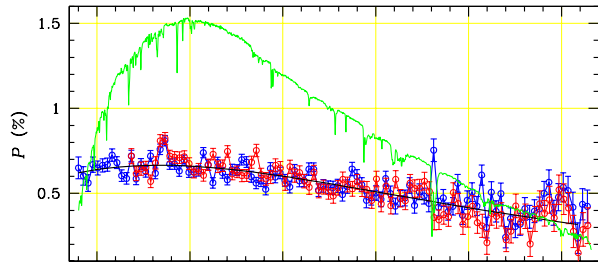


HD93843 2015-12-29

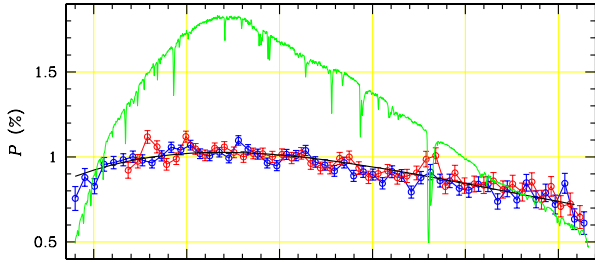
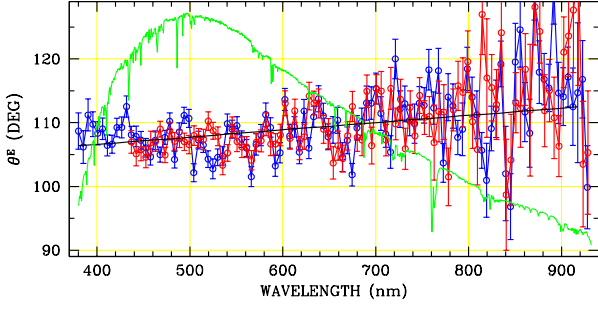
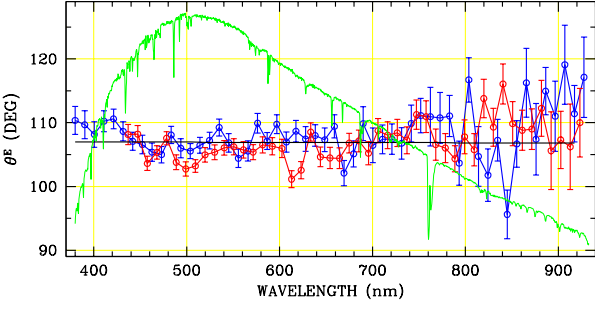




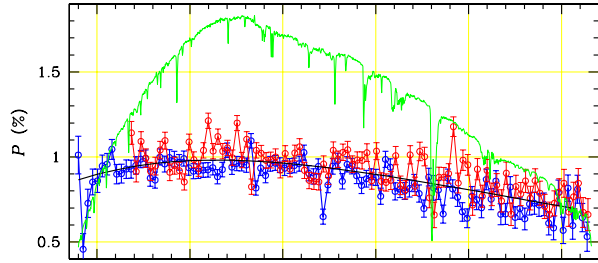
HD94493 2015-05-12



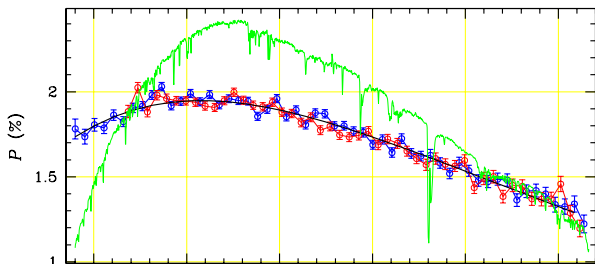
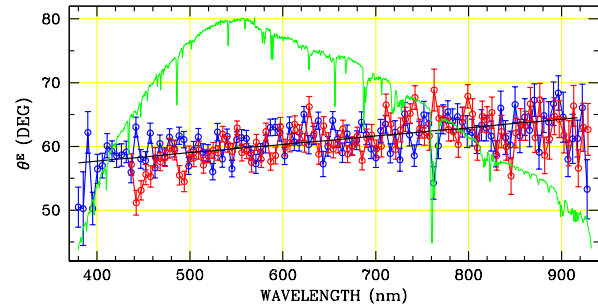
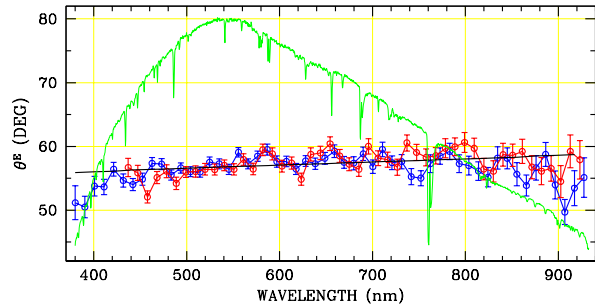
HD94493 2016-01-26



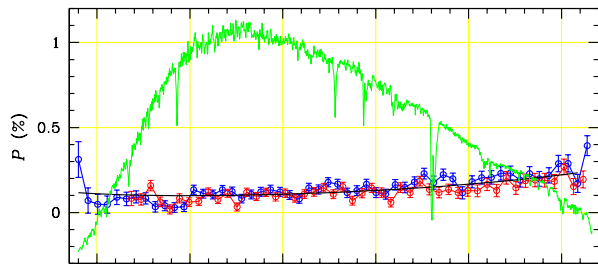
HD97484 2015-05-17



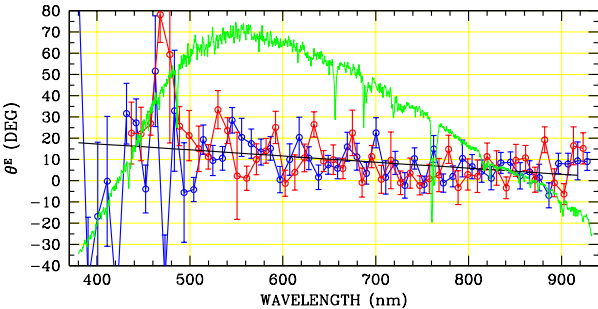
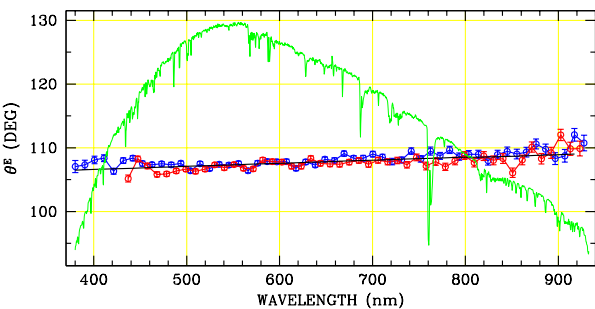
HD97484 2016-02-14

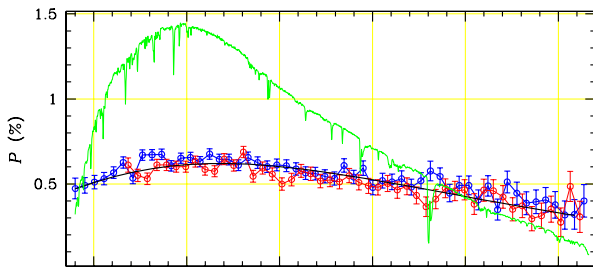


HD99953 2015-05-25

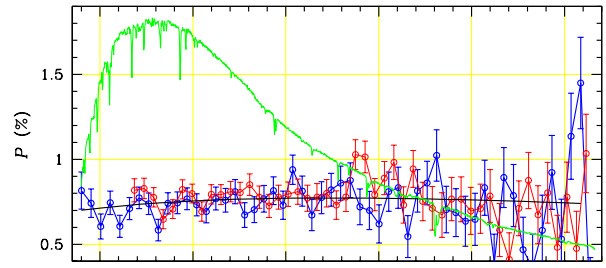
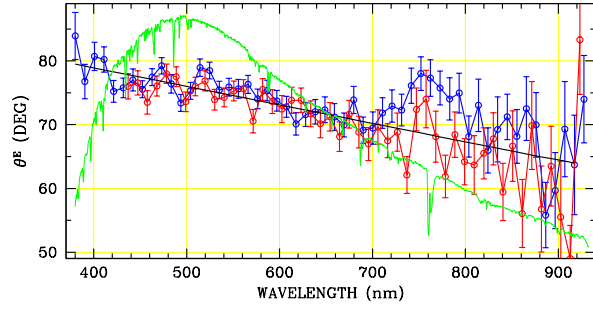


HD101065 2015-05-25

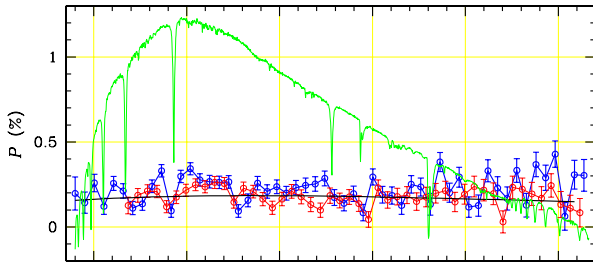
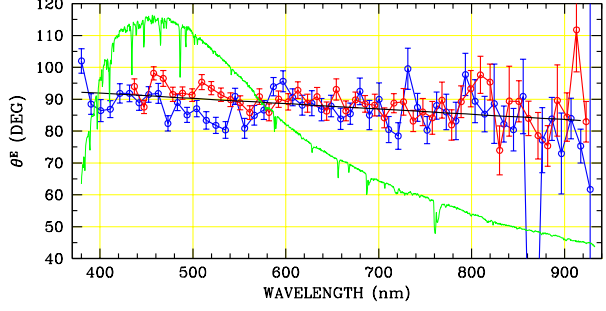




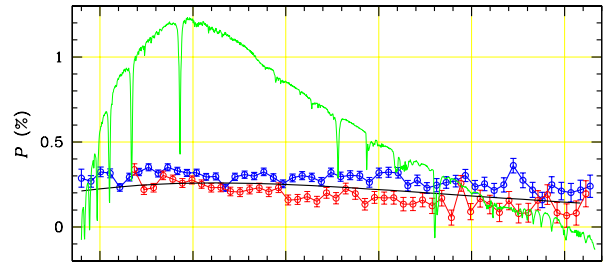
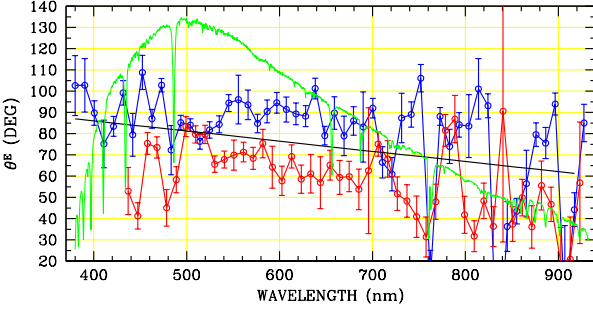
HD103779 2015-05-23



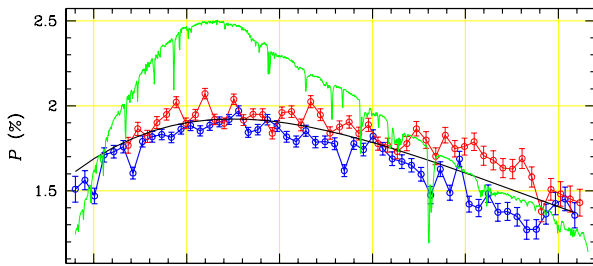
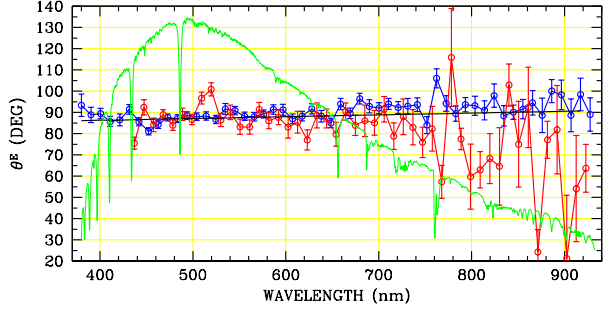
HD104705 2015-05-23



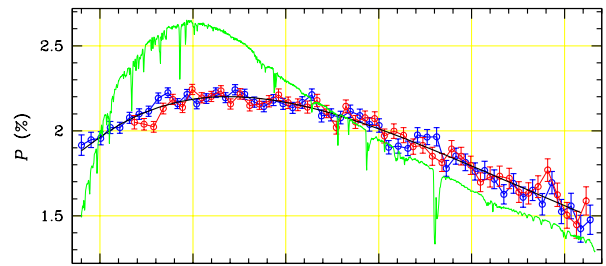
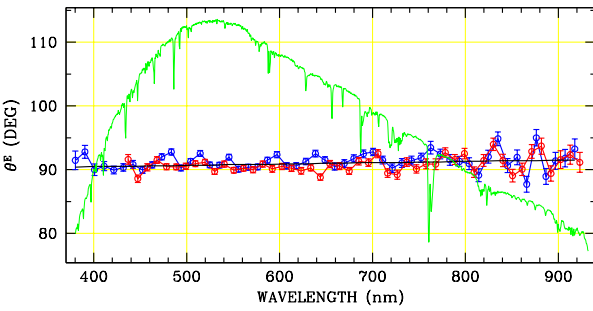
HD105416 2015-05-12



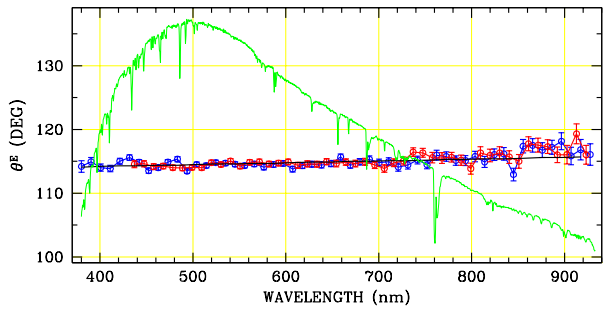
HD105416 2016-02-07

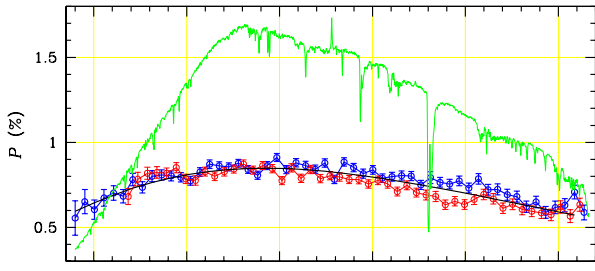


HD108639 2016-01-23

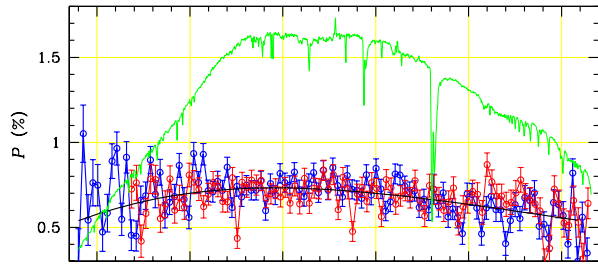


HD109399 2015-05-23

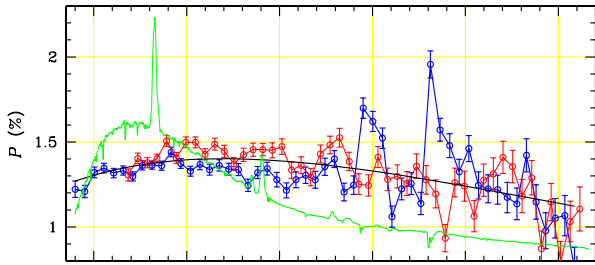
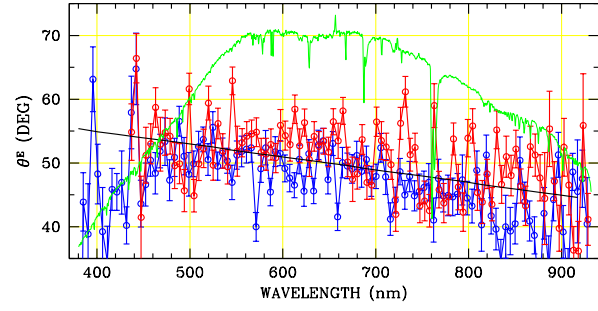
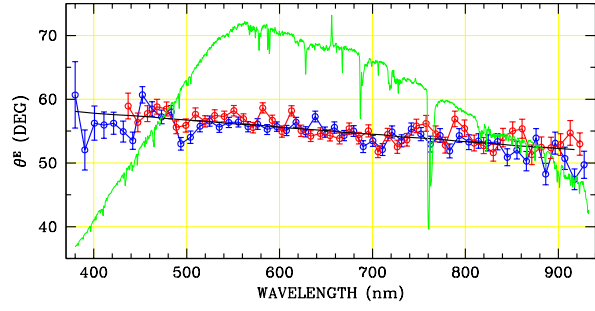




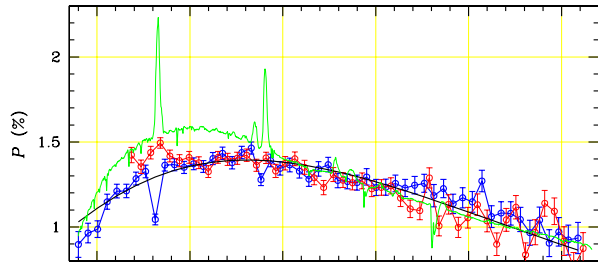
HD112272 2015-04-07



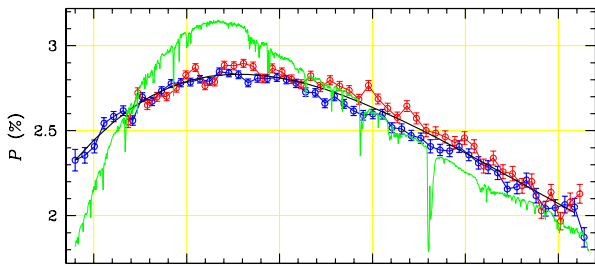
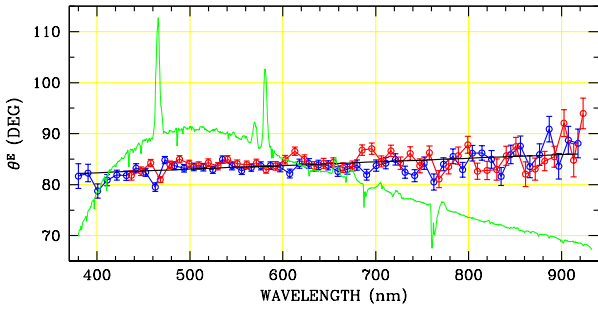
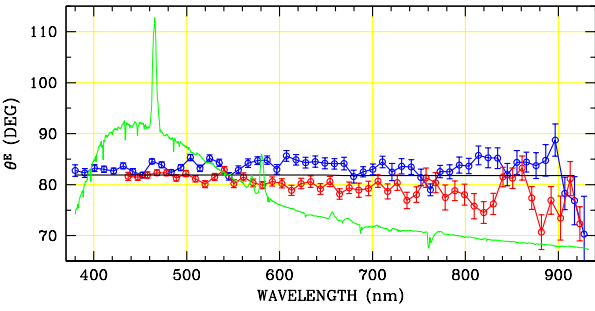
HD112272 2015-12-29



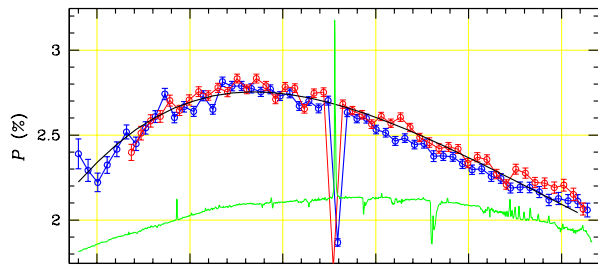
HD113904 2015-04-07



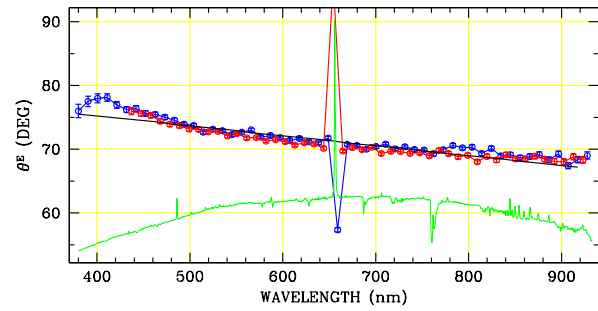
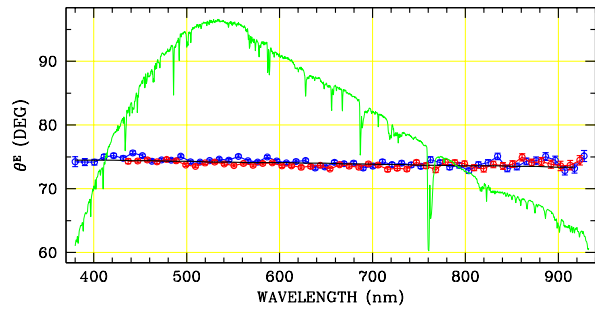
HD113904 2015-12-29

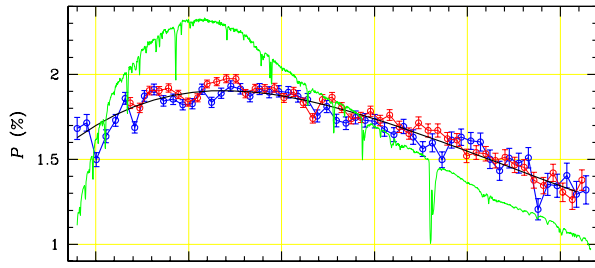


HD111934 2015-04-07

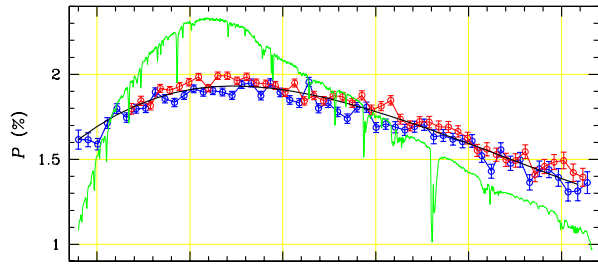


CPD-63 2495 2015-04-07

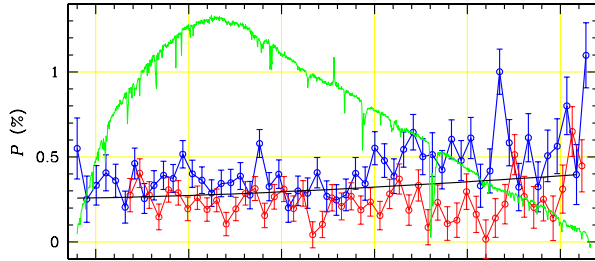
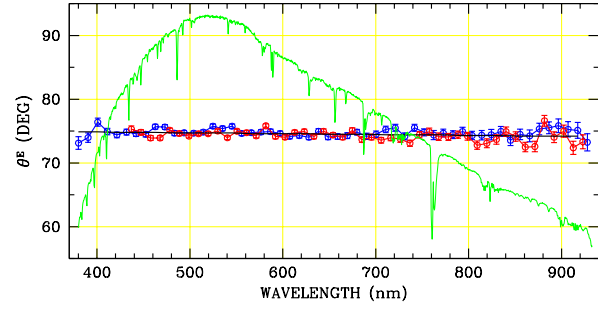
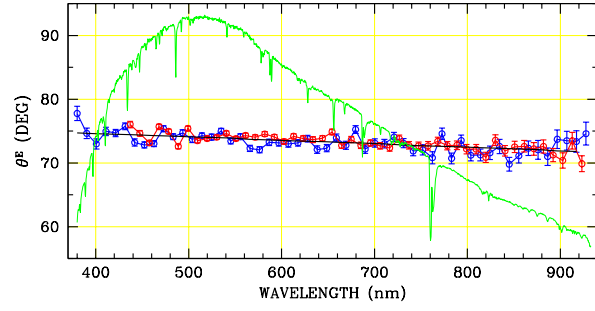




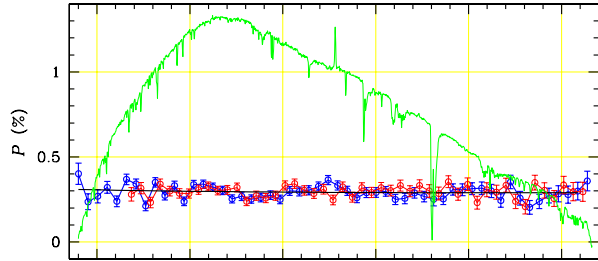
HD114886 2015-05-12



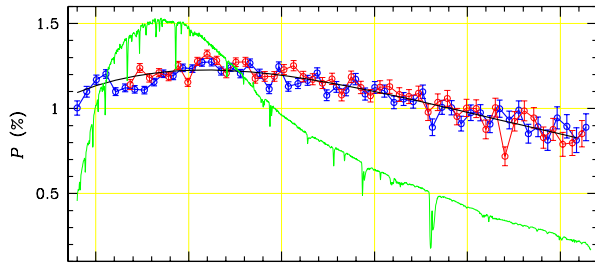
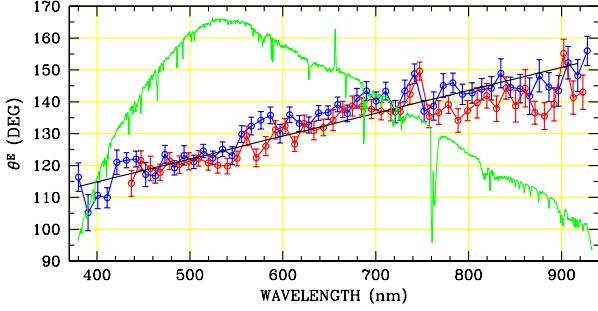
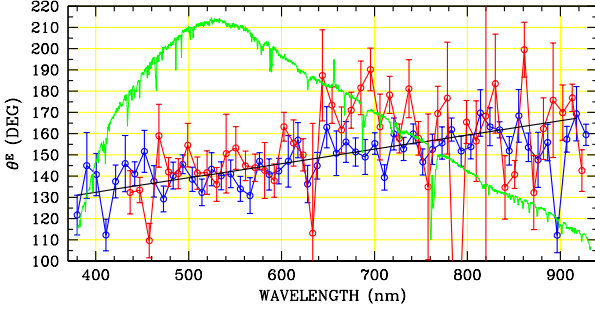
HD114886 2016-01-30



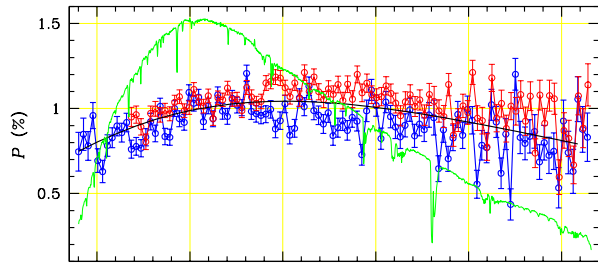
HD115842 2015-05-12



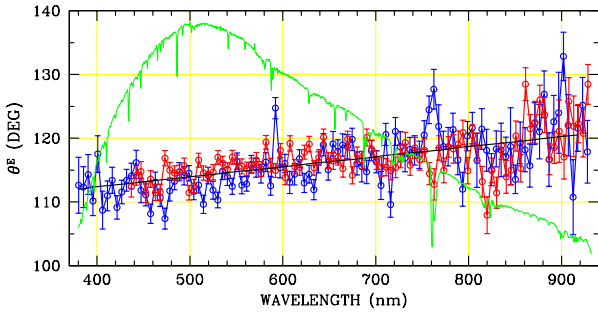
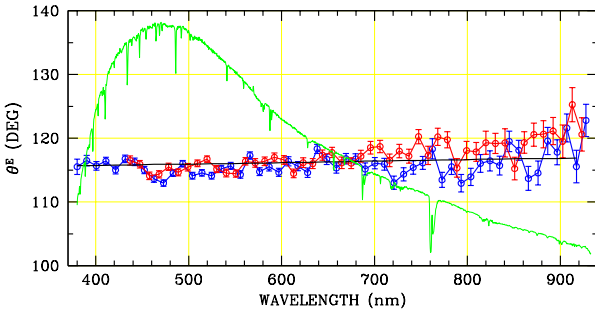
HD115842 2016-01-30

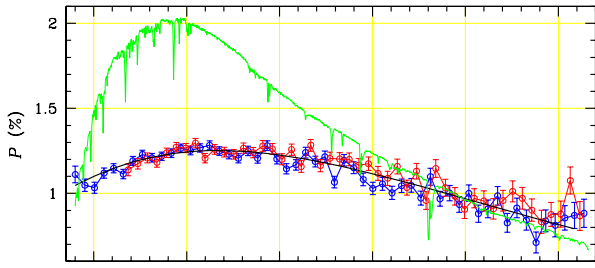


HD116852 2015-05-12

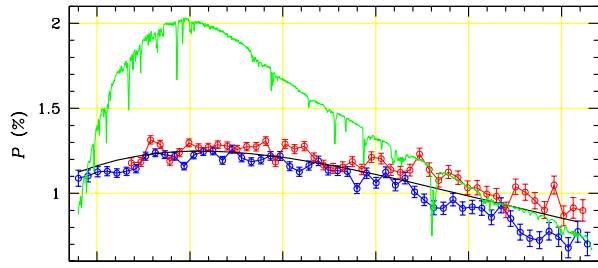


HD116852 2016-02-22

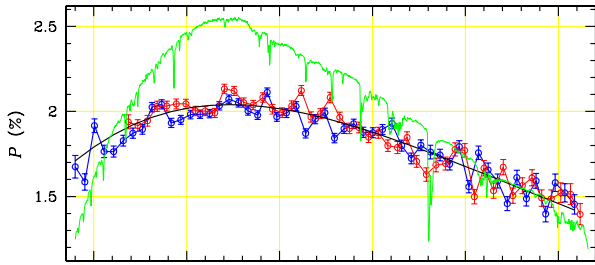
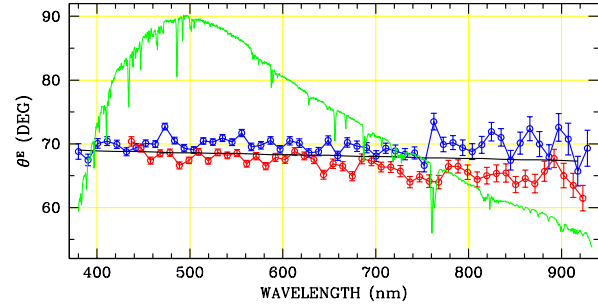
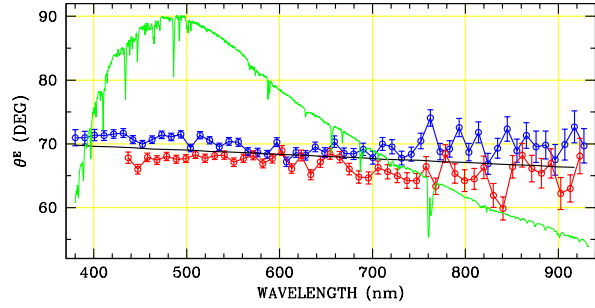




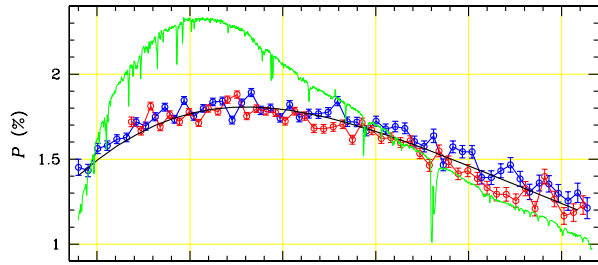
HD119159 2015-05-12



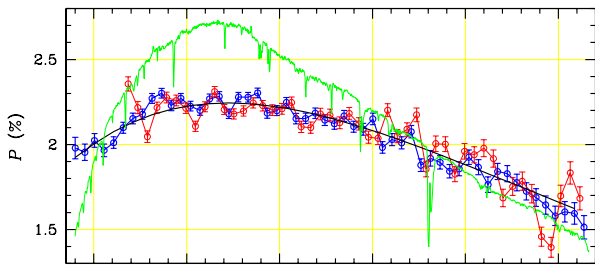
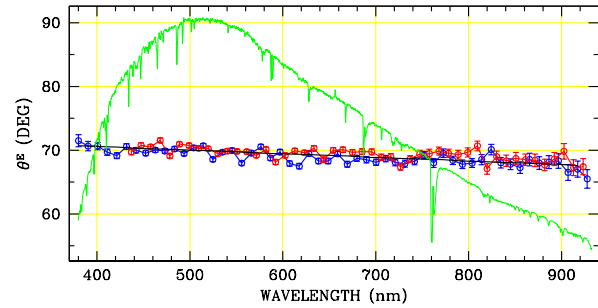
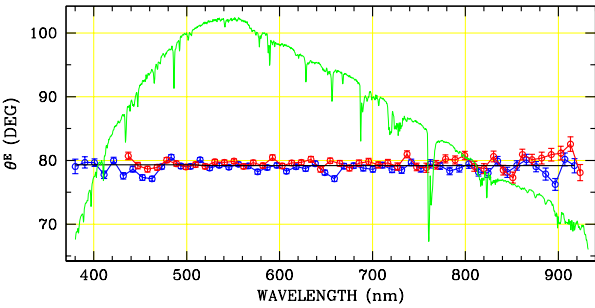
HD119159 2016-01-28



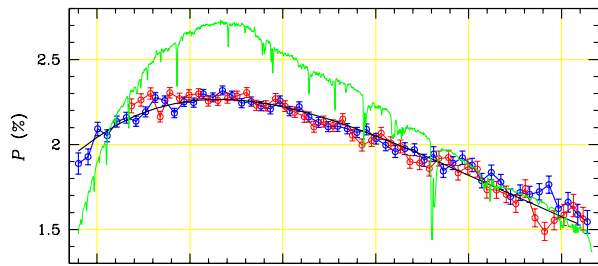
HD115071 2016-01-26



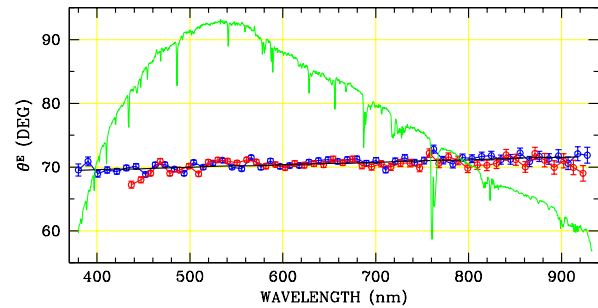
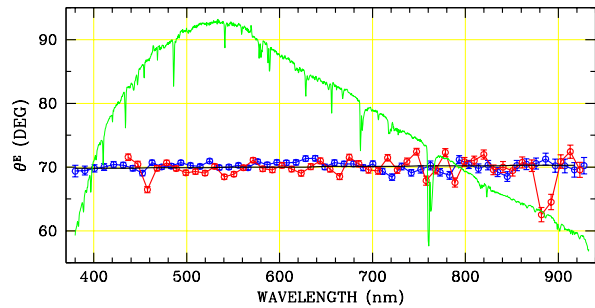
HD122879 2015-05-12



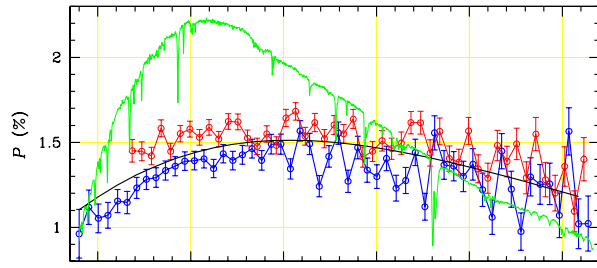
HD124314 2015-05-12



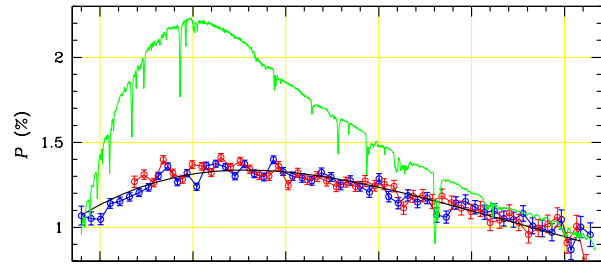
HD124314 2016-02-22



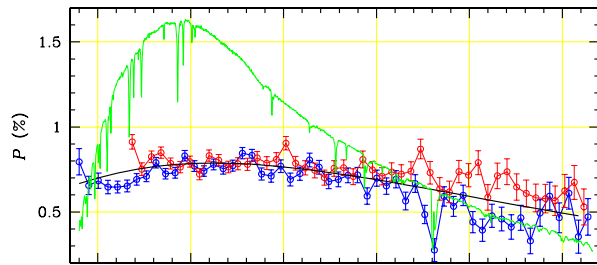
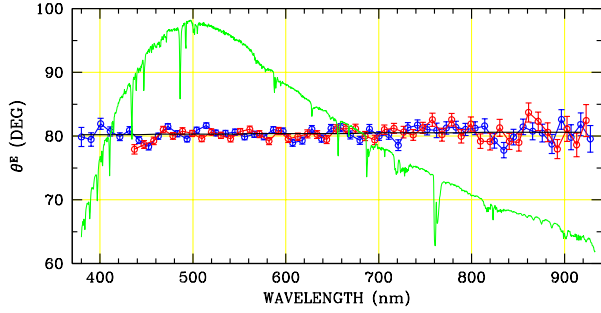
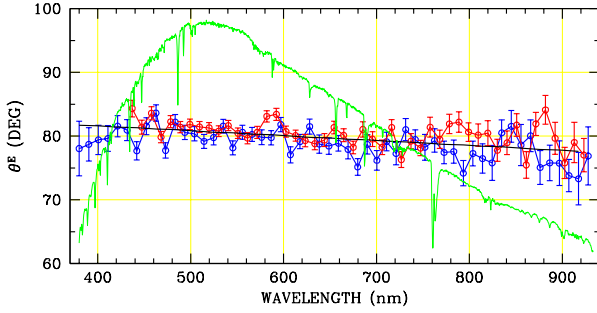




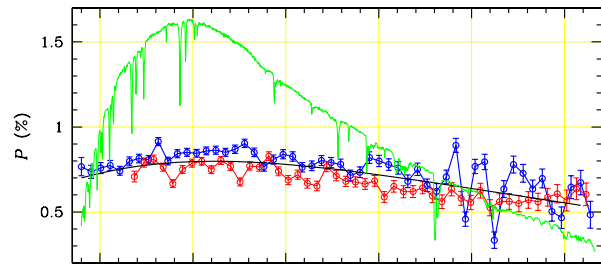
HD129557 2015-05-11



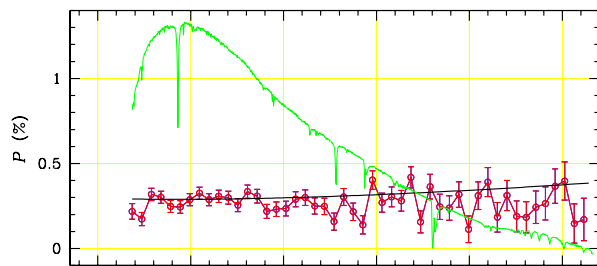
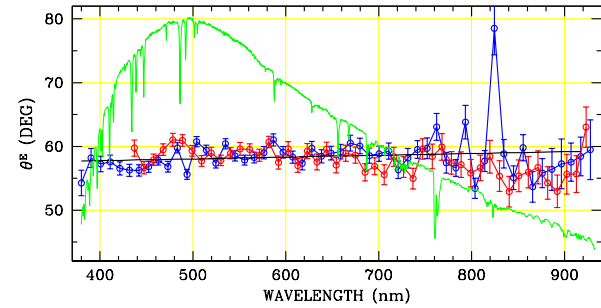
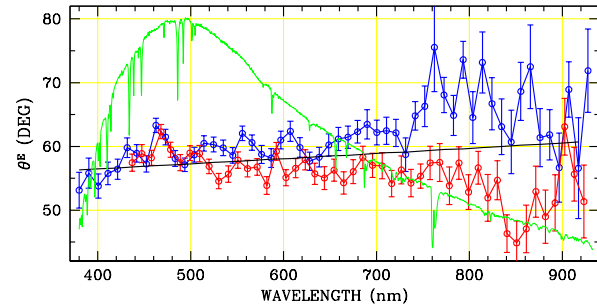
HD129557 2016-02-22



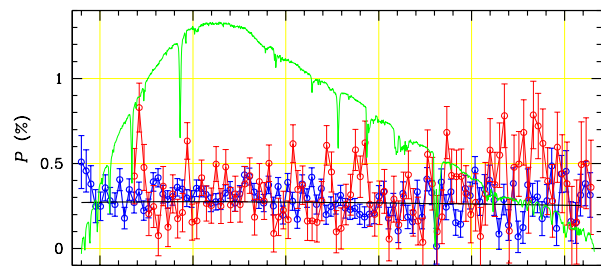
HD133518 2015-05-11



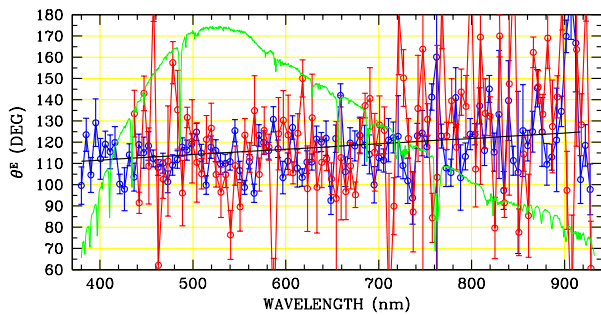
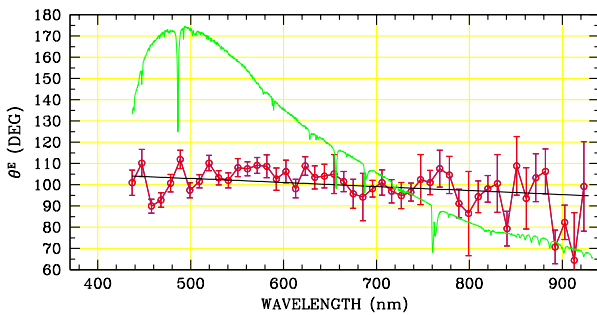
HD133518 2016-02-12

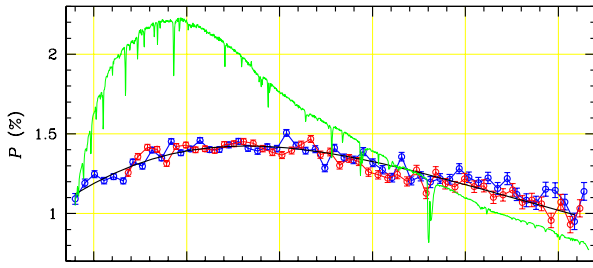


HD134591 2015-05-12

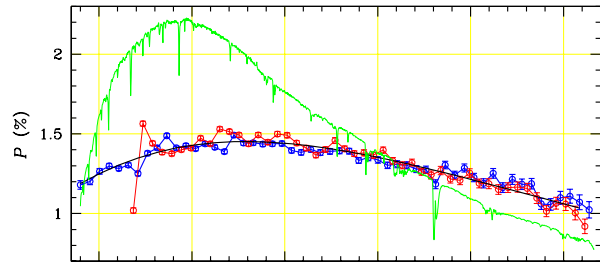


HD134591 2016-02-22

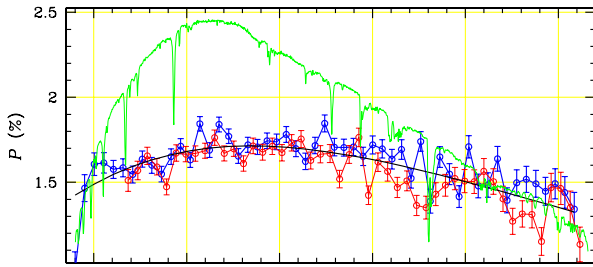
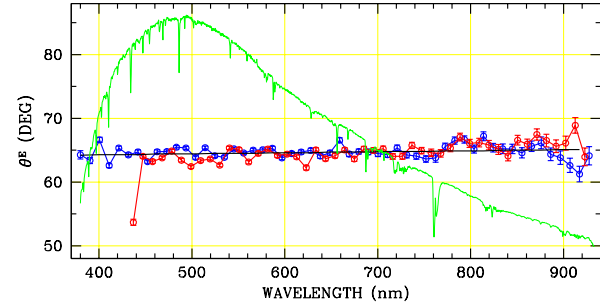
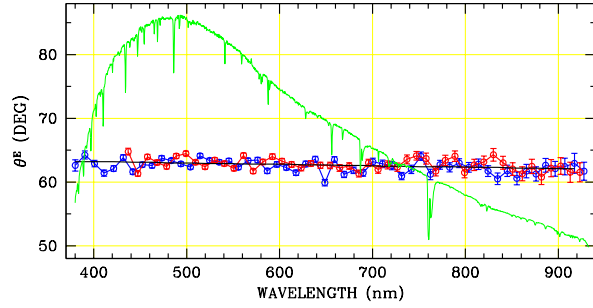




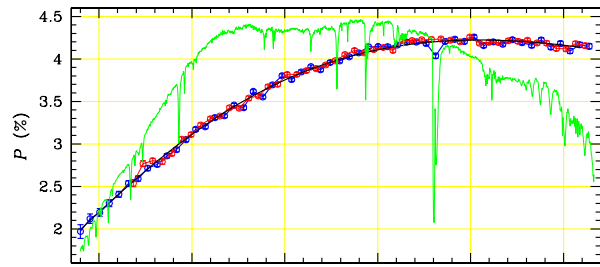
HD135591 2015-05-12



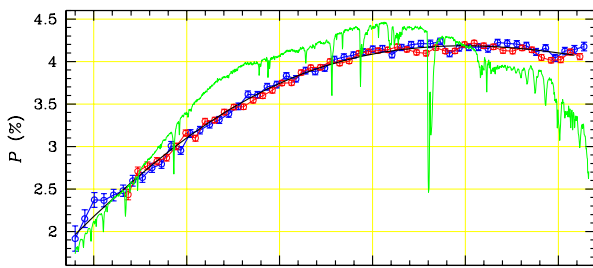
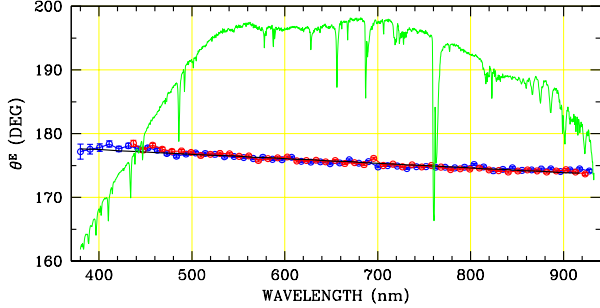
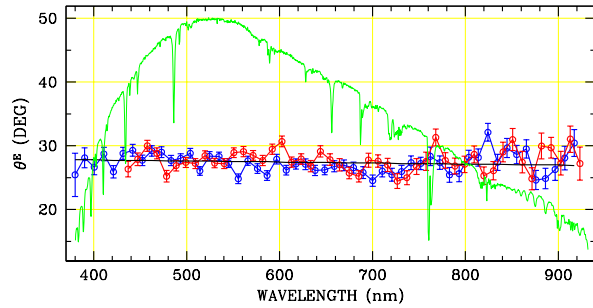
HD135591 2016-01-29



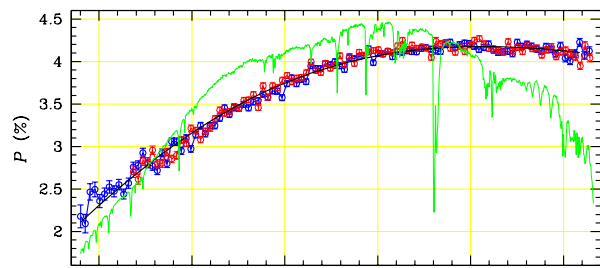
HD147683 2016-02-12



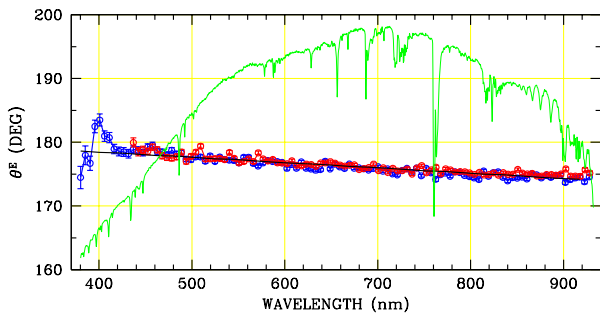
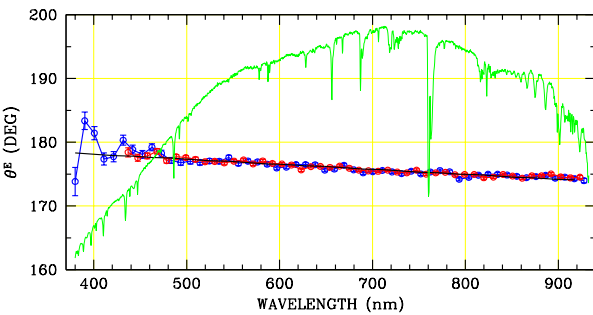
HD147889 2015-05-13

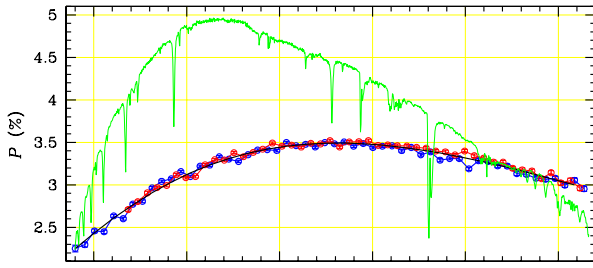


HD147889 2015-05-24

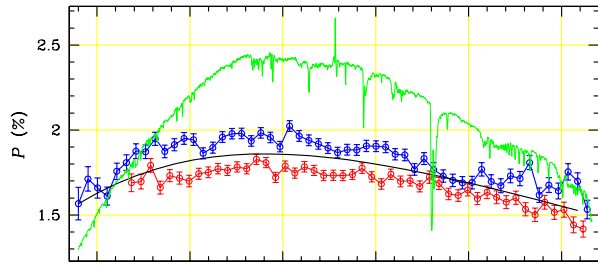


HD147889 2016-01-28

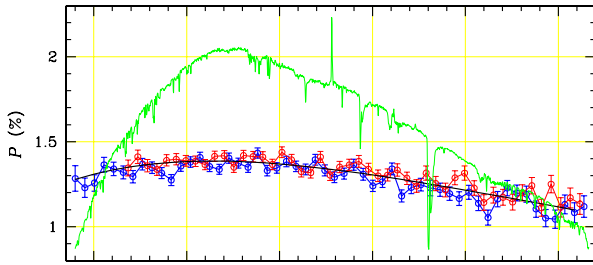
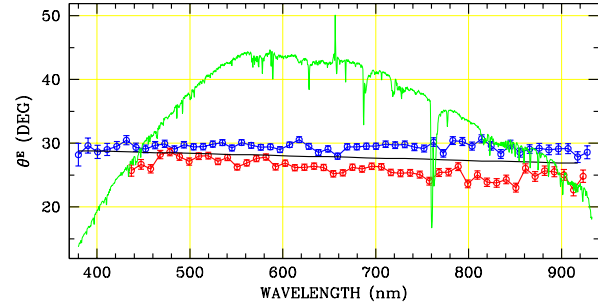
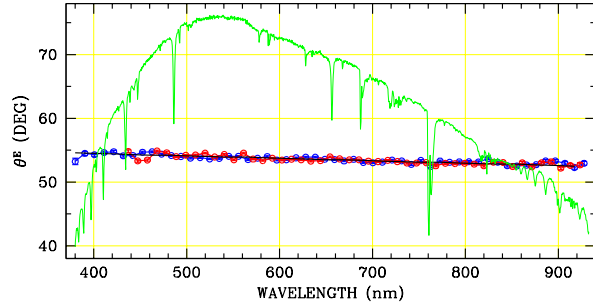




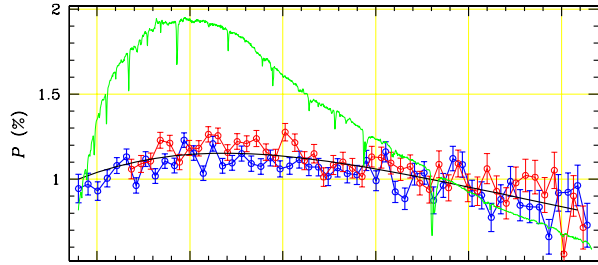
HD147888 2016-01-30



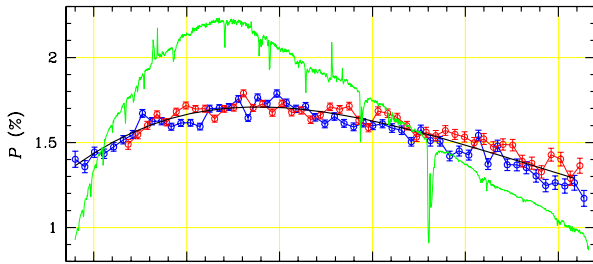
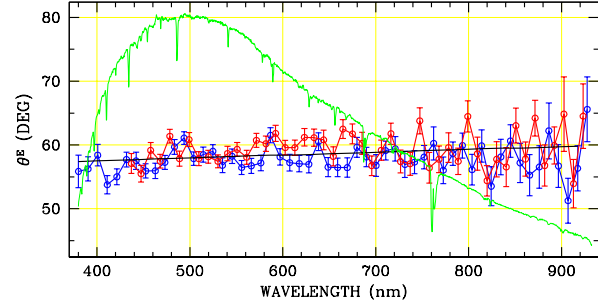
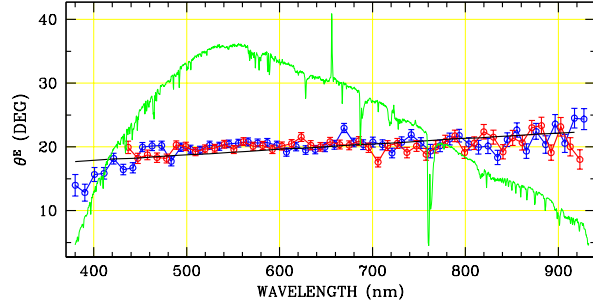
HD148379 2015-05-11



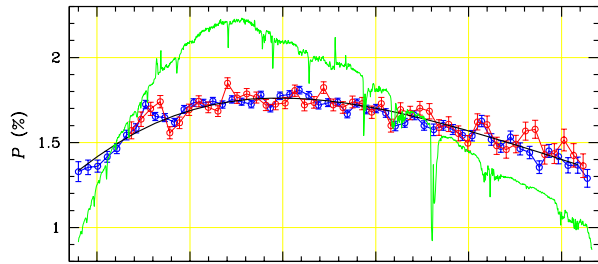
HD148688 2015-05-11



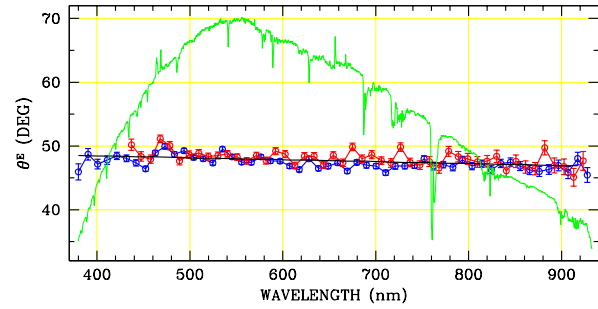
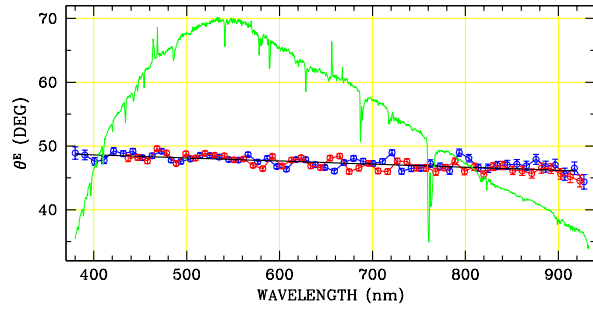
HD150136 2015-05-20

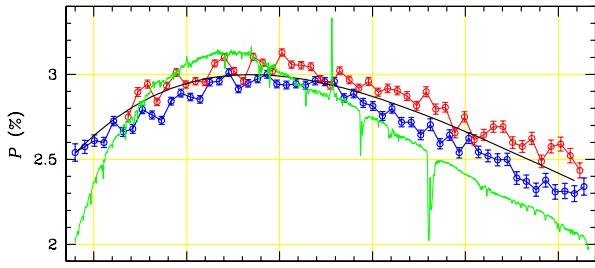


HD148937 2015-05-12

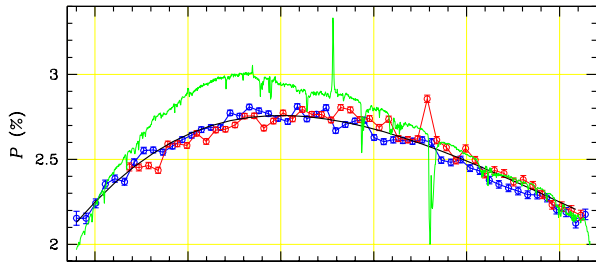
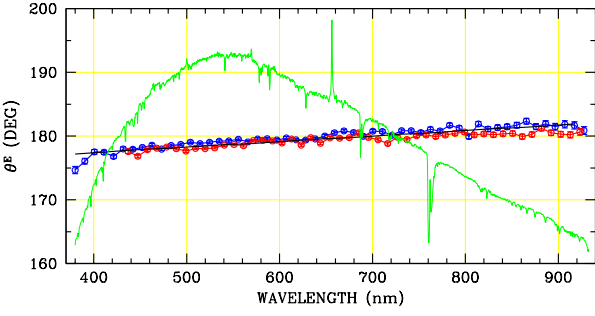


HD148937 2016-02-12

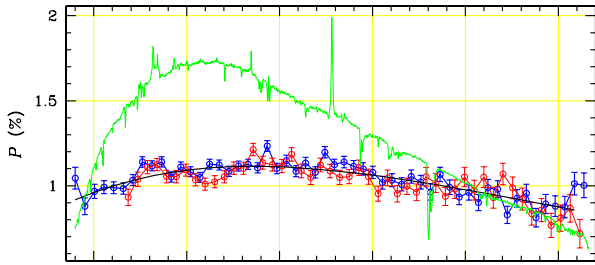
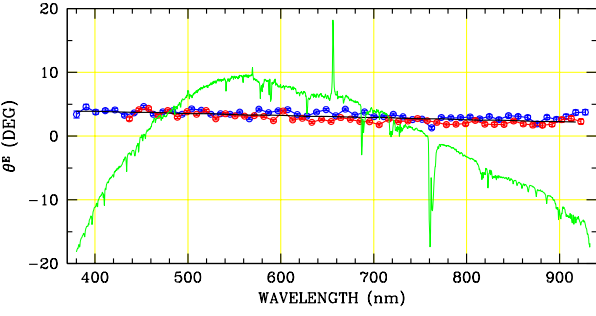




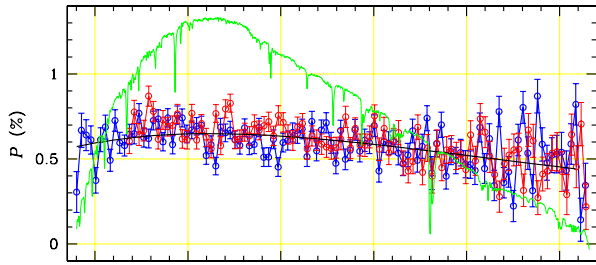
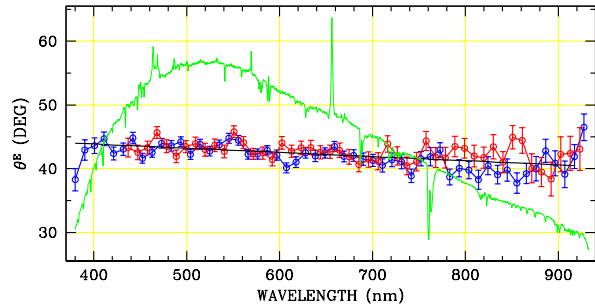
HD149404 2015-05-12



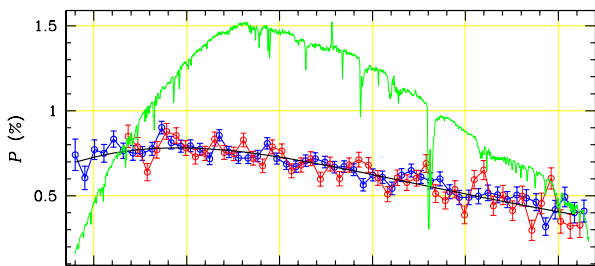
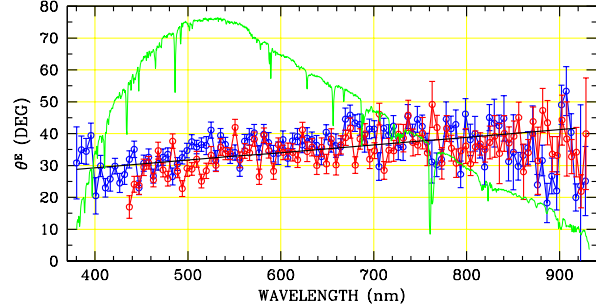
HD149404 2016-01-30



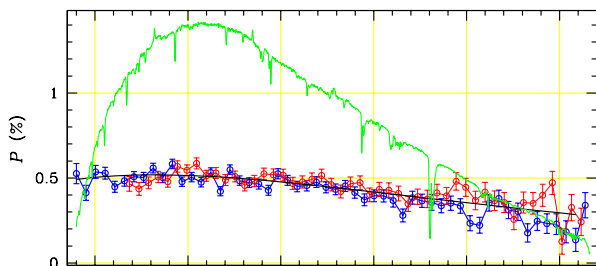
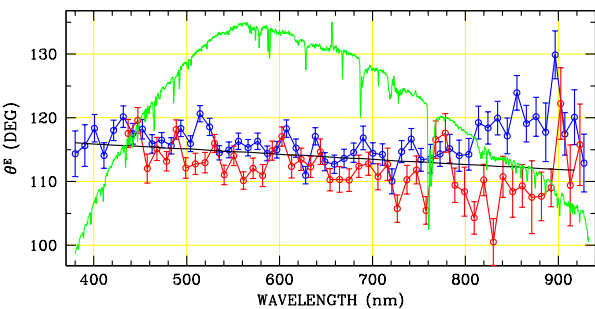
HD151804 2015-05-24



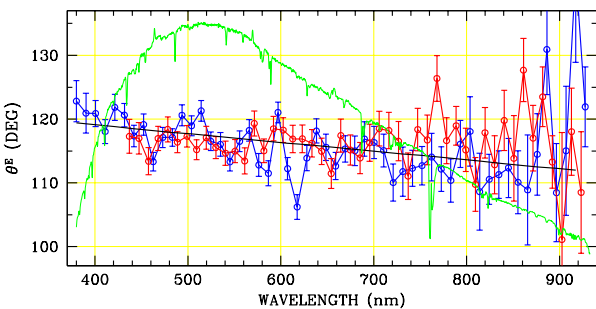
HD151805 2016-02-22

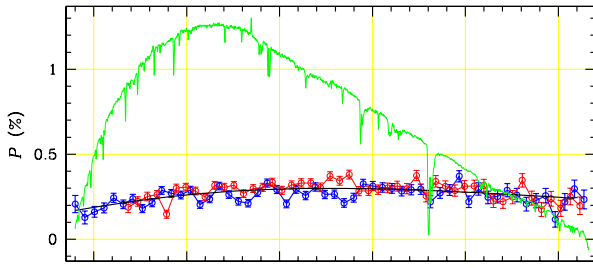


HD152235 2015-05-24

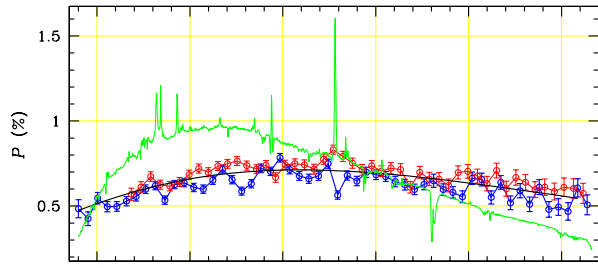
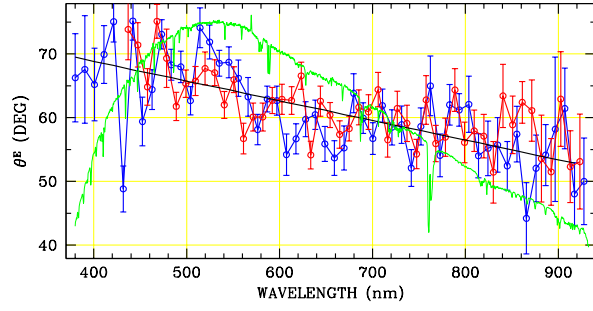


HD152248 2015-05-24

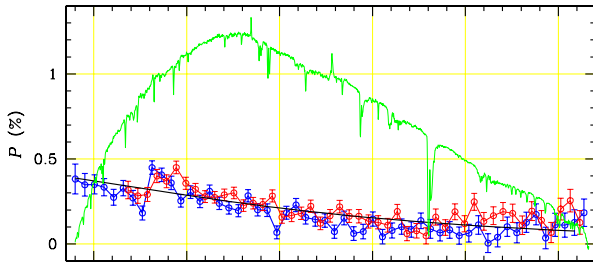
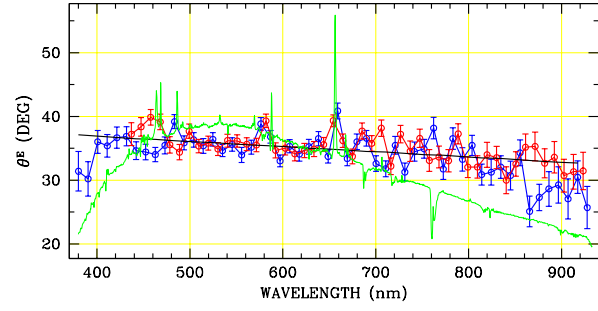




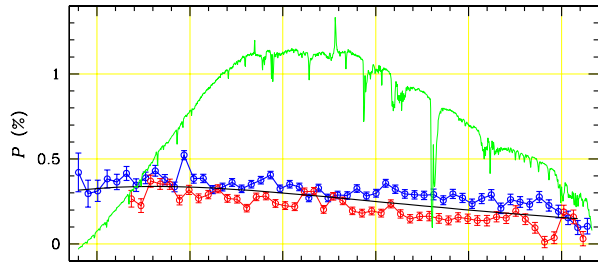
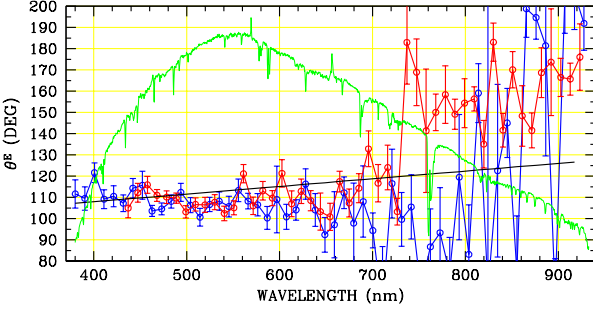
HD152249 2015-05-24



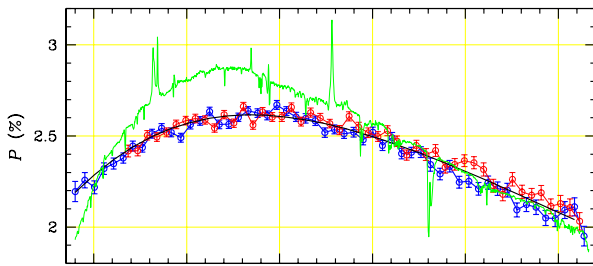
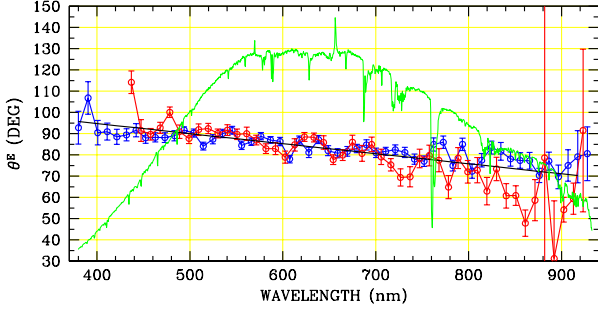
HD152408 2015-05-24



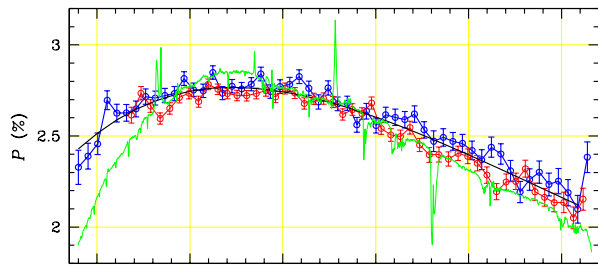
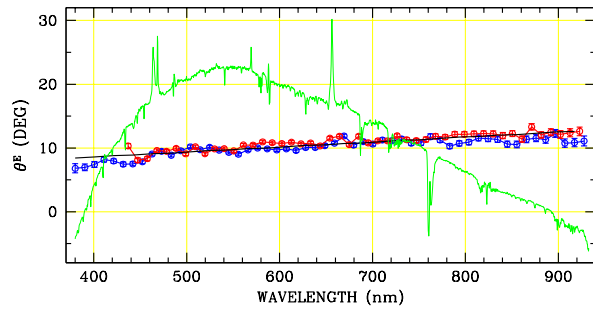
HD152424 2015-05-24



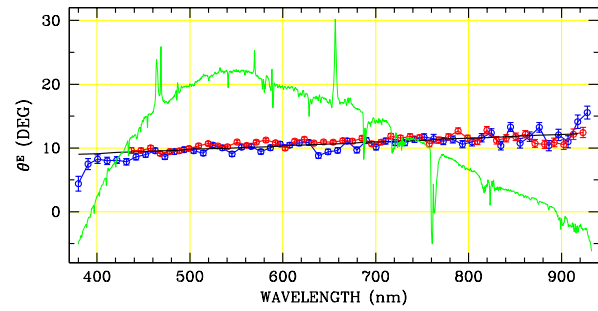
HD152424 2016-02-12

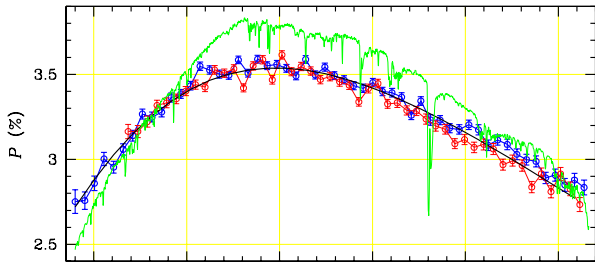


HD153919 2015-04-12

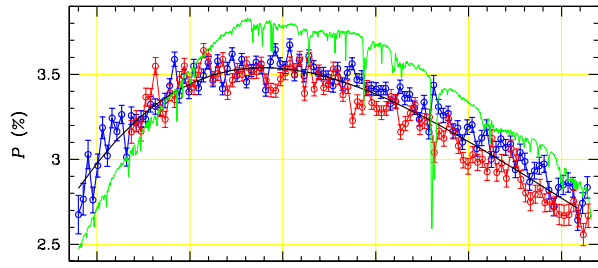


HD153919 2016-02-22

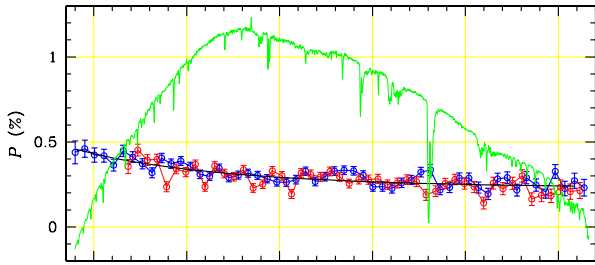
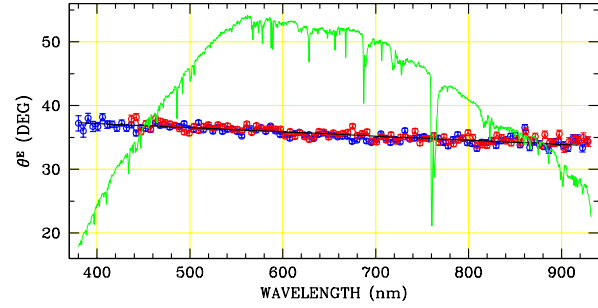
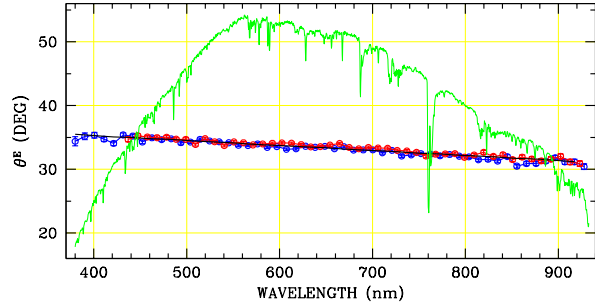




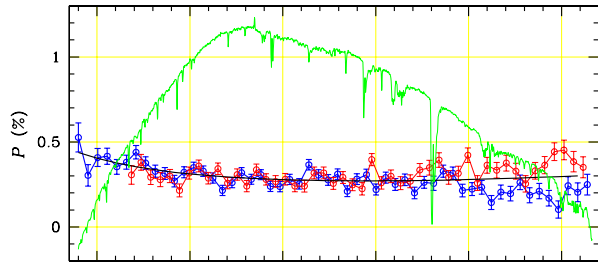
HD154043 2015-04-12



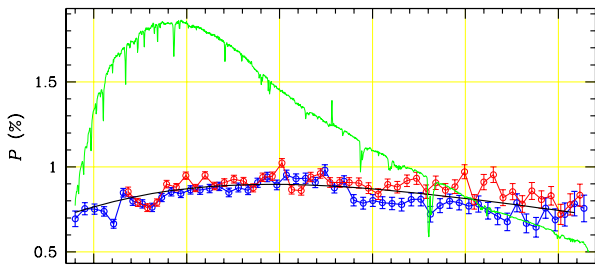
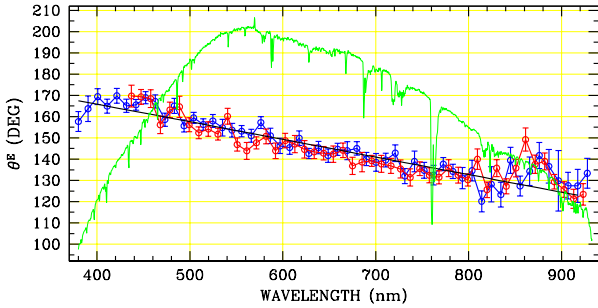
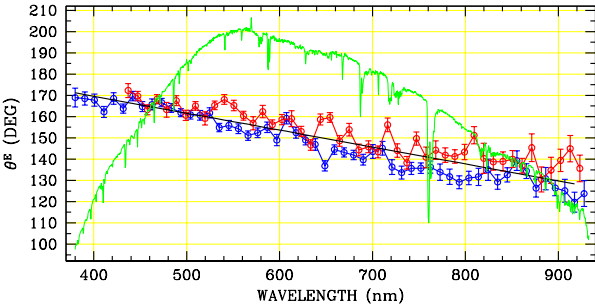
HD154043 2016-02-02



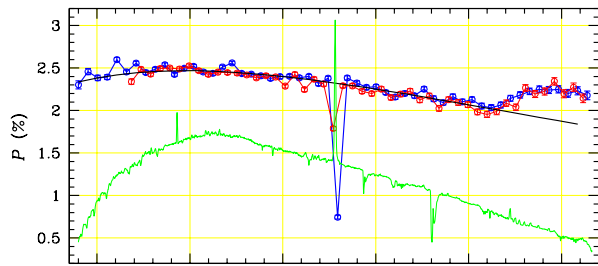
HD154368 2015-04-12



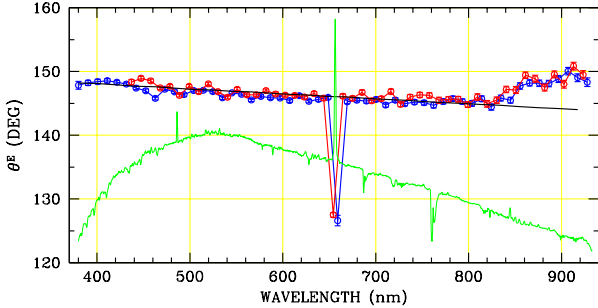
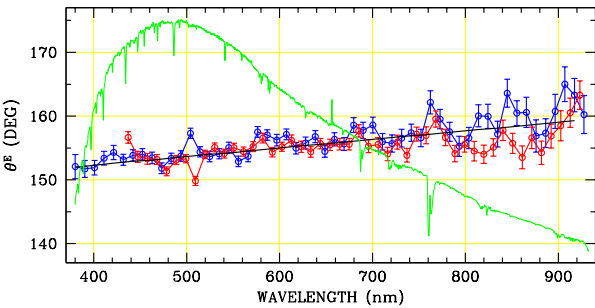
HD154368 2016-02-22

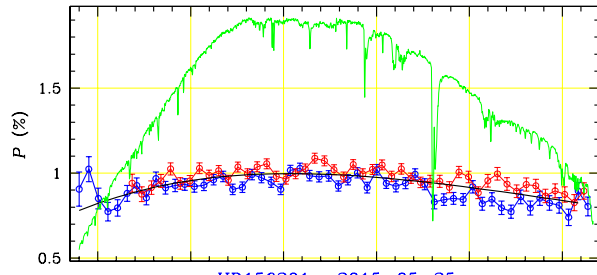


HD155806 2015-05-24

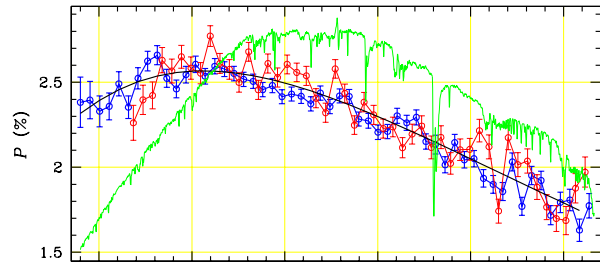


HD155851 2015-05-24

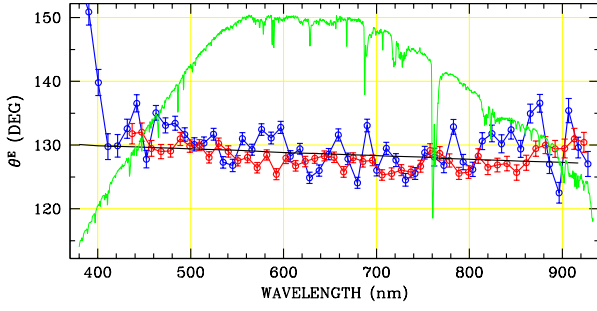




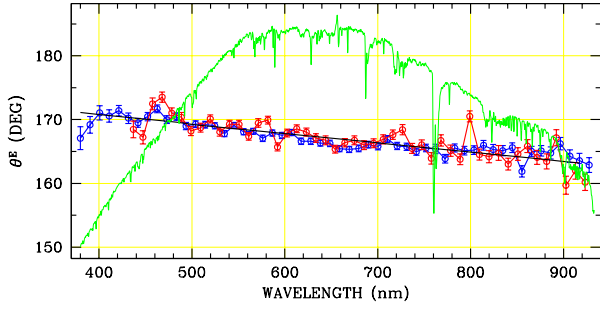
HD156201 2015-05-25



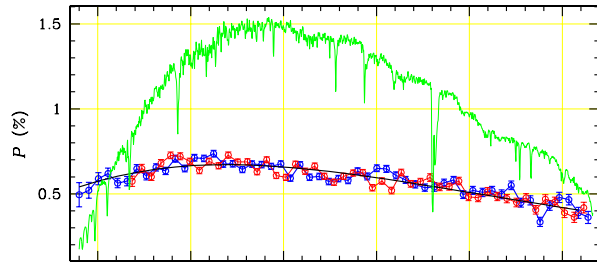
HD157038 2015-05-25



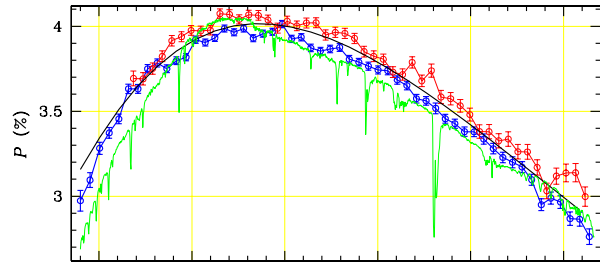
HD157978 2016-03-14



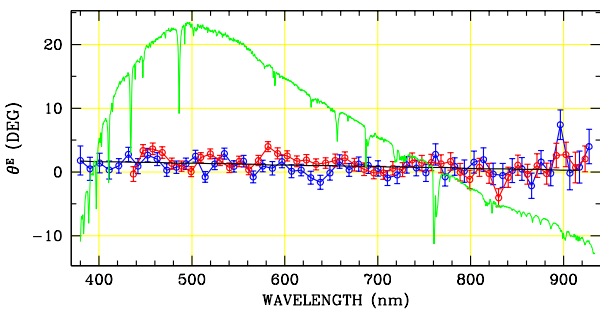
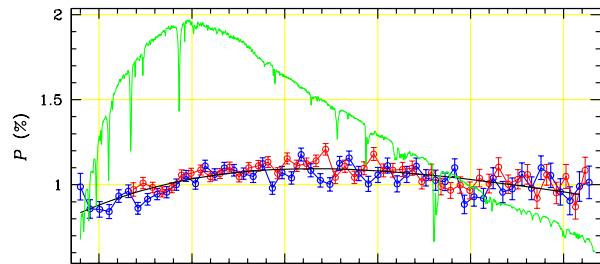
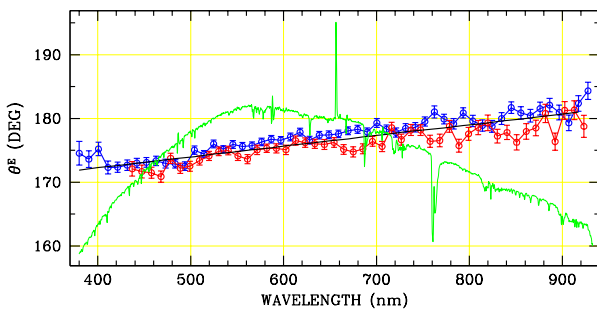
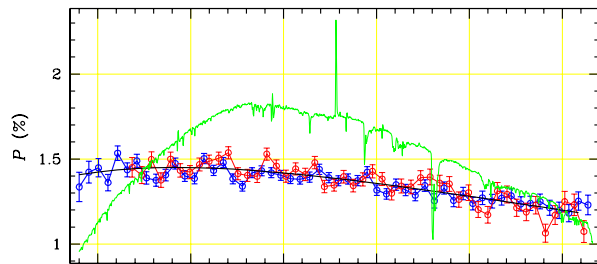
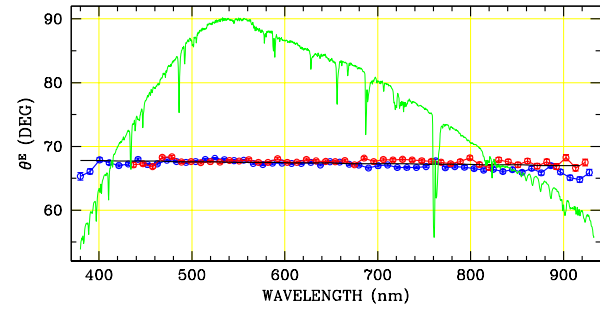
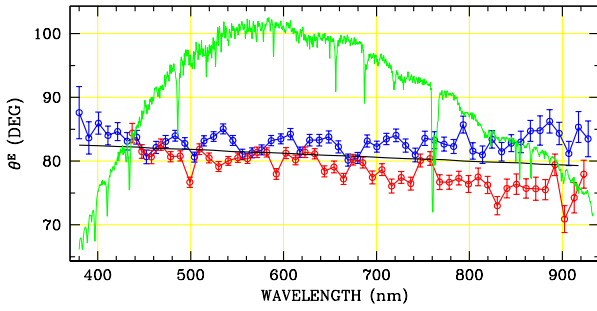
HD161056 2016-02-17

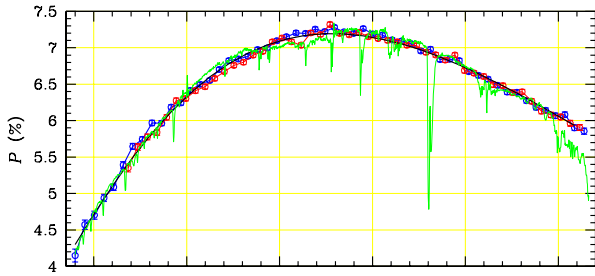


HD163181 2015-05-25

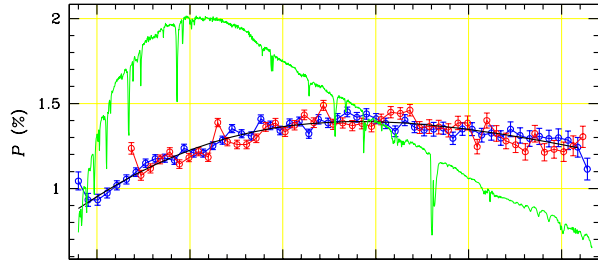
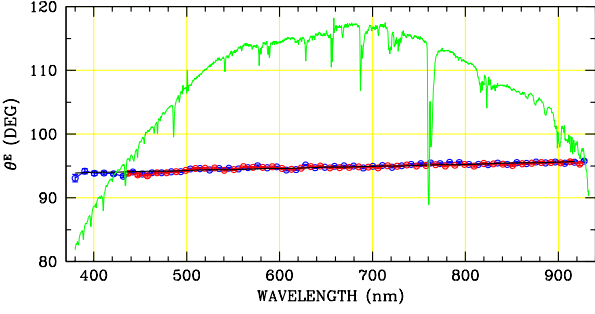


HD164073 2015-05-25

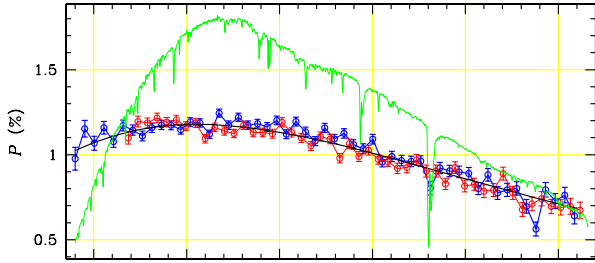
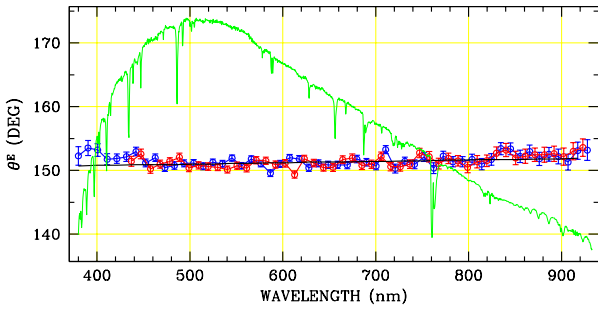




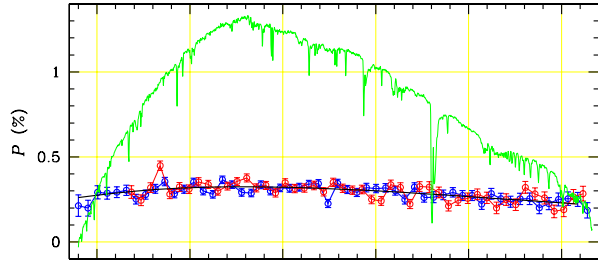
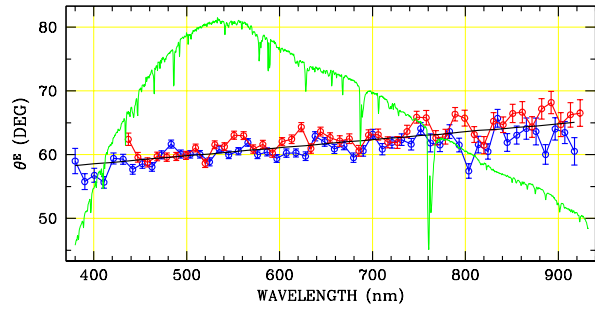
HD164740 2015-04-07



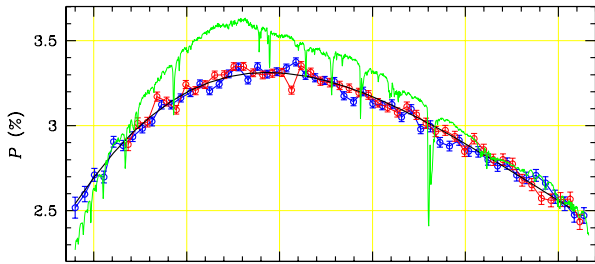
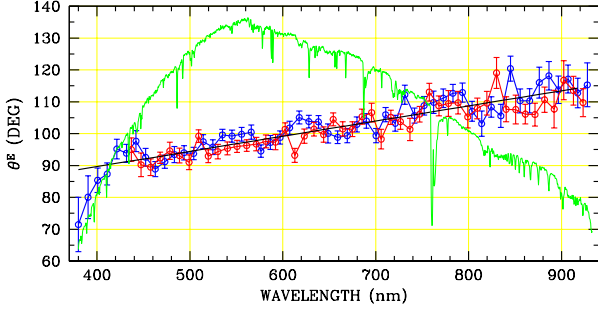
HD315023 2015-04-07



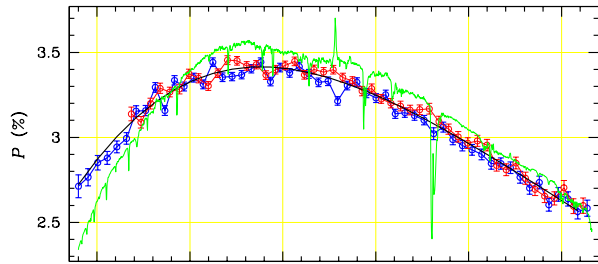
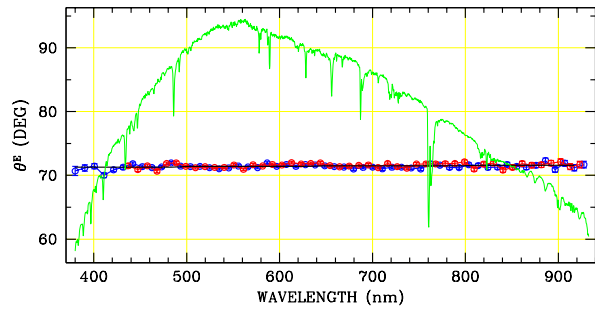
HD165319 2015-10-16



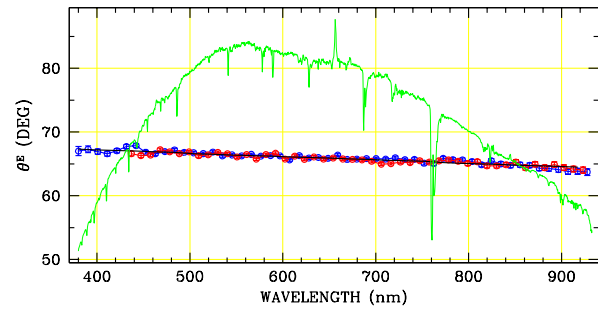
HD167838 2016-03-13



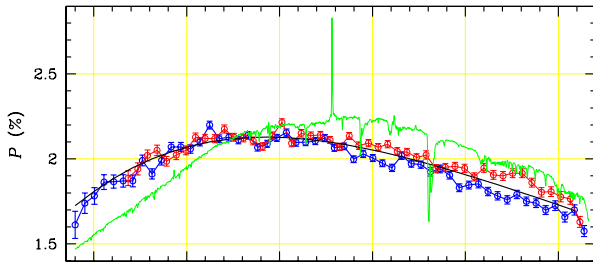
BD-13 4920 2015-04-07



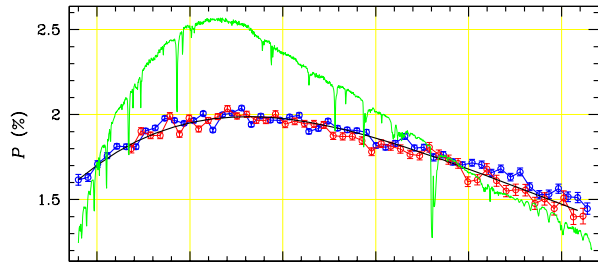
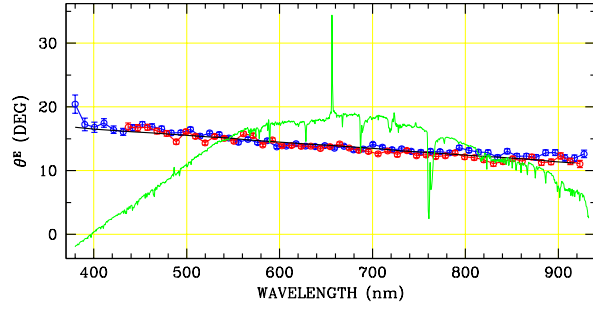
HD168076 2015-05-30



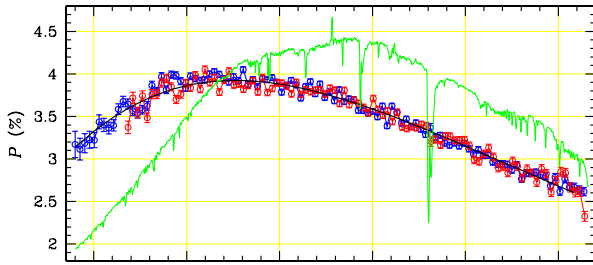
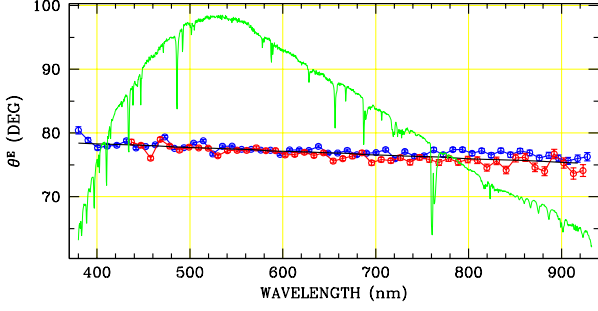




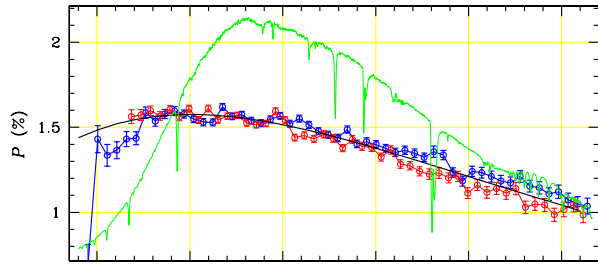
HD169454 2016-03-13



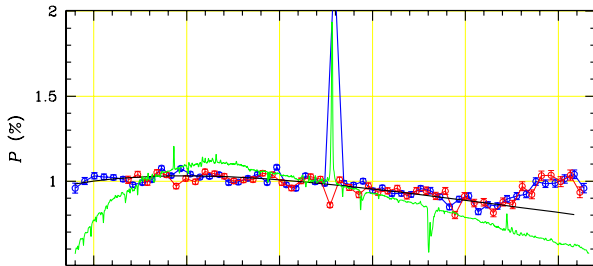
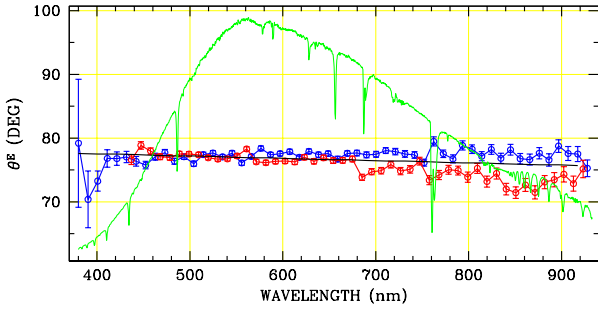
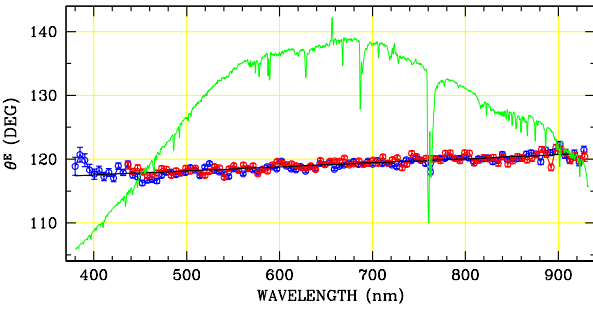
HD170740 2016-03-15



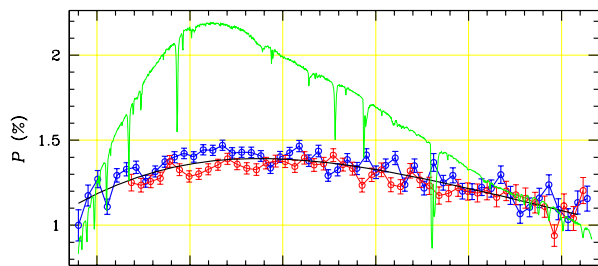
HD170938 2015-04-07



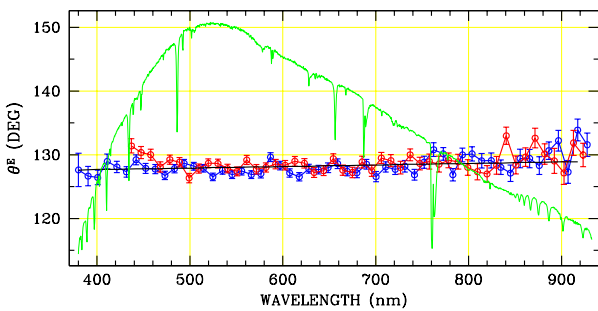
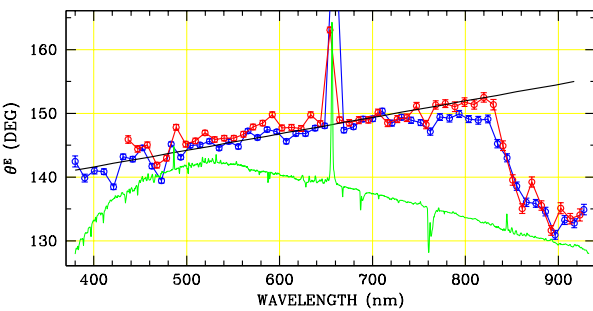
HD171957 2015-11-08

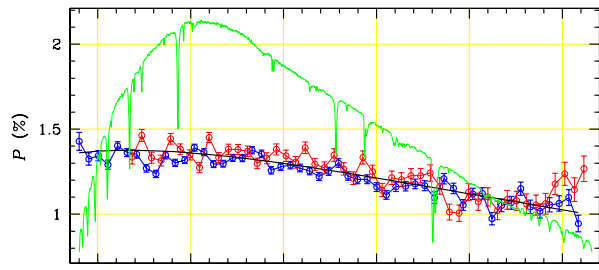


HD172694 2015-06-02



HD203532 2015-06-02





HD210121 2015-10-02

